Individual addressing for Ca^+ ions using a crossed acousto optic deflector

Master's Thesis

Dominique Cyrill Zehnder

Supervision
Philip Leindecker
Edgar Brucke

Dr. Cornelius Hempel
Prof. Dr. Jonathan Home

Ion Trap Quantum Computing group, ETH Zürich - PSI Quantum Computing Hub
Trapped Ion Quantum Information group, ETH Zürich

2. April 2024

Contents

Abstract

In this work a single ion addressing system for $^{40}Ca^+$ ions in a linear Paul trap is implemented using a crossed acousto optic deflector (cAOD). A new scheme for driving the cAOD is presented which facilitates addressing with standard devices optimized for the $+1$ $+1$ diffraction orders. The system is tested with a camera setup and a spot size of 2.24 µm, limited by the performance of the objective, is attained.

The crosstalk is measured to be on the order of 3×10^{-3} with a camera. The addressing system is integrated in the existing experiment. Preliminary tests with a single ion show that a spot diameter of 3.57 µm is achieved. This is small enough for individual ion addressing.

A fiber v-groove array (FVGA) is proposed as a mode filter for future addressing systems, an efficiency for arbitrary single channel couplings of $\geq 25\,\%$ is demonstrated.

Acknowledgements

I would like to thank Prof. Jonathan Home and Dr. Cornelius Hempel for giving me the opportunity to do my Master's thesis in their laboratories. I was openly welcomed into the group and the many group activities made the work really enjoyable.

I am grateful for the supervision through Philip Leindecker, Edgar Bruke and Cornelius Hempel. I enjoyed the many discussions and valuable inputs. Also the lab work was always fun and I was able to learn a lot.

Im thankful for the support of Flavia Timpu with implementing the fiber array setup and discussions about microscope objectives. I would like to thank Stephan Sigrist for his help with the many workshop parts and the feedback on my mechanical design. I also want to thank Julian Schmidt who always had an open ear and could always point me in the right direction.

Working in the lab was made more enjoyable with the company of all the other PSI ITQC members which were all super helpful and kind.

I would also like to thank all the members of TIQI who helped me during my work.

ETH

Eidgenössische Technische Hochschule Zürich
Swiss Federal Institute of Technology Zurich

Eigenständigkeitserklärung

Die unterzeichnete Eigenständigkeitserklärung ist Bestandteil jeder während des Studiums verfassten schriftlichen Arbeit. Eine der folgenden drei Optionen ist in Absprache mit der verantwortlichen Betreuungsperson verbindlich auszuwählen:

● Ich bestätige, die vorliegende Arbeit selbständig und in eigenen Worten verfasst zu haben, namentlich, dass mir niemand beim Verfassen der Arbeit geholfen hat. Davon ausgenommen sind sprachliche und inhaltliche Korrekturvorschläge durch die Betreuungsperson. Es wurden keine Technologien der generativen künstlichen Intelligenz[1] verwendet.

○ Ich bestätige, die vorliegende Arbeit selbständig und in eigenen Worten verfasst zu haben, namentlich, dass mir niemand beim Verfassen der Arbeit geholfen hat. Davon ausgenommen sind sprachliche und inhaltliche Korrekturvorschläge durch die Betreuungsperson. Als Hilfsmittel wurden Technologien der generativen künstlichen Intelligenz[2] verwendet und gekennzeichnet.

○ Ich bestätige, die vorliegende Arbeit selbständig und in eigenen Worten verfasst zu haben, namentlich, dass mir niemand beim Verfassen der Arbeit geholfen hat. Davon ausgenommen sind sprachliche und inhaltliche Korrekturvorschläge durch die Betreuungsperson. Als Hilfsmittel wurden Technologien der generativen künstlichen Intelligenz[3] verwendet. Der Einsatz wurde, in Absprache mit der Betreuungsperson, nicht gekennzeichnet.

Titel der Arbeit:

Individual addressing for Ca+ ions using a crossed acousto optic deflector

Verfasst von:
Bei Gruppenarbeiten sind die Namen aller Verfasserinnen und Verfasser erforderlich.

Name(n):	**Vorname(n):**
Zehnder	Dominique

Ich bestätige mit meiner Unterschrift:

- Ich habe mich an die Regeln des «Zitierleitfadens» gehalten.
- Ich habe alle Methoden, Daten und Arbeitsabläufe wahrheitsgetreu und vollständig dokumentiert.
- Ich habe alle Personen erwähnt, welche die Arbeit wesentlich unterstützt haben.

Ich nehme zur Kenntnis, dass die Arbeit mit elektronischen Hilfsmitteln auf Eigenständigkeit überprüft werden kann.

Ort, Datum	**Unterschrift(en)**
Zürich, 2.4.2024	D. Zehnder

Bei Gruppenarbeiten sind die Namen aller Verfasserinnen und Verfasser erforderlich. Durch die Unterschriften bürgen sie grundsätzlich gemeinsam für den gesamten Inhalt dieser schriftlichen Arbeit.

---

[1] z. B. ChatGPT, DALL E 2, Google Bard
[2] z. B. ChatGPT, DALL E 2, Google Bard
[3] z. B. ChatGPT, DALL E 2, Google Bard

1. Introduction

The field of quantum computing aims to harness quantum effects and leverage them to implement arbitrary computation. The quantum systems used for logic encoding are called qubits. Multiple different physical platforms demonstrated qubit manipulation and control. Platforms which look promising for scalable quantum computing are trapped ions [1, 2] and superconducting circuits [3, 4, 5]. There are many more quantum systems which enable logical or sensing application.

Single and multi qubit control is well established for medium sized systems up to 10's of qubits [4]. To enable the true potential of quantum computing the qubit operations need to be performed with high fidelity. An active front of research is to increase the reliability of quantum devices and to find logical encoding schemes which allow for errors to be corrected.

It can be estimated that a quantum computer needs at least several 100's of qubits [6] to achieve supremacy over classical computers. Therefore the scalability of the platform is another frontier which is important for the technological realization of quantum computation.

With a true fault tolerant quantum computer applications in many fields are predicted. One of the proven algorithm is the efficient factorization of prime numbers [7]. Also other computational fields such as machine learning [8] or finance [9] will profit from quantum computers.

Current quantum computing devices have yet to demonstrate applications beyond simple textbook examples. Promising use cases lie in simulating quantum chemistry or physical models. In this field for example many-body spin systems are simulated using the quantum nature of qubits. The systems can be simulated in a digital fashion [10] where the hamiltonian is approximated with gate operations.

1.1. Quantum computing with trapped Ions

Trapped ions are a good platform for quantum computations since the ions have a long decay time T_1 of $\sim 1\,\mathrm{s}$ for optical transitions. Qubits encoded in the hyper fine structure can have a T_1 of over several minutes. The qubit system is the valence electron of an alkali metal. These atomic systems are identical for all qubits unlike platforms where the qubits are fabricated. A drawback is the need for high precision and stable laser systems.

Quantum computing with trapped ions can use different species of ions. Typically, alkaline earth metals like Be, Mg, Ca or Sr are used, but also Yb is often used because of its good-performing hyperfine qubit. Depending on the chosen ion species the qubit is encoded in different schemes. The qubit can be encoded in optically accessible states, Zeeman states or hyperfine states can be used to encode the qubit [2]. In our lab we work with $^{40}\mathrm{Ca}^+$ and the qubit is encoded using optic transitions.

The qubit is encoded using electron shelving in the $\mathrm{D}_{5/2}$ states (figure 1.1). The state is long lived with a lifetime of $1.2\,\mathrm{s}$ [11]. The qubit transition is accessible with a laser

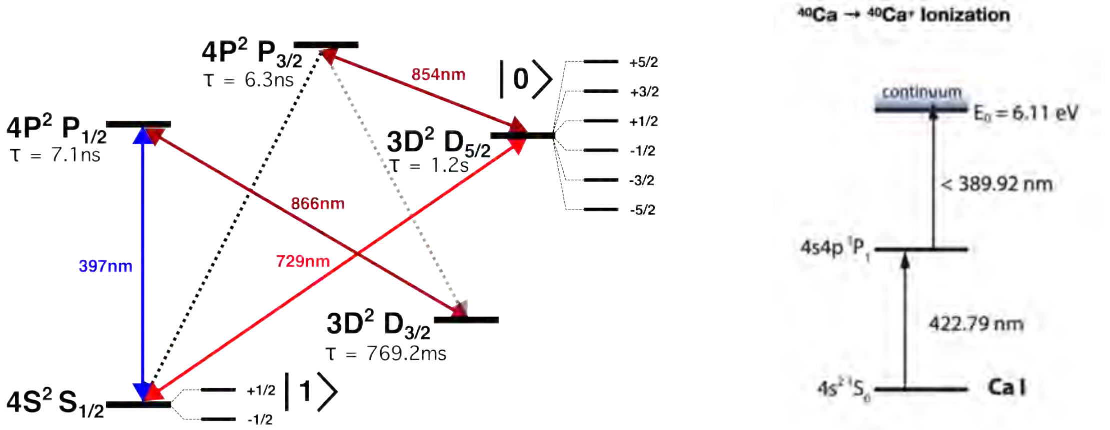

(a) ^{40}Ca$^+$ level scheme (b) Ionization of ^{40}Ca

Figure 1.1.: (a) Simplified energy level scheme of ^{40}Ca$^+$ [1]. The short lived state $P_{1/2}$ is used for readout $\tau = 7.1$ ns [12]. The metastable states in $D_{5/2}$ with a lifetime of 1.2 s [11] are used to encode the $|0\rangle$ state. The ground state encodes the $|1\rangle$ state. (b) the ionization scheme to go from atomic to ionic calcium [13].

at 729 nm. The readout of the system is implemented with 397 nm light. If light is scattered during the detection pulse the ion was in the $S_{1/2} \cong |1\rangle$ state. This readout is possible due to the short lifetime of 7.1 ns of the $P_{1/2}$ state compared to the meta-stable lifetime of the $D_{5/2}$ state where the light cannot couple to the ion.

The ions are generated by photo ionization with two near ultra violet (UV) lasers. The atoms are produced in an oven placed next to the trap. The ionization uses a two stage process. A frequency tunable 423 nm laser selects the correct calcium isotope which is then ionized using a 375 nm laser. There is a weak decay path from $P_{1/2}$ to $D_{3/2}$ states, to repump these states a 866 nm laser is used. To reset the qubit 854 nm light is used to pump the excitation to the short lived $P_{3/2}$ state. For state preparation in addition to the reset and repumping beam a σ^+ polarized laser at 397 nm is used to couple the states $|S_{1/2}, m_j = -1/2\rangle \leftrightarrow |P_{1/2}, m_j = +1/2\rangle$. This will optically pump the excitation to the state $|1\rangle \cong |S_{1/2}, m_j = 1/2\rangle$.

Two types of radio frequency (RF) traps are used to trap ions. One option is the linear three dimensional Paul trap which uses two RF electrodes and several DC electrodes to generate a trapping potential. The potential with strong radial confinement and the coulomb repulsion of the ions results in a ion chain along the trap axis. A novel kind of RF traps are surface traps where the trapping potential is generated from an 2D micro fabricated chip with all electrodes in a single plane. This type of trap has a shallower potential but is more promising towards scalability. The laser beams for controlling the ions are either free space beams or from integrated photonics wave guides in the case of surface traps.

---

[1] Solid transitions are available lasers in the lab, dotted transitions cannot be driven and are only decay channels. The decay from $D_{3/2}$ and some Zeeman states are omitted for readability.

1.2. Individual addressing

In order to implement quantum circuits addressing of single ions is needed. This individual addressing of ions in the ion crystal can be implemented using different methods. Most techniques are based on tightly focussed laser beams which only interact with one ion in the string.

Several different implementations for optical addressing were previously demonstrated. One type of addressing system utilized an optical modulator to deflect the laser beam. An optical system with an objective focuses the modulated beam onto the ions. The deflection can be implemented with an electro optic modulator (EOM) [14], single acousto optic modulator (AOM) [15, 16] or with cAOD [17, 18]. Other addressing systems use spatial light modulators like digital micro-mirror devices (DMDs) to shape and steer the addressing beam [19].

A different type of systems uses micro-fabricated waveguides with a fixed pitch [20, 21]. These devices are engineered for low crosstalk at the output side, despite of the small distance of 15 - 20 µm between the waveguides. The light is delivered with fibers to the wave guide array (WGA) and focussed onto the ion crystal with a lens and an imaging objective. The light is split into fibers using fiber splitters[2] and switched with a separate fiber AOM in each channel.

In the current setup a 12 channel WGA is used to address ions. Currently only two channels are configured. The goal is to test different addressing systems for their fidelity and scalability. Therefore in this thesis I implemented an individual addressing system based on a cAOD and work towards a combination of cAOD with a FVGA. We use a cAOD since this will enable us to have individual addressing with a constant frequency shift introduced by the modulator.

One major advantage of a cAOD setup over a WGA chip is the higher power which can be delivered to the ions in single addressing applications. In the WGA the input power is first split into N channels and has additional losses from the fiber AOM. The cAOD on the other hand experiences only the loss from the two acousto optic deflectors (AODs). For multi tone addressing the power in each cAOD diffraction spot scales with $1/N^2$ so up to three ion addressing this system will deliver higher power in our case.

A further advantage of the cAOD device is the phase stability between different channels since all ions are addressed from only one device. In the case of the WGA every channel uses its own fiber AOM. These devices have strong dependences on temperature and humidity and a stable operation of multiple such devices is difficult.

The cAOD device has no fixed spacing between the addressing beams. Additionally this enables also correction in the vertical direction to account for small errors in the addressing position.

From a scalability point of view the cAOD has advantages. Generally this one device will be cheaper compared to one AOM per ion. Also the attainable addressing range from an cAOD is by a factor 4 - 6 bigger. This comparison holds for the current available chip with 12 channels. But the wave guide chips can be scaled up to include more channels.

One drawback of cAOD type systems is the beam quality. Due to the diffraction in the acousto optic crystals the beam will be deformed. Here the WGA will deliver a gaussian beam with less abberations. Also for multi ion addressing the cAOD device will generate unwanted diffraction orders which introduce a lot of scattering on the trap and in the chamber.

---

[2] Fiber optics device which splits light from 1 fiber to N (usually 2 - 16) fibers according to a fixed ratio.

	WGA	cAOD	combined
Optical power	-	+	0
Phase stability	-	+	+
Addressing flexibility	-	+	-
Spot shape	+	-	+
Scatter	+	-	+
Cost	-	+	+

Table 1.1.: Comparison of three possible addressing systems. The signs indicate if the system performs well (+), bad (-) or neutral (0) regarding the criteria. The optical power is the peak power that can be delivered relative to the power before the addressing system. The addressing flexibility compares if the beam has fixed spacing on the addressing axis or arbitrary positions are possible. The spot shape considers primarily the achievable size but also aberrations. Scatter occurs if stray light illuminates the chamber or is reflected from the trap.

A new idea is to use an cAOD in combination with a WGA. The WGA would act as a mode cleaner to reduce crosstalk and scattering. The cAOD has a better phase stability compared with individual fiber AOMs for each cannel. For this the light of the cAOD is coupled int a FVGA which is connected directly to the WGA (without the need for fiber AOMs). The addressing spacing will be fixed and additional losses from the coupling are introduced, but the fidelity of the overall system can gain from the reduced crosstalk and the single device as the source for the addressing (table 1.1).

2. Theoretical background

For a general quantum computer to be useful it needs to fulfill some requirements. One generally accepted list of criteria was introduced by DiVincenzo [22]:

1. A scalable and well defined qubit system.
2. State initialization.
3. Coherent time much longer than gate time.
4. A universal set of gates[1].
5. Qubit readout.

In the previous chapter it was briefly discusses that a trapped ion platform fulfills this criteria. In this chapter I want to discuss in more detail what a universal set of gates is and how it is realized on the given qubit system. This chapter focuses on the theoretical aspect. The experimental realization in the setup is presented in the chapter 5.1.

2.1. Qubit control

Unlike a classical bit which can only take either 0 or 1 as an value the state of a qubit is generally a superposition of two states:

$$|\psi\rangle = \alpha|0\rangle + \beta|1\rangle. \tag{2.1}$$

For the state to be physical the complex coefficients α and β need to be normalized: $|\alpha|^2 + |\beta|^2 = 1$. The computational states $|0\rangle$ and $|1\rangle$ are elements of the Hilbert space $\mathcal{H}_{qubit} \cong \mathbb{C}^2$ and we identify them with the following vector representation:

$$|0\rangle = \begin{pmatrix} 1 \\ 0 \end{pmatrix}, \qquad |1\rangle = \begin{pmatrix} 0 \\ 1 \end{pmatrix}. \tag{2.2}$$

A complete basis of this Hilbert space can be formed with the so called Pauli operators and the identity:

$$X = \begin{pmatrix} 0 & 1 \\ 1 & 0 \end{pmatrix}, \qquad Y = \begin{pmatrix} 0 & -i \\ i & 0 \end{pmatrix}, \qquad Z = \begin{pmatrix} 1 & 0 \\ 0 & -1 \end{pmatrix}, \qquad \mathbb{1} = \begin{pmatrix} 1 & 0 \\ 0 & 1 \end{pmatrix} \tag{2.3}$$

We immediately see that our computational states are eigenvectors of the Pauli-Z gate. In quantum circuits we often use the eigenvalues of the X operator as bases:

$$|+\rangle = \frac{1}{\sqrt{2}}(|0\rangle + |1\rangle), \qquad |-\rangle = \frac{1}{\sqrt{2}}(|0\rangle - |1\rangle). \tag{2.4}$$

---

[1] A set of gates which allows to express all possible operations as a combination.

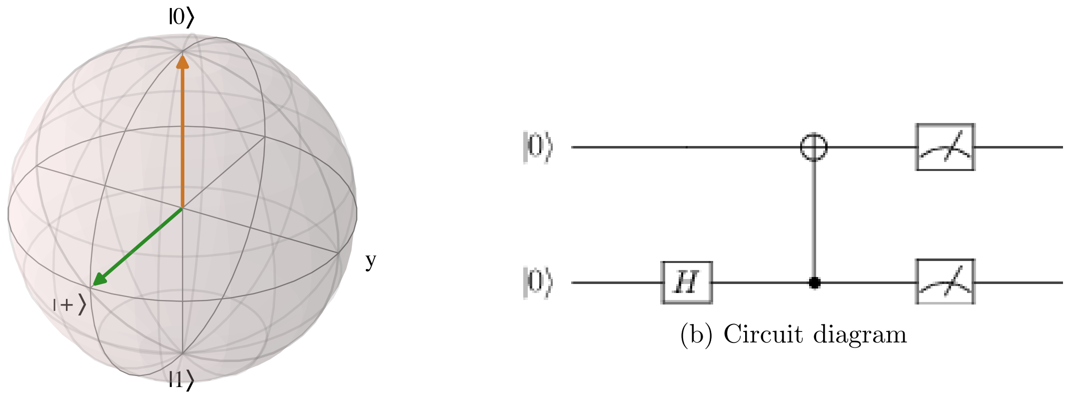

(a) Bloch sphere

(b) Circuit diagram

Figure 2.1.: (a) Visualization of states in the Bloch sphere. Orthogonal states are at the opposite side of the sphere. (b) Example of a minimalistic quantum circuit. Two qubits are prepared in the $|0\rangle$ state and a successive application of a Hadermard and a CNOT gate is used to create a Bell state. The last step indicates a measurement on each qubit.

To perform a quantum operation on a qubit means to apply a unitary transformation (a gate). For example the application of an X-gate on a qubit will act like a NOT operation. Another gate is the so called Hadamard gate which we can interpret as a change of basis between X and Z basis. The gate will transform $|0\rangle \rightarrow |+\rangle$ and $|1\rangle \rightarrow |-\rangle$ and vice versa.

$$H = \frac{1}{\sqrt{2}} \begin{pmatrix} 1 & 1 \\ 1 & -1 \end{pmatrix} \tag{2.5}$$

In the case of one qubit we can use the Bloch sphere to visualize the state and the effects of gates on a qubit. For this we write the coefficients in equation 2.1 as: $\alpha = cos(\theta/2)$ and $\beta = sin(\theta/2)e^{i\phi}$. This is possible since global phase factors do not change a state. We see that this is essentially a parametrization of a sphere. The poles of the Bloch sphere are the orthogonal eigenstates of the Pauli operators (figure 2.1a). In this picture we can interpret the application of a gate to an qubit as a rotation around the given axis.

In addition to the single qubit rotations also a phase shift gate is needed it will introduce a constant phase shift of $e^{i\phi}$ to one of the qubit states.

$$P_\phi = \begin{pmatrix} 1 & 0 \\ 0 & e^{i\phi} \end{pmatrix} \tag{2.6}$$

To have a universal set of gates according to the DiVicenzo criteria we are missing multi qubit gates. The single qubit description is extended to the multi qubit case with the tensor product. A pure two qubit state (or product state) can be written as:

$$|\Psi\rangle = |\psi_A\rangle_A \ \otimes \ |\psi_B\rangle_B. \tag{2.7}$$

This extension also applies for multi qubit gates. One of the most used two qubit gate is the CNOT gate or controlled NOT. This gate conditions the application of a X gate to the target qubit on the control qubit. Only when the first one is in $|1\rangle$ the NOT gate will be applied otherwise the identity operation is used. With the tensor formalism this is written as:

$$CNOT = |0\rangle_A\langle 0|_A \otimes \mathbb{1}_B + |1\rangle_A\langle 1|_A \otimes X_B. \tag{2.8}$$

There exist states which cannot be written as the tensor product of the individual system states. We call such states entangled. They can be written as a linear combination of product states. An example of an entangle state is:

$$|\Psi\rangle = \frac{1}{\sqrt{2}}(|00\rangle + |11\rangle) = \frac{1}{\sqrt{2}}(|0\rangle_A \otimes |0\rangle_B + |1\rangle_A \otimes |1\rangle_B) \tag{2.9}$$

In trapped ion computing two qubit gates are usually implemented with the Mølmer-Sørensen(MS) gate [23] which does not implement a CNOT gate. With additional single qubit gates the MS gate becomes equivalent to a CNOT gate.

A general quantum algorithm will consist of three parts. First a qubit register will be initialized to a defined state. Then a series of single and multi qubit gates will be applied. Finally the qubits in the register are measured to extract the results. This can by visualized with the circuit diagrams shown in figure 2.1b.

2.2. Rabi oscillation

The implementation of gates with trapped ions is realized with the light matter interaction between the trapped ion and applied light fields. Following the derivation in [13, 24] we first look at the semiclassical interaction of light field with a two level system.

The atomic system has the ground state $|g\rangle$ and the excited state $|e\rangle$ which are separated by $\Delta E = \hbar\omega_0$. If we set the zero point energy in the middle of the levels, then the atomic Hamiltonian is:

$$H_a = \frac{\hbar\omega_0}{2}\hat{\sigma}_z \tag{2.10}$$

The classical light field with a frequency ω_l and a phase ϕ_l can be written as: $\vec{E}(t,\vec{r_0}) = \vec{E}_0(\vec{r_0})\cos(\omega_l t + \phi_l)$. The interaction between the radiation an the atom is given as:

$$H_l = -\hat{D} \cdot \vec{E}(t,\vec{r_0}) \tag{2.11}$$

The operator $\hat{D}$ is the dipole operator. According to the definition of the Rabi frequency as: $\Omega_0 = |-\frac{1}{\hbar}\langle e|\hat{D} \cdot \vec{E}(\vec{r_0})|g\rangle|$, we can rewrite the Hamiltonian for the laser interaction to:

$$H_l = \hbar\Omega_0\hat{\sigma}_x\cos(\omega_l t + \phi_l). \tag{2.12}$$

The total Hamiltonian can be expressed as the sum of the atomic systems plus the interaction term: $H = H_a + H_l$. A change to the interaction picture with respect to the atomic Hamiltonian makes the further discussion of the time evolution more clear. For this we transform the interaction Hamiltonian as follows: $H_{int} = e^{-iH_at/\hbar}\, H_l\, e^{iH_at/\hbar}$.

$$H_{int} = \hbar\Omega_0\big(\cos(\omega_l t - \phi_l)\cos(\omega_0 t)\hat{\sigma}_x + \cos(\omega_l t - \phi_l)\sin(\omega_0 t)\hat{\sigma}_y\big) \tag{2.13}$$

We recognize that there will be cross terms which oscillate at $\omega_l + \omega_0$ and $\omega_l - \omega_0$. We apply the rotating wave approximation and drop the terms with the higher oscillation frequency. The laser detuning $\Delta = \omega_l - \omega_0$ is introduced and the expression is rewritten using trigonometric identities:

$$H_{int} = \hbar\frac{\Omega}{2}\big(e^{-i(\Delta t+\phi_l)}\hat{\sigma}_+ + e^{i(\Delta t+\phi_l)}\hat{\sigma}_-\big) \tag{2.14}$$

The unitary transformation implemented by this Hamiltonian for a resonant drive ($\Delta = 0$) is:

$$U(\Theta, \phi_l) = exp\big(-i\frac{H_{int}t}{\hbar}\big) = \begin{pmatrix} \cos(\frac{\theta}{2}) & -ie^{-i\phi_l}\sin(\frac{\theta}{2}) \\ -ie^{i\phi_l}\sin(\frac{\theta}{2}) & \cos(\frac{\theta}{2}) \end{pmatrix} \tag{2.15}$$

In this operation we can recognize a combination of the Pauli X and Y gate. The pulse area $\theta = \Omega t$ defines the rotation angle and the phase ϕ_L will select the rotation axis in the x-y plane of the Bloch sphere.

Following the discussion in [25] the coupling strength Ω can be computed as the matrix element between the states of interest. In the case of the chosen qubit transitions $|S_{1/2}, m_j = 1/2\rangle \leftrightarrow |D_{5/2}, m_j = m'\rangle$ it is a quadruple transition. This can be written in terms of the Clebsch-Gordan coefficients as:

$$\Omega = \frac{eE_0}{2\hbar}\sqrt{\frac{15A}{c\alpha k^3}}\Lambda(m, m')g^{(\Delta m)}(\phi, \gamma) \tag{2.16}$$

The constants c and α are the speed of light and the fine structure constant. The total decay rate is $A = \Gamma(D_{5/2})$. The last factor $g^{(\Delta m)}(\phi, \gamma)$ accounts for the geometric relation between the magnetic quantization axis, the wave vector and the polarization angle.

In an ion trap the ions are trapped in an harmonic potential along the z axis and therefore we have to consider the motional degrees of freedom while addressing the ion. Following [13] we add the contribution of the harmonic motion to the atomic hamiltonian:

$$H_a = \frac{\hbar\omega_0}{2}\hat{\sigma}_z + \hbar\omega_t\big(\hat{a}_z^\dagger\hat{a}_z + \frac{1}{2}\big). \tag{2.17}$$

The frequency ω_t is the ion oscillation frequency of the trap. This introduces the motional sidebands $\omega_0 \pm \omega_t$ du to the Doppler shifted interaction. This couples the internal electronic state of the ion to its motional degrees of freedom. The interaction part of the Hamiltonian becomes:

$$H_l = \hbar\frac{\Omega}{2}(\hat{\sigma}_+ + \hat{\sigma}_-)\big(e^{i\eta(\hat{a}_z+\hat{a}_z^\dagger)}e^{-i(\omega_l t-\phi_l)} + e^{-i\eta(\hat{a}_z+\hat{a}_z^\dagger)}e^{i(\omega_l t-\phi_l)}\big). \tag{2.18}$$

Here the Lamb-Dick factor is introduced:

$$\eta = kx_0\cos\theta = k\sqrt{\frac{\hbar}{2m\omega_r}}\cos\theta. \tag{2.19}$$

This factor accounts for the extent of the wave function, the wavelength of the light and the relative angle between the motion and the wave vector. Again the rotating wave approximation can be applied. Additionally we assume the extent of the wave packet x_0 is much smaller than the light wavelength. This so called Lamb-Dicke regime with $\eta^2(2\bar{n}+1) \ll 1$ is usually attained after Doppler cooling. The Lamb-Dicke regime allows to Taylor expand the terms depending on η. With this the final interaction hamiltonian is:

$$H_{int} = \hbar\frac{\Omega}{2}\big(e^{-i(\Delta t-\phi_l}\hat{\sigma}_+\big[\mathbb{1} + i\eta(\hat{a}_z e^{-i\omega_t t} + \hat{a}_z^\dagger e^{i\omega_t t})\big] + h.c.\big) \tag{2.20}$$

This results in an Rabi frequency which is depending on the motional state of the ion: $\Omega_n = (1-\eta^2 n)\Omega_0$. For the case $\Omega \ll \omega_t$ the rotating wave approximation might be applied for the trap frequency ω_t as well. Then the two sideband and carrier transition are:

- Resonant drive $\Delta = 0$ this couples $|g,n\rangle \leftrightarrow |e,n\rangle$. This is called the carrier transition.

$$H_{car} = \hbar\frac{\Omega_n}{2}\big(e^{i\phi_l}\hat{\sigma}_+ + e^{-i\phi_l}\hat{\sigma}_-\big) \tag{2.21}$$

- Detuned on the red motional side band ($\Delta = -\omega_t$) this couples $|g,n\rangle \leftrightarrow |e,n-1\rangle$. The transition rate is $\Omega_{n,n-1} = \eta\sqrt{n}\Omega_0$.

$$H_{rsb} = i\hbar\eta\frac{\Omega_{n,n-1}}{2}\big(e^{i\phi_l}\hat{a}_z\hat{\sigma}_+ + e^{-i\phi_l}\hat{a}_z^\dagger\hat{\sigma}_-\big) \tag{2.22}$$

- Detuned on the blue motional side band ($\Delta = +\omega_t$) this couples $|g,n\rangle \leftrightarrow |e,n+1\rangle$. The transition rate is $\Omega_{n,n+1} = \eta\sqrt{n+1}\Omega_0$.

$$H_{rsb} = i\hbar\eta\frac{\Omega_{n,n+1}}{2}\big(e^{i\phi_l}\hat{a}_z^\dagger\hat{\sigma}_+ + e^{-i\phi_l}\hat{a}_z\hat{\sigma}_-\big) \tag{2.23}$$

2.3. Gate Implementation

Generally the experimental parameters which can be adjusted are the pulse length, the power, the phase and the frequency detuning of the laser beam. By adjusting this parameters we can engineer the interaction of the applied laser field onto to the qubit to implement gats described in section 2.1.

2.3.1. Single qubit gates

NOT gate The most straight forward implementation of a X-gate ist to drive the optical qubit transition resonantly (detuning $\delta = 0$). The interaction Hamiltonian describing this interaction is given in equation 2.15. We see that the X-gate is implemented if the pulse area is $\Omega t = \pi$. The phase does not matter in the case of a π-pulse since any rotation axis has the same effect.

Phase gate The Pauli Z gate is often referred to as Phase gate. It can be implemented using a decomposition into multiple rotations R_x and R_y using the interaction described in equation 2.15.

Another possibility is to use far detuned laser beam to induce an AC Stark shift [26]. The energy shift for a largely detuned beam is:

$$\Delta_{AC} = -\frac{\Omega^2}{2\Delta}. \tag{2.24}$$

Here Ω is the Rabifrequency and Δ is the detuning. The phase shift is $\Delta\phi = \Delta_{AC}t/\hbar$. For a Z gate we want a phase shift of π. By solving for the pulse length $t(\Delta)$ we can apply the desired pulse.

Single addressing Depending on the used addressing system it is not possible to resonantly address single ions. An alternative method is to use an AC Stark shift with additional global $\pi/2$-pulses [13]. In that case one uses first a global $\pi/2$-pulse to bring a state vector onto the equatorial plane of the Bloch sphere. An (single ion) addressing beam can introduce an AC Stark shift to the desired ions. The pulse length is chosen such that a rotation by π around the z-axis is implemented (compare to Phase gate). A second $\pi/2$-pulse with the opposite sign is applied. This effectively switches the states for the addressed ions and leaves the other ions in the initial state.

2.3.2. Multi qubit gates

Multi qubit gates for trapped ions are based around the common motion of the ion crystal. This allows to transmit information between ions over the shared motion.

Two common entangling gates for trapped ion platforms are the CZ and MS gate. The first implementation was proposed by Cirac and Zoller [1]. It relies on ground state cooling and is thus often replaced by the Mølmer-Sørensen gate [23] that only requires the ions to be in the Lamb-Dicke regime.

The Cirac-Zoller gate uses the common motion by a direct mapping of the internal states to the ground and first excited motional states. For this the first ion is addressed with an π-pulse to drive the first red sideband. This couples the motional states $|0, e\rangle \leftrightarrow |1, g\rangle$. Now the second ion is addressed with a 2π pulse coupling only the $|1, g\rangle$ with an ancilla state $|0, a\rangle$. The second ion will get a phase of 180° if the first ion was in the exited sate. Then the first π pulse is reversed.

The Mølmer-Sørensen gate also implements a phase gate up to single qubit gates. The gate is implemented by means of a bichromatic light field where both sidebands are driven off resonantly in a way that the sum of both frequencies add up to double of the qubit separation. Thus the gate couples the states $|gg\rangle \leftrightarrow |ee\rangle$ over four possible paths.

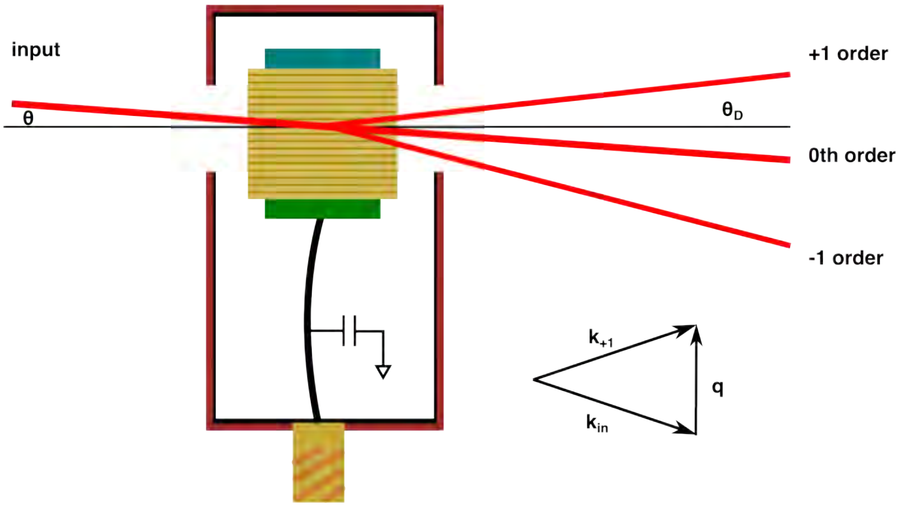

Figure 2.2.: Workin principle of an acousto optic modulator. Acoustic waves are generated in the crystal by a transducer (green). The absorber (blue) will reflect or absorb the acoustic wave depending on the specific device. Usually some passive electronic components are included for impedance matching. The crystal cut is simplified and is chamfered according to the particular optimizations.

2.4. Acousto optic devices

For the pulse shaping and the frequency control fast modulators are necessary. One type of devices which enables both amplitude modulation and shifting of the optical frequency are based on the acousto-optic effect. These devices are called either AOM or AOD. The terminology is not strictly defined and usually indicates the targeted application. AOMs are preferred over other types of optical modulators due to their ability to shift the optical frequency, the good extinction ratio and fast modulation speed.

The principle underlying the devices is the interaction between light and the acoustic wave propagating in the crystals. The acoustic wave modulates the index of refraction in the crystal according to the RF frequency. This modulation results in a transmission grating which will diffract the light. This static or adiabatic approximation of a grating is valid due to the vastly different timescales of the acoustic wave and the optical frequency [27].

Using the Bragg condition we can compute the input angle where a portion of the power is refracted.

$$\sin(\theta) = \frac{M\lambda}{2\Lambda} = \frac{M\lambda\Omega}{2v} \tag{2.25}$$

In this equation λ is the laser wavelength and Λ is the acoustic wavelength. The input angle is θ and M denotes the diffraction order. We can substitute the acoustic wavelength Λ with the acoustic velocity v and acoustic frequency Ω. The acoustic frequency is identical to the RF drive. In the case of an isotropic crystal the input angle is equivalent to the diffracted angle.

The power which will be deflected to a given order is dependent on the acoustic power. If the input angle is kept constant but the RF drive frequency is changed the Bragg condition will be slightly off and the diffraction efficiency is reduced. This effect in combination with the RF absorption bandwidth will define the usable bandwidth of the device [28].

We can write the wavevectors for the optical beams as the $k = n\omega/c$ and the wavevector for the soundwave as $q = \frac{2\pi\Omega}{v}$. Where Ω ist the acoustic frequency, v is the velocity in the crystal and n is the index of refraction. We can think of the Bragg condition also in therms of momentum conservation of the wavevectors. This translates to the vector relation $\vec{k_o} = \vec{k_i} \pm \vec{q}$.

In the previous discussion the modulation in the index of refraction was treated statically. But the modulation is changing with the RF frequency Ω. This can be interpreted as a doppler shift to the refracted wave [27]. Therefore the output frequency $\omega_o = \omega_i + \Omega$.

We can view this effect also in terms of momentum and energy conservation between the phonon and photon. The momentum transfer will change the output angle of the optical beam. The energy conservation will introduce a slight shift in frequency to the deflected beams.

Construction acousto optic modulators are constructed very simple (figure 2.2). In the enclosure there is the optical crystal where the beam is actually modulated. The crystal is connected to an RF transducer which generates the acoustic waves in the crystal and some kind of damper which absorbs the wave in a well-defined way. The RF signal drives the transducer directly. Passive electronic components are used for impedance matching.

Parameter selection The AOM devices are tuned by selecting the crystal material, the mode of the acoustic wave and the crystal cut itself. Most available devices use TeO_2 crystals because it has a very high $\mathcal{M}$ value. This value is a measure for how much an acoustic wave can alter the refractive index of the material. As we can see from equation 2.25 devices meant for deflection and steering (AODs) usually uses transverse modes with an lower acoustic velocity typically around 650 m/s. This results in bigger deflection angles for lower frequencies. Devices meant for frequency shifting and switching take advantage of the higher longitudinal velocities in the order of 4000 m/s. The optimization of the crystal depends on the desired application parameters such as: wave length, diffraction order, input- and output angles RF frequency etc. In addition many crystals come with an anti reflection coating to minimize losses for the designed wavelength.

2.5. Individual addressing with an AOD

Due to the characteristics described in the previous chapter, AODs are well suited for addressing trapped ions. They can switch laser beams fast and precise, but most importantly AODs enables fast deflection of the beams. A first approach is to take an AOD to deflect the beam and use an optical system to focus the laser on a string of ions. The deflection angle can be changed by adjusting the RF drive. This simple implementation with one AOD device has the drawback, that the introduced frequency shift δ_f onto the laser beam will depend on the addressed position. One can implement only phase shift single qubit gates using the AC stark shift (see chapter 2.3.1).

In order to resonantly address the ion string one needs to have a constant frequency shift over the total addressing range. A possible method to implement this is to use

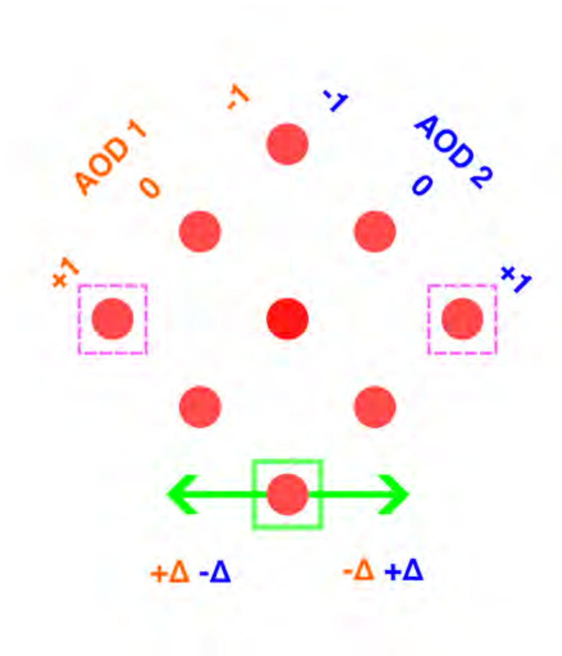

Figure 2.3.: Diffraction pattern of a cAOD. The devices are rotated by 45° such that the addressing axis is horizontal. The deflection axis of the two devices are orthogonal to each other. The pink square indicate the operation points from previous work. The green making shows the operation point chosen for this work.

two AODs which have orthogonal addressing axis. This crossed configuration will be referred to as crossed acousto optic deflector (cAOD). This placement of the devices will generate a grid like diffraction pattern (figure 2.3). Each generated dot will accumulate two frequency shifts corresponding to the RF drive frequency Ω multiplied with the diffraction order. We can immediately see diffraction orders with a total shifts of $+2\Omega, +\Omega, 0, -\Omega, -2\Omega$ (considering only the first orders).

In previous works the +1 -1 diffraction order was chosen to implement an addressing system with zero frequency shift [29, 18] . By using the same RF frequency for both AODs the frequency shift is constant($\delta_f = 0$). The deflection angle of the diffracted order is proportional to the drive frequency $\Omega = \Omega_1 = \Omega_2$. Changing the frequency shifts the order along the horizontal line with zero frequency shift. This implements an addressing system capable of addressing all ions resonantly. The addressing frequency for the AODs can then be expressed as:

$$\Omega_{1,2} = \Omega_0 + \Delta_A \tag{2.26}$$

where Ω_0 is the AOD center frequency and Δ_A is the addressing frequency offset which has to be in the bandwidth of the device.

The mode described needs an cAOD which is capable of operating at ether $+-$ or $-+$ diffraction orders. This is usually a non standard configuration of the devices. One can get essentially the same performance with a standard device which is optimized for $++$ operation. In this case one has to drop the constraint of a zero frequency shift and work with a constant frequency shift to the addressing beam. This shift can be pre-compensated. For this addressing scheme we do not drive both AODs at the same frequency but add and subtract the addressing frequency Δ_A to the two devices:

$$\begin{aligned} \Omega_1 &= \Omega_0 + \Delta_A \\ \Omega_2 &= \Omega_0 - \Delta_A \end{aligned} \tag{2.27}$$

The addressing beam experiences a constant frequency shift $\delta_f = 2\Omega_0$. One drawback is the need for an individual RF generator for each AOD.

The constant frequency shift is of essence since only this allows for resonant addressing of multiple ions at the same time (figure 2.4c). For this multiple frequencies are sent to each AOD simultaniously.

Another option with a cAOD is to use both degrees of freedom to steer the beam to an arbitrary point in the span of the two AOD ranges. For this it is useful to define the two frequencies $\Delta f_{x,y}$ which are 45° tilted with respect to the AOD axes (figure 2.4b). We define them relative to the center position. These frequencies can then be decomposed to the relevant AOD drive frequencies as follows:

$$\begin{aligned} \Omega_1 &= \Omega_0 + (\Delta f_x + \Delta f_y)/\sqrt{2} \\ \Omega_2 &= \Omega_0 - (\Delta f_x - \Delta f_y)/\sqrt{2} \end{aligned} \tag{2.28}$$

This driving scheme will introduce an frequency shift $\delta_f = \sqrt{2}\Delta f_y$ in addition to the shift of the center frequencies.

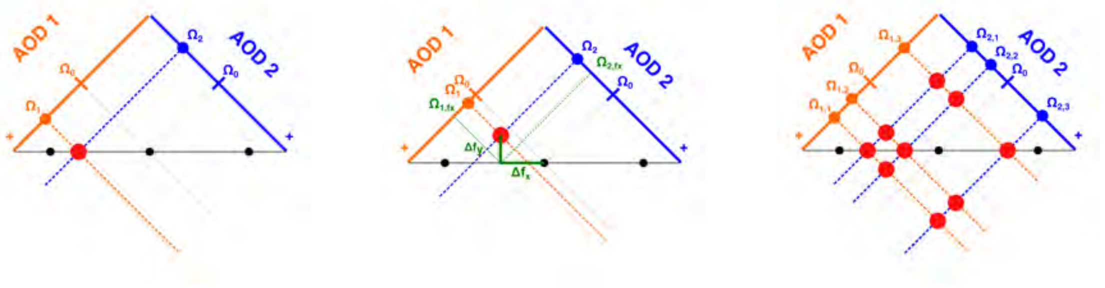

(a) single addressing

(b) xy position

(c) multi tone

Figure 2.4.: Illustration of how the addressing beam is deflected by changing the RF frequency within the bandwidth. We always look at the +1 +1 diffraction order which will be deflected to the center when the cAOD is driven at its center frequency Ω_0. The ion axis is horizontal, each AOD is angled by 45° with respect to the ion string. The image is not to scale. (a) In this mode the addressing is along the ion string. Only a constant frequency shift is introduced. (b) The beam is positioned on an arbitrary position within the span of the two AODs. The drive frequencies for the individual AODs are found by projecting the horizontal frequency Δf_x on the AOD axis. The projection of the vertical deflection Δf_y will introduce a correction. We choose the sign such that positive $\Delta f_{x,y}$ are to the left and bottom. (c) If multiple frequencies are sent to the cAOD not only the desired spots on the ion axis are generated but also unwanted combinations of all drive frequencies.

3. Design of an individual addressing system using a cAOD

The first step towards the addressing system based on the cAOD was to design the telescope system which will sit in between the deflector and the imaging objective. I approached this in two steps first a simple Gaussian model was employed to reduce the parameter space and based on this findings the system was further investigated in a more sophisticated Zemax[1] simulation.

3.1. Gaussian model

Optimizing the optical system means to find a good compromise between competing parameters. We were considering mainly the spot size at the ion, the addressing range and the switching time. The most important figure is the spot size which has to be smaller than the ion spacing and will reduce the crosstalk for smaller values. The addressing range aims to cover the whole achievable ion string of ~50 ions with a spacing of 5 - 8 µm. The goal is to address all ions in the string to test the scalability of such a setup. The addressing pulse is shaped with a double pass acousto optic modulator (DP AOM) on the splitting board. Although the switching time (also called rise time) should be as fast as possible.

To estimate the smallest achievable spot after the objective we can compute the gaussian beam waist given the input beam diameter:

$$w = \frac{4\lambda}{\pi}\frac{f_{\text{eff}}}{2D_{in}}. \tag{3.1}$$

We introduce a factor of 2 in the denominator to get the beam waist. The wavelength of the addressing beam is $\lambda = 729\,\text{nm}$ and the effective focal length of the objective is $f_{\text{eff}} = 38\,\text{mm}$ (for 397 nm). To get the smallest achievable spot we set the input diameter equal to the pupil diameter [2] of the objective. The diffraction limited beam waist is $w_{diff} \approx 0.58\,\mu\text{m}$.

The addressing range in the paraxial approximation[3] is purely dependent on the input angle to the objective:

$$\delta_A \approx f_{\text{eff}}\ \theta \tag{3.2}$$

To find the total addressing range we have to find the maximal deflection of the beam entering the objective. The maximal deflection angle θ_{max} is given through the deflection of the cAOD θ_{aod} and the magnification M of the telescope: $\theta_{max} = \theta_{aod}/M$.

The rise time is linear in the input beam size and is given as [28]:

$$T_r = \frac{\beta D_{in}}{v} \tag{3.3}$$

---

[1] Ansys, Zemax OpticStudio

[2] This is the maximal aperture of a given lens system.

[3] The angle for all rays is small: $\tan\theta \approx \sin\theta \approx \theta$.

		Initial goal	Gaussian model	Zemax	final setup
Waist radius	[µm]	< 2	0.9	< 1.5	1.12
Addressing range	[µm]	~ 350	347	323	302.9
	[ions][4]	> 50	> 50	68	60
Input diameter	[mm]	< 6	3	3	3.1
Rise time	[µs]	< 10	3	-	-

Table 3.1.: Comparison between the desired specification and the selected parameters during the design process. Also the final achieved values are presented, they are further discussed below.

The constant $\beta = 0.66$ accounts for the gaussian beam shape. The acoustic velocity v of the AOD is 650 m/s.

In figure 3.1 the three parameters are plotted in terms of the two free parameters input diameter D_{in} and magnification M of the telescope. The input diameter is upper bounded by the cAOD aperture. The diameter at the Objective is directly given from the input diameter and the magnification : $D_o = MD_{in}$. This plot allows us to select a good combination of parameters: $D_{in} = 3\,\text{mm}$ and $M = 6.5$.

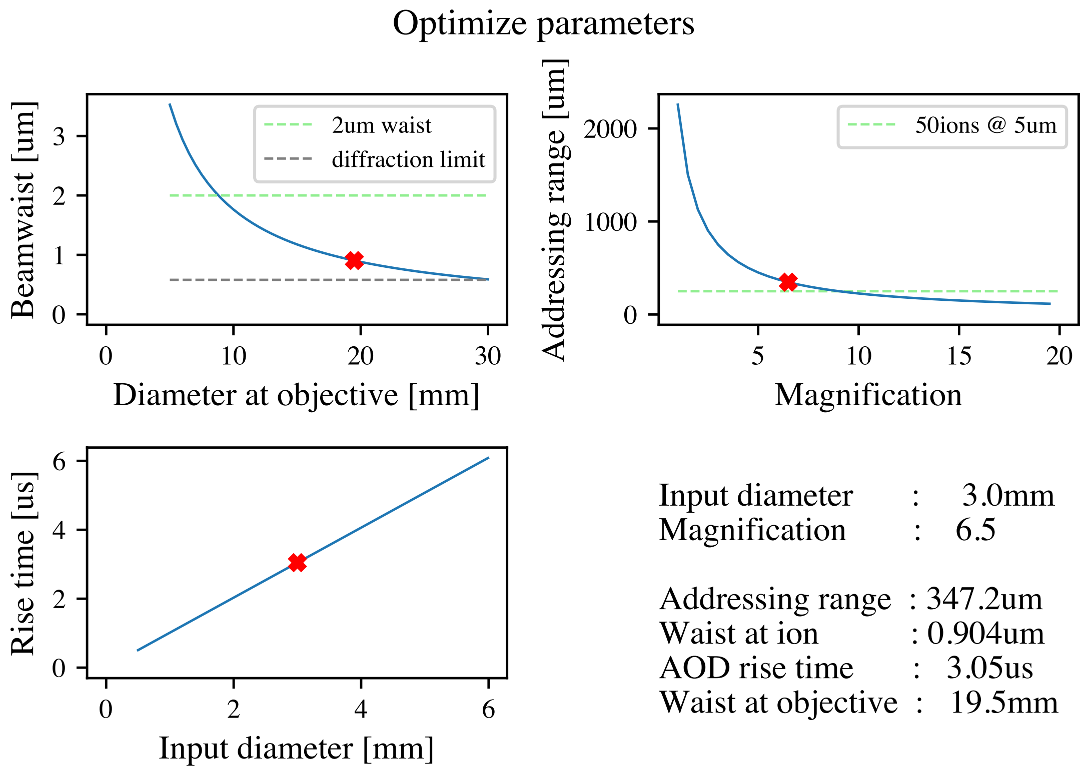

Figure 3.1.: Selection of the two free parameters input diameter D_{in} of the cAOD and magnification M of the telescope. The red crosses indicate the selected operation points.

---

[4] Assuming a spacing of 5 µm.

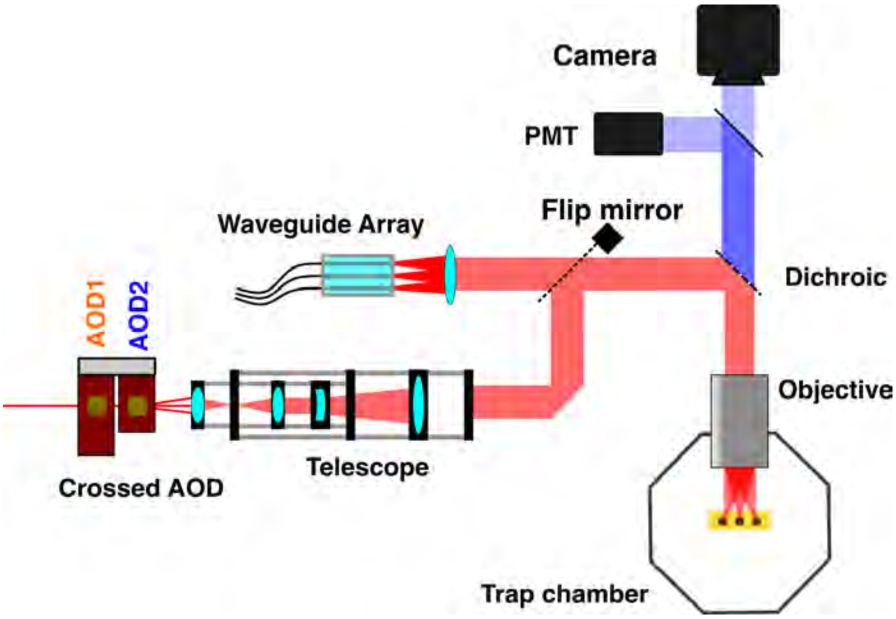

Figure 3.2.: Schematic of the imaging and addressing system. The dichroic is used to superimpose addressing beam with the imaging axis. The flip mirror can select between the cAOD or the WGA for the he addressing.

With the chosen magnification of 6.5 the next step is to find a combination of lenses to build the telescope. The selection is constraint through the resulting length of the telescope and the available lenses in the suppliers catalogues. As demonstrated in the work of Ralf Berner and Hendrik Timme a combination of Kepler and Galilean telescope can reduce the length [29, 18]. A Kepler telescope is a combination of two convex lenses with positive focal lengths, the telescope length is the sum of the both focal lengths. A Galilean telescope combines a concave lens with a convex lens. The telescope length is reduced to $l = f_+ - |f_-|$. This allows for a more compact design for the same magnification.

One constraint comes from the beam layout for the addressing. The cAOD beam is combined with the light exiting the imaging objective using a dichroic mirror. Additionally a flip mirror is placed to change the addressing between the cAOD and a WGA (figure 3.2). This predefined path fixes the minimum distance between the telescope and the objective. Additionally the telescope and cAOD have to fit on the baseplate of the experiment since at a later point the complete setup will be enclosed in a Mu-metal shield.

To select a combination of lenses I implemented a gaussian model for a two stage design of a Kepler and Galilean telescope. The selected combination of lenses is within the desired length constraints and also comes close to the needed magnification. In figure 3.3 the maximal deflected ray is indicated. We see that the beams are deflected by quite a bit and with the increasing size in the second telescope I want to use 2 inch lenses. As mentioned in [29] achromatic doublet lenses are used due to their superior focusing performance compared to plano-convex lenses. Aspheric lenses would also be interesting option since they have superior performance for deflected beams, but the available catalogue from Thorlabs was rather limited. Therefore I settled on achromatic lenses.

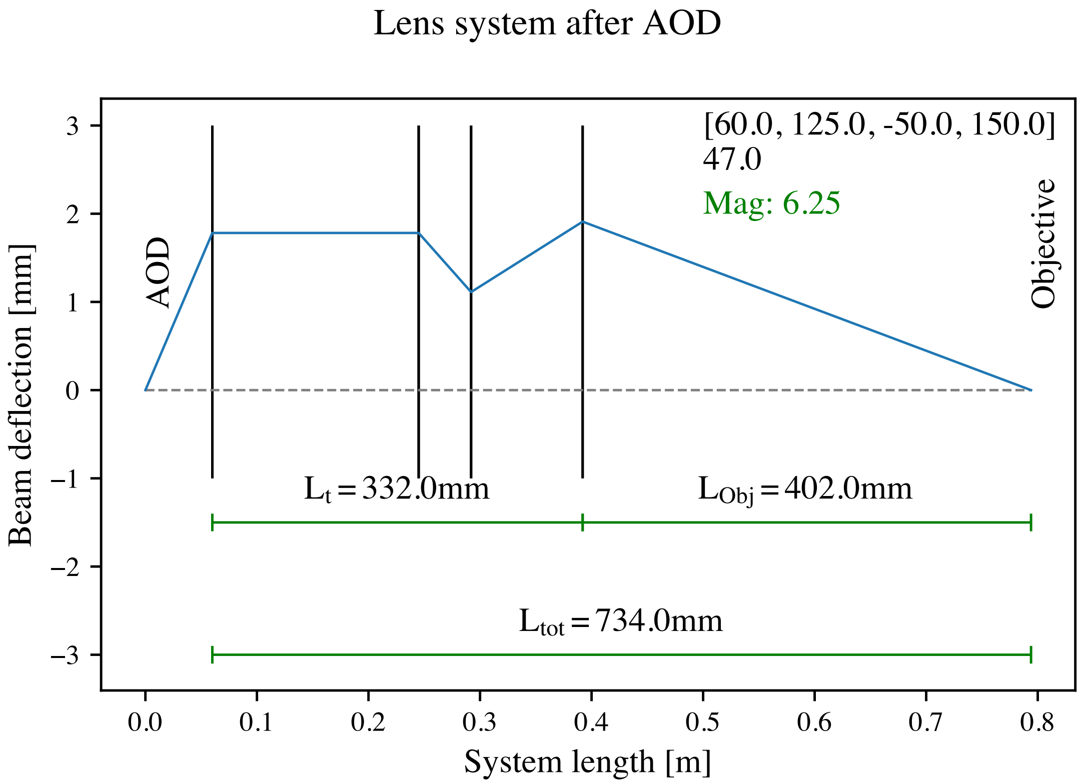

Figure 3.3.: Gaussian model of a telescope system with the chosen magnification. The bounds on the lengths are estimated from the CAD model. The y-axis indicates the center of the optical path for the maximal deflected beam.

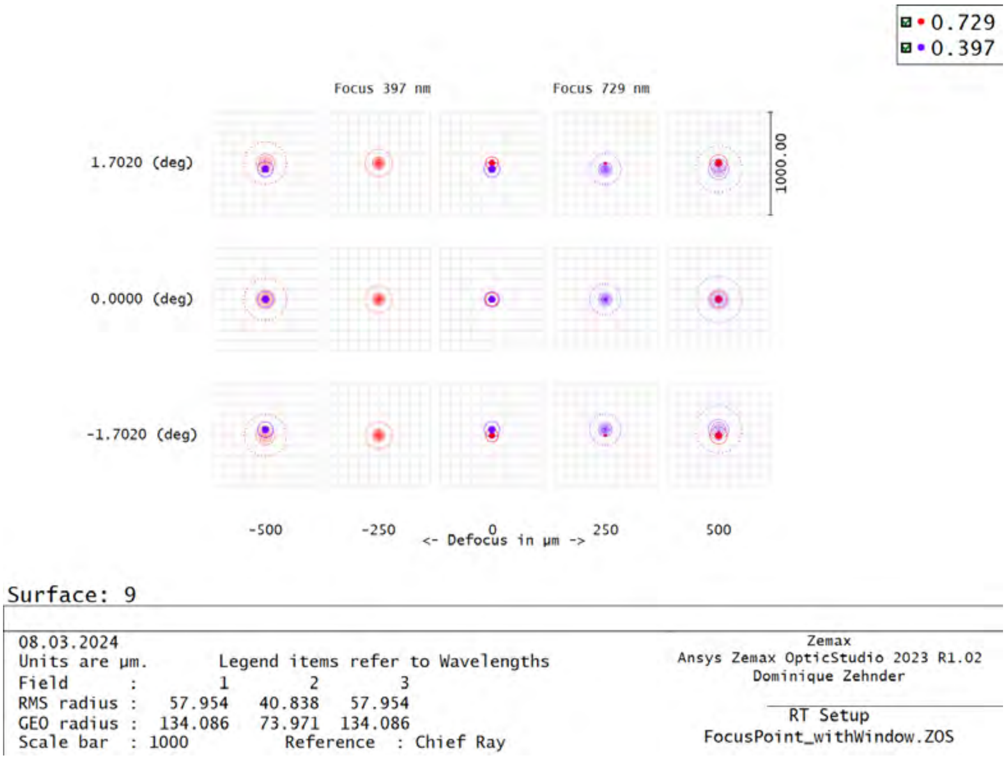

```
Surface: 9

08.03.2024                                                Zemax
Units are µm.       Legend items refer to Wavelengths    Ansys Zemax OpticStudio 2023 R1.02
Field        :        1         2         3                 Dominique Zehnder
RMS radius :    57.954    40.838    57.954
GEO radius :   134.086    73.971   134.086                    RT Setup
Scale bar  :  1000          Reference   : Chief Ray     FocusPoint_withWindow.ZOS
```

Figure 3.4.: Comparison of the focus position between 397 nm and 729 nm light. The offset distance is found to be $\delta_z = 473$ nm. Note the radius fits refer to the plane in between the two focal planes. Each row shows the simulation for a different incident angle. The input beams have a diameter of 22 mm. The colors indicate the wavelengths.

3.2. Zemax simulations

In the previous chapter the telescope was simulated with thin lenses. Now we want to simulate the real performance of the telescope including the imaging objective. Photon Gear the manufacturer of the imaging objective supplied a Zemax black box file. Zemax is a simulation tool which is based on raytracing. It allows to use accurate lens models of manufacturers and features a big toolkit for analyzing and optimizing optical system such as objectives and telescopes. This black box model allows to simulate light passing through the objective without revealing the design parameters of the objective's optical elements. This makes Zemax a good tool for simulating the addressing system.

Ion plane The objective serves two purposes, the collection of the fluorescence of the ion at 397 nm and the focussing of the addressing beam at 729 nm. The readout beam passes straight through the dichroic mirror and the addressing beam is reflected from the dichroic mirror (figure 3.2). It is important that the two planes for readout and addressing overlap. The objective should be optimized for this operation. To test this I sent two collimated beam with an diameter of 22 mm and compared the position of the foci (figure 3.4). It is important to note that the vacuum view port has an effect on the focal position and beam size. It is modeled as plain surface. From the simulation we find a shift of $\delta_z = 473\,\mu\text{m}$ between the two focal planes.

	Waist			Waist
System	min [µm]	max [µm]	addressing range [µm]	measured [µm]
$[60, 125, -40, 150^*]$	1.066	1.099	322.99	1.126
$[60, 125, -50, 150^*]$	0.561	0.599	403.41	1.251
$[60, 125, -40, 200^*]$	1.650	1.660	226.54	1.297
$[75^*, 150^*, -50, 150^*]$	0.527	1.332	411.09	-
$[80^*, 200^*, -50, 150^*]$	0.959	1.726	333.67	-

Table 3.2.: Comparison of the different simulated lens systems. The star denotes 2 inch lenses. Only systems with 1 inch lenses for the first two lenses were tested. The waist simulated by Zemax is only an estimate from all traced rays. Based on the measured waist size the first system is used.

Telescope I used the Thorlabs lens catalog in Zemax to obtain the models for the possible achromatic lenses I wanted to simulate in the telescope. One has to pay attention to the orientation of the lenses to get a good performance. Because I experienced some instabilities when I tried to optimize all parameters of the lens system at once I chose to build each of the partial telescopes individually and optimize them for perfect collimation. Then I would combine them to the full system and only in the end I would optimize one parameter at a time to optimize for the smallest spot size.

I tried several combinations of lenses an overview can be found in table 3.2. The lens systems are labeled in the compact notation: $[a, b, c, d^*]$ where a and b are the focal lengths for the first Kepler telescope 1 and and c and d are the Galilean telescope. The star for lens d indicates an 2 inch lens diameter.

The optical performance is the most important factor of the selection of the effective system. But also the opto-mechanics and mounts for the chosen lenses need to be available. With all this considerations we decided on the 1 inch version of the first telescope part because the mounting of the optics provides more flexibility and the negative focal length lenses are only available in 1 inch anyways. The last lens has a diameter of 2 inch to have a big enough aperture.

In figure 3.6 the performance of the final lens system $[60, 125, -40, 150^*]$ is simulated. We see the spot diameter is below 2.6 µm for the whole addressing range. The shape of the beam is round for approximately half of the range and is only slightly distorted towards the ends. We can see that the expected addressing range of 323 µm is slightly smaller than the desired addressing range. But it is still feasible to address more than 50 ions with a spacing of 5 µm. The lens system with the $f_3 = -50\,\mathrm{mm}$ performed much worse in the test setup compared to the simulated value. Thus the system with $f_3 = -40\,\mathrm{mm}$ is used.

Crosstalk We can also look at the crosstalk between the addressing beam to its neighboring ions. In figure 3.5 the Huygens point spread function[5] for the center beam and the maximal deflected beam is shown. We see that the power is dropping fast and for the neighboring ions we expect a crosstalk in the order of 1×10^{-4}. We can clearly see some distortions to the beam shape for the outer points (figure 3.6a) This also translates

---

[5] This method traces a grid of rays from the input to the image plane. Each point of the wavefront is treated as a plain wave and propagated to the image plain. The interference of all points is computed and squared.

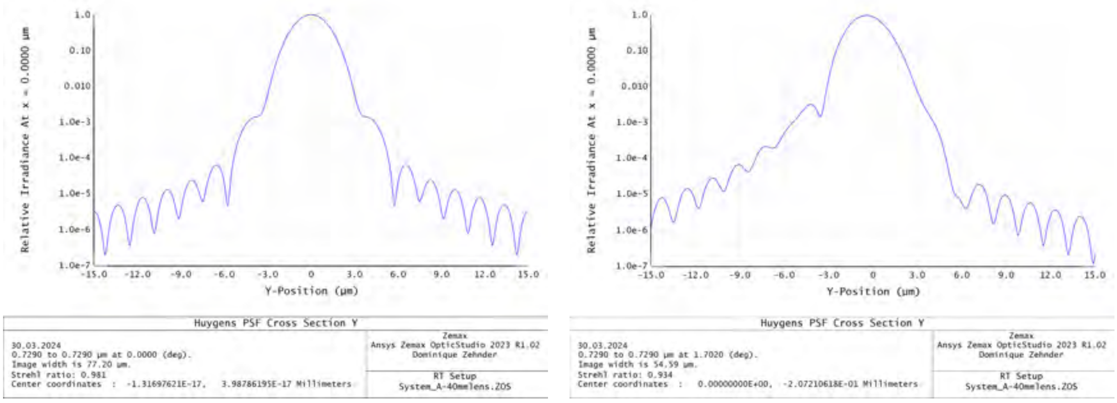

(a) center beam

(b) maximal deflected beam

Figure 3.5.: Estimated crosstalk to the neighboring ions based on the Huygens point spread function. The plot is normalized to the maximal irradiation. For the center beam the crosstalk to neighboring ions at 5 µm is around 1×10^{-4}. For off-center beams the crosstalk is non-symmetric. Toward the end of the addressing range the crosstalk slightly increases.

to a skewed crosstalk. In both cases the crosstalk is in the same order of magnitude as implementations of comparable systems.

The simulations validates the chosen system and all specifications are fulfilled (table 3.1). Even though the model takes many effects into account we have to assume a worse performance for the real setup. This comes mainly from the large beam at the end of the telescope which will be slightly clipped in a 2 inch mirror. Also the alignment will introduce some errors.

3.3. Crossed AOD mount

In all of the following experiments the cAOD device DTSXY-400-730 from AA opto-electronic is used. The device consists of two separate AODs which are mounted to an aluminum base plate. The relative alignment is adjusted by the company and fixed with glued screws.

The device available in the lab is optimized for a collinear propagation of the +1 +1 diffraction order. This optimization is not the ideal one for our application but due to long lead times a replacement of the device was not feasible. As described in chapter 2.5 this device can still be used with minor modifications to the setup. In table 3.3 the key characteristics of the device are summarized.

The kinematic mount of the cAOD enables the positioning of the device in all 6 spacial degrees of freedom. The construction is based around four OptoSigma stages (table 3.3). The XYZ-axis allow for 12 mm adjustment the rotation axes for ∼5° adjustment around the center point of the two AODs devices. The mechanical construction is the same as presented in the thesis of Ralf Berner [29]. Some minor changes to the hole-pattern of the base plate were made to have more flexibility. Also the L-shaped adapter was made symmetrically to allow for the right handed version of the goniometer stage (figure 5.3b).

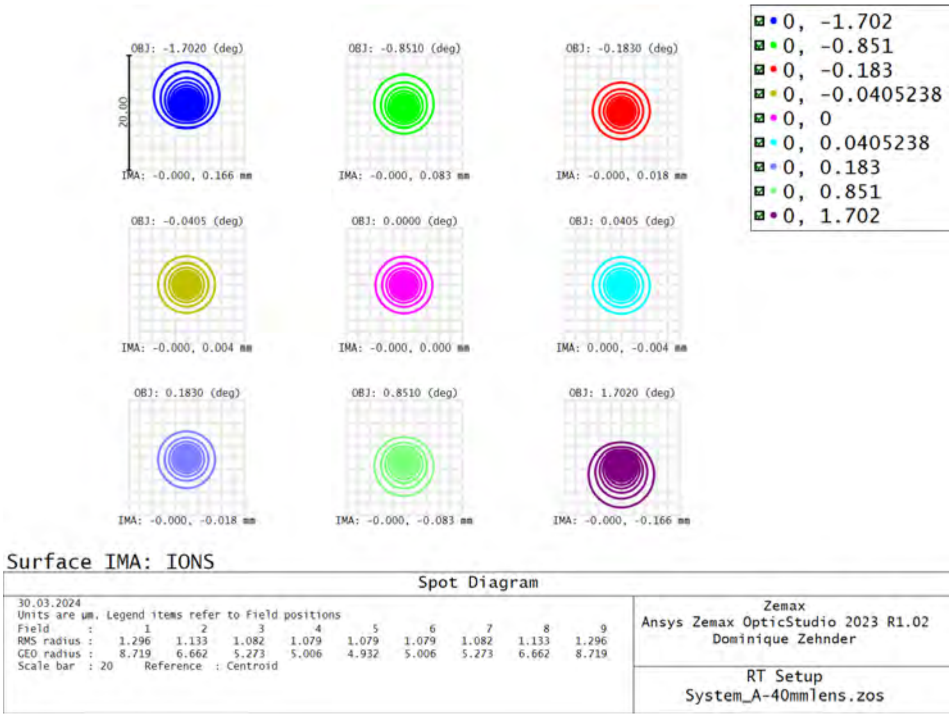

```
30.03.2024
Units are µm. Legend items refer to Field positions
Field       :        1        2        3        4        5        6        7        8        9
RMS radius  :    1.296    1.133    1.082    1.079    1.079    1.079    1.082    1.133    1.296
GEO radius  :    8.719    6.662    5.273    5.006    4.932    5.006    5.273    6.662    8.719
Scale bar   : 20     Reference  : Centroid
```

(a) Spot size and shape for different deflection angles

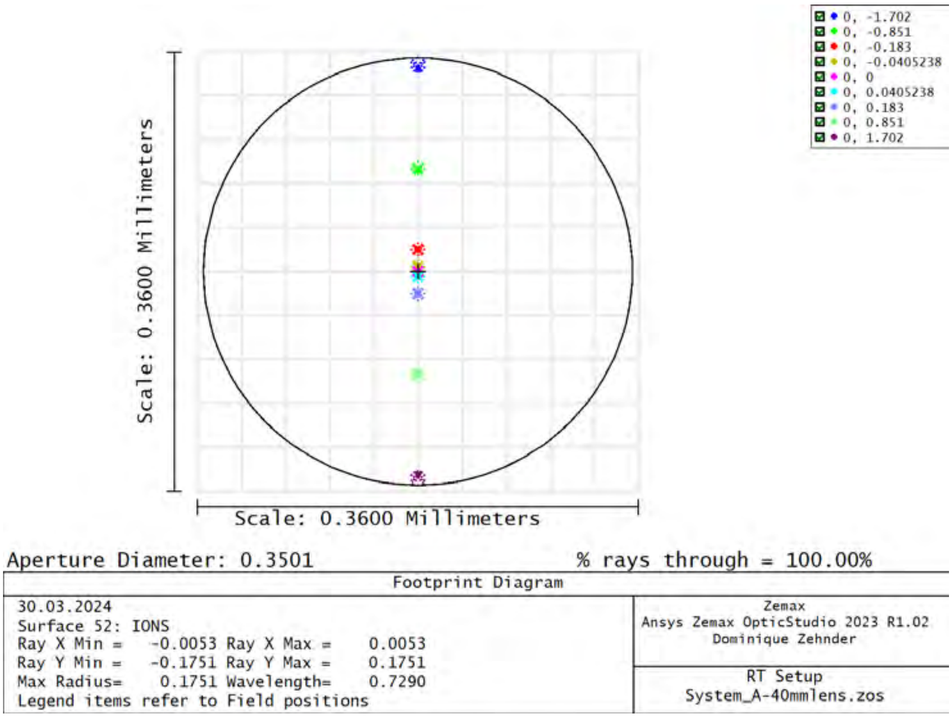

```
30.03.2024
Surface 52: IONS
Ray X Min =    -0.0053 Ray X Max =    0.0053
Ray Y Min =    -0.1751 Ray Y Max =    0.1751
Max Radius=     0.1751 Wavelength=    0.7290
Legend items refer to Field positions
```

(b) Footprint of the beams in the ion plane

Figure 3.6.: Zemax simulation of the final lens system $[60, 125, -40, 150^*]$. In (a) the spot size and shape is depicted. Each of the beams starts at a different angle between ±1.702° to simulate the deflection of the cAOD (color indicates the angle). We find the beam waist is below 1.3 µm over the total addressing range. In (b) the position of the deflected beam in the ion plane is simulated. We find an estimated addressing range of 323 µm.

	DTSXY-400-730
Center frequency	110 MHz
Bandwidth	38 MHz
Scan angle	42 mrad^2
RF power	<2 W
Laser beam diameter	0.5 - 6 mm
Acoustic velocity	650 m/s
Optimization	X:+FC, Y: +FC
Diffraction efficiency	≥ 58 %
Colinear emission	1th order

(a) cAOD Device

Model	Axis	Range
TSD-605S	X, Y, Z	±6 mm
KSP-656M-M6	AOM 1	±5°
KSP-406MR	AOM 2	±5°
GOHT-40A40BMSR	addressing angle	±7°

(b) translation and rotation stages

Table 3.3.: (a) Specifications of the cAOD tested @730 nm according to data sheet (appendix A.1). The optimization +FC means the +1 order at the center frequency is optimized. (b) Translation stages used to position the cAOD assembly.

3.4. Telescope

The optical system used for expanding the beam of the cAOD before the imaging objective is described above. The lens system needs to be mounted in a sturdy way and also have enough degrees of freedom. The telescope is chosen similar to the design of [29]. The two inch cage system was extended over the entire length to increase the stiffness. Due to the dimensional constraint of the optical table an 45° mirror was placed to reduce the length of the telescope. In addition the cage system was design such that one lens can be motorized to fine adjust the focus position on the ions (figure 3.7a).

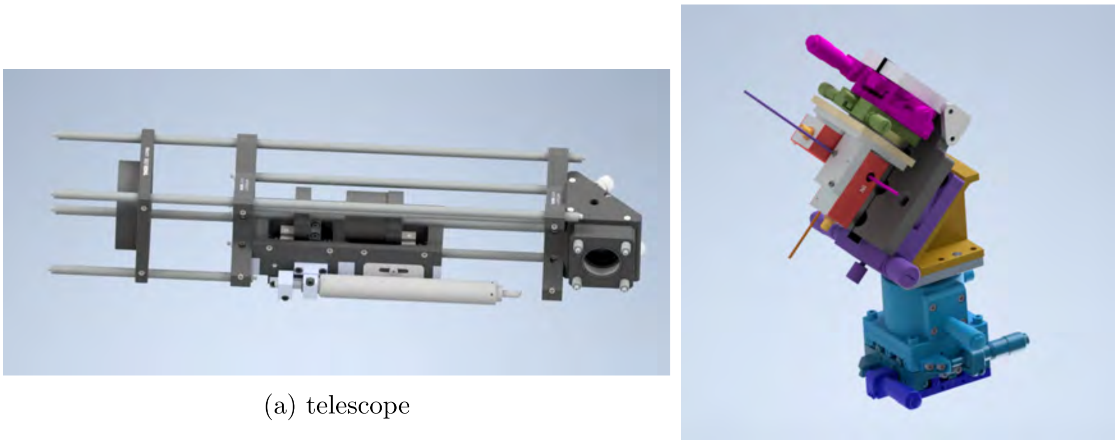

(a) telescope

(b) cAOD stage

Figure 3.7.: (a) Renderings of the motorized telescope system used to expand the beam after the cAOD. (b) Assembly for mounting the cAOD. The six stages allow to position the cAOD in all 6 degrees of freedom. The rotation stages rotate around the center of the two AODs.

4. Testing individual addressing system based on a cAOD

In order to characterize the addressing system before integrating it in the experiment a test setup is used. This enabled better access to all components and no interruption for the working setup. Following the two used test setups are presented. In chapter 4.2 to 4.4 the results obtained from the setups are presented.

4.1. Test setup

4.1.1. AOD operation

The purpose of the first setup was to test the operation of the AOD without any additional optical components. This tests includes the kinematic mount of the cAOD, the laser system, the RF source and the experimental controls (figure 4.1).

The RF signal for controlling the cAOD is generated by a Moku:Pro[1]. This highly customizable device has four RF in- and outputs with various operations modes. For this test a basic signal generator module was used. The 10 MHz clock reference for the Moku is provided from an GPS clock reference [2]. The signal is boosted by an RF amplifier with a fixed amplification of 35 dB[3]. The RF power was adjusted to 1.2 W as specified in the data sheet.

The tests were performed with a Toptica diode laser with the desired wavelength of 729 nm. The light is amplified in a tapered amplifier and brought to the setup in a polarization maintaining single mode fiber [4]. The polarization of incoming light is set to be linear with a combination of a $\lambda/2$ and $\lambda/4$ waveplates from Altechna. The input power was between 5 - 10 mW. To collimate the input beam a Schäfter+Kirchhoff[5] fiber collimator was used. The measurements were taken with a monochromatic CCD camera from Thorlabs [6](table 4.1). To adjust the power to a suitable power level neutral density (ND) filters were placed. The camera was placed approximately 40 - 50 mm after the cAOD such that the beam at the center frequency is entering the camera orthogonal. The experiments were controlled from a python notebook which interfaces the MOKU API over the network. The RF frequencies were scanned by the script and images were taken.

---

[1] Liquid instruments, Moku:Pro

[2] Standford Reasearch Systems, FS740

[3] creotech, Booster

[4] Thorlabs, P3-780PM-FC5

[5] S+K, 60FC-4-M18-10

[6] Thorlabs, Kiralux CS235MU

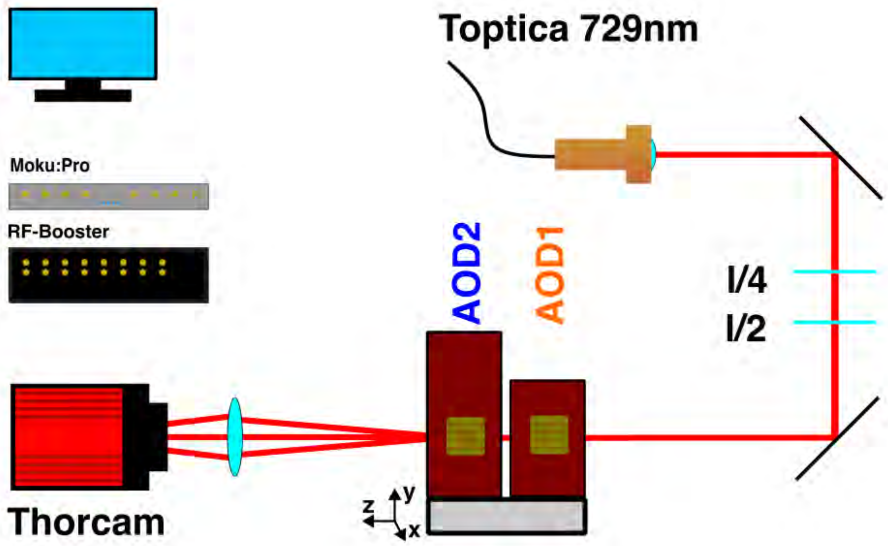

Figure 4.1.: Setup for testing the operation of the cAOD. A lens is used to bring the beams onto the camera sensor. The input beam has a diameter of 3 mm. The image is not to scale.

4.1.2. Telescope characterization

This setup allows to test the addressing system under realistic conditions. In figure 4.2 all components are shown as a schematic and in image 4.3 a picture of the used setup us depicted. The setup can be divided into three parts: the addressing setup, simulation of the readout optics and the imaging setup.

Addressing The 729 nm line consists of three sub assemblies: the input optics, the cAOD and the telescope system. The input optics and the cAOD mount are identical to the setup described in section 4.1.1. The output beam of the cAOD is directed into the telescope assembly presented in section 3.4. The first Kepler telescope has an 45° mirror in the middle. The two middle lenses are on translation stages. Only the last lens has a 2 inch diameter.

The alignment procedure for the system was the following:

1. Input system
   - i Collimate the input fiber coupler with a shear plate interferometer[7].
   - ii Align beam on center axis of the input cage system.
   - iii Set a linear polarization with the two wave plates using a polarizing beam splitter (PBS).

---

[7] The shear plate interferometer is a gauge for the collimation of a laser beam. Thorlabs, SI254

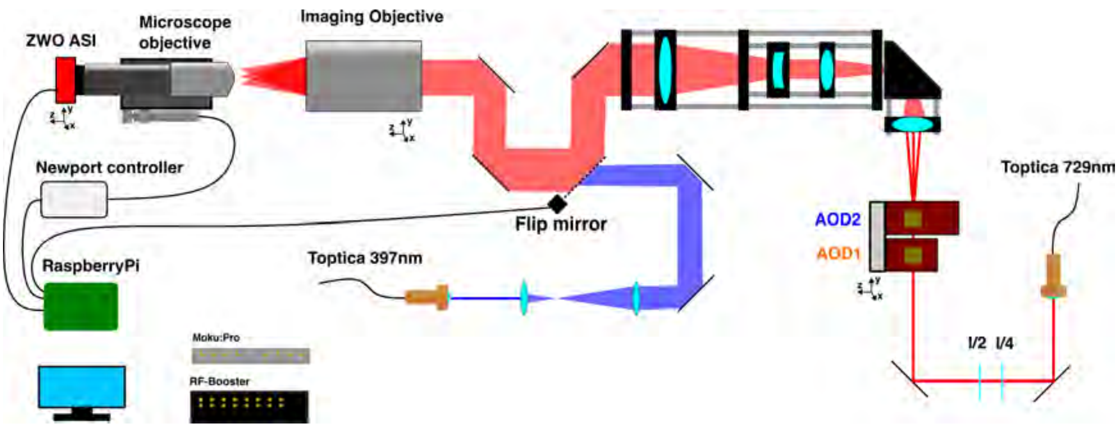

Figure 4.2.: Setup used to test the optical system for addressing. In addition to the 729 nm addressing beam (red), the ion readout is simulated with an 397 nm beam (blue). The two beams can be switched with a flip mirror. The imaging objective and the camera system are mounted on xyz-stages for easier alignment. The telescope is built in a 2 inch cage system from Thorlabs to increase the stability.

2. Telescope
   - i Start with cage construction with only the 45° mirror and align the input beam along the center axis.
   - ii Insert the lenses for the first telescope part and collimate the output beam with the shear plate[8].
   - iii Insert the lenses for the second telescope and collimate the output beam with the shear plate.
3. Place AOD
   - i Only now slide in the cAOD assembly and place it such that the beam enters the aperture.
   - ii Align the lower rotation stage for first AOD.
   - iii Align the upper rotation stage for second AOD.
   - iv Optimize x, y and z axis.
   - v Optimize power with the $\lambda/2$ wave plate.
   - vi Fine adjust the beam onto the axis of the telescope with the two input mirrors and repeat the last four steps.
   - vii Adjust the goniometer stage to align addressing axis with the ccd chip.

The beam from the telescope is directed toward the objective via the flip mirror[9] and two kinematic mirrors which give the necessary degrees of freedom for alignment. This part of the setup uses 2 inch optics. If the flip mirror is in the down position the 397 nm line will be directed to the objective.

---

[8] Knive edge measurements performed validate that the shear plate is a good method for setting the collimation (appendix B.5)

[9] Thorlabs, MFF102/M

	Thorlabs Kiralux CS235MU	ZWO ASI290MM
Sensor	-	Sony IMX290LQR
Resolution	1920x1200	1939x1096
Pixel size	5.86 µm	2.9 µm
Quantum efficiency @729 nm	$\sim 35\,\%$	$\sim 80\,\%$
Read noise	$< 7.0\ e^-$	$3.2\ e^-$
Full well capacity	$\geq 30\,000\ e^-$	$14\,600\ e^-$
ADC resolution	12	12
Dynamic range	up to 75 dB	12 bit (72 dB)

Table 4.1.: Specifications of the used camera according to data sheet.

Readout The 397 nm beam is used to simulate the position of the ion readout. The light is supplied from another Toptica diode laser. The light is directed to the setup in a polarization maintaining fiber and collimated with an S+K collimator[10]. After the collimator a telescope with $f_1 = 35$ mm and $f_2 = 300$ mm increases the beam diameter to ∼20 mm. The beam is then overlapped with the addressing beam using the flip mirror.

Imaging system The imaging part consists of the high numerical aperture (NA) objective[11] which is used for ion readout and addressing. And the camera system to measure the beam characteristics. We aim for a diffraction limited spot size in the order of 1 - 2 µm beam waist. Measuring such small optical beams is not straight forward. The measurements were performed with an ZWO ASI scientific camera[12] (table. 4.1). Since the pixel size is 2.9 µm a microscope objective is used to magnify the waist. I used two different objectives a 10X Nikon Plan Fluor (NA=0.3) and a 50X Olympus MPlanApo N (NA=0.95). The 10x allowed for measurements over the entire addressing range but could not quite resolve the smallest waists. Thus the 50x objective was used. Both objectives were calibrated with a resolution target[13].

For alignment the camera setup was mounted to a XYZ-translation stage [14]. Since the Rayleigh range of the expected addressing beam is below 10 µm the z-axis (along the optical axis) is equipped with a motorized actuator[15]. In addition to the increased resolution of 0.1 µm (for unidirectional motion) this also allows to automate some measurements.

As mentioned in the simulation chapter the vacuum viewport is part of the objective design. For the measurement an AR coated 4 mm Fused Silica viewport[16] was placed between the addressing objective and the camera setup.

---

[10] S+K, 60FC-SF-4-A11-01
[11] Photon Gear, NA=0.4 EFL=38 mm, EPD=30.04 mm (appendix A.2)
[12] ZWO, ASI290MM (mono)
[13] Thorlabs, NBS 1952
[14] 3x OptoSigma, TAM-401S
[15] Newport TRA6PPD, with SMC100PP controller
[16] Lesker SKU029886, 4 mm Corning HPFS 7980 Fused Silica, AR coating at 729 nm on both sides

Measurement control For the different measurements the cAOD has to be synchronized with the camera, stage and the flip mirror. The Moku is interfaced over the python network API. To make the integration of the other hardware such as camera, stage and flip mirror easier they were all connected to a RaspberryPi 4 B. A python script running on the raspberry pi exposed the controls to the lab network such that the devices can be orchestrated from the measurement notebooks. This high level of automatization enables fast and reproducible measurements.

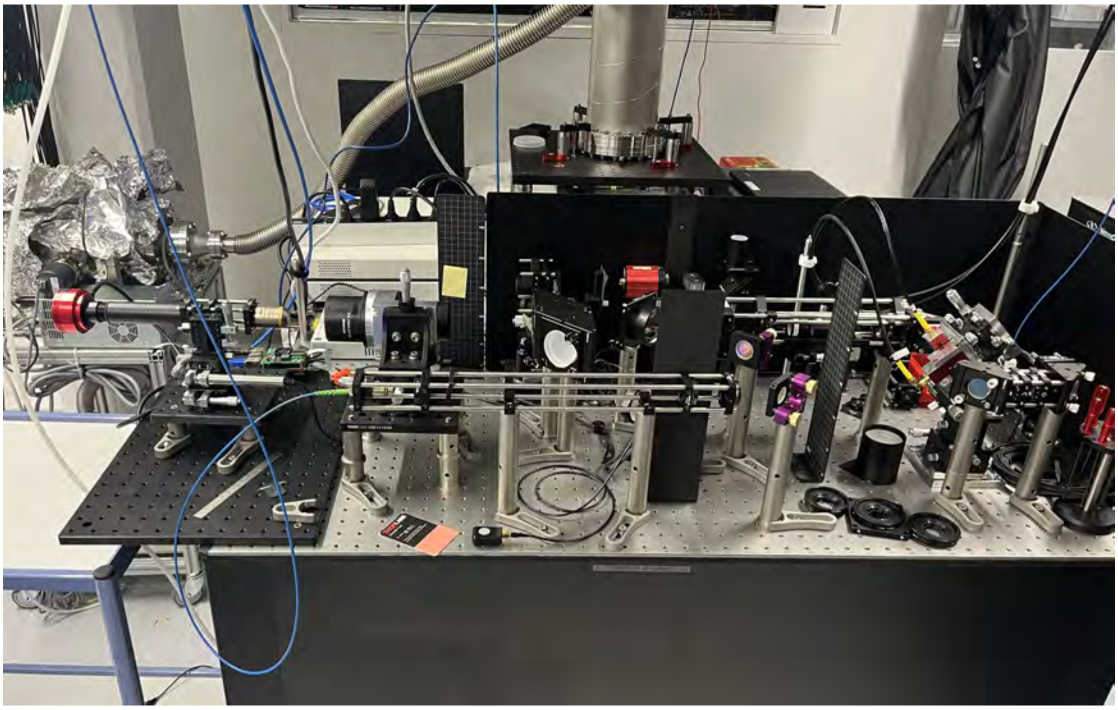

Figure 4.3.: An image of the test setup as described in this section. The cAOD is placed on the right hand side. The camera and objective are placed to the left. The beam path is elevated due to the height of the cAOD mount.

4.2. AOD characterization

In chapters 2.4 and 2.5 the operation principle and control of a cAOD is explained in detail. To verify the supplied parameters and ensure the proper operation of the device the setup described in chapter 4.1.1 is used.

The cAOD was controlled with the different proposed modes of operation from chapter 2.5 and the power at the output was measured with a camera. A linear camera response is assumed. This allows us to see the usable bandwidth of the device (figure 4.4). The numbers represent the diffraction order, the signs describe how the addressing frequendy Δ_A is added or subtracted from the individual AODs. The bandwidth is directly proportional to the achievable addressing range.

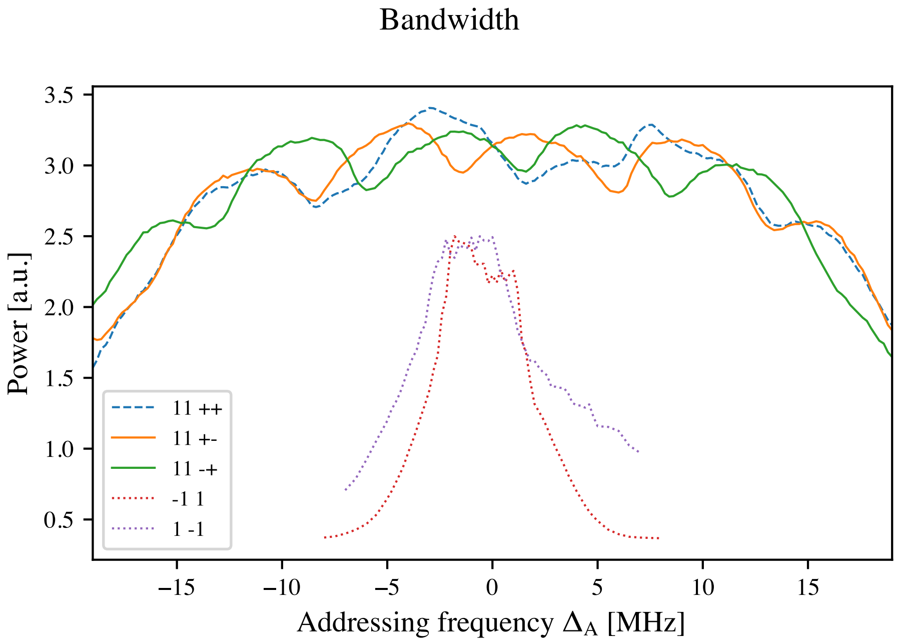

Figure 4.4.: Diffraction efficiency of the cAOD plotted against the RF drive relative to the center frequency. The dotted lines indicate the mode of operation where no net frequency shift is introduced ($\delta_f = 0$). The solid lines represent the operation mode where a net shift of twice the center frequency is introduced ($\delta_f = 2\Omega_0$). The dashed line has a frequency shift depending on the addressing position.

The usual mode of operation with zero frequency shift is not feasible, since the particular device available during this thesis was optimized for the +1 +1 diffraction order. If the device is operated in the not optimized configuration this results in power losses and a significant reduction of the bandwidth to ~10 %.

The operation in the +1 +1 order where both AODs use the same frequency is not ideal for addressing due to the variable frequency shift (figure 4.5a). If the devices are driven with two different frequencies $f\Omega_0 \pm \Delta_A$ then the resulting frequency shift is non zero but constant, which makes a correction simpler (see chapter 2.5). Which mode of operation is chosen (+- or -+) does not mater as we can see from the bandwidth measurement. The two lines are mirrored around the center frequency (figure 4.4).

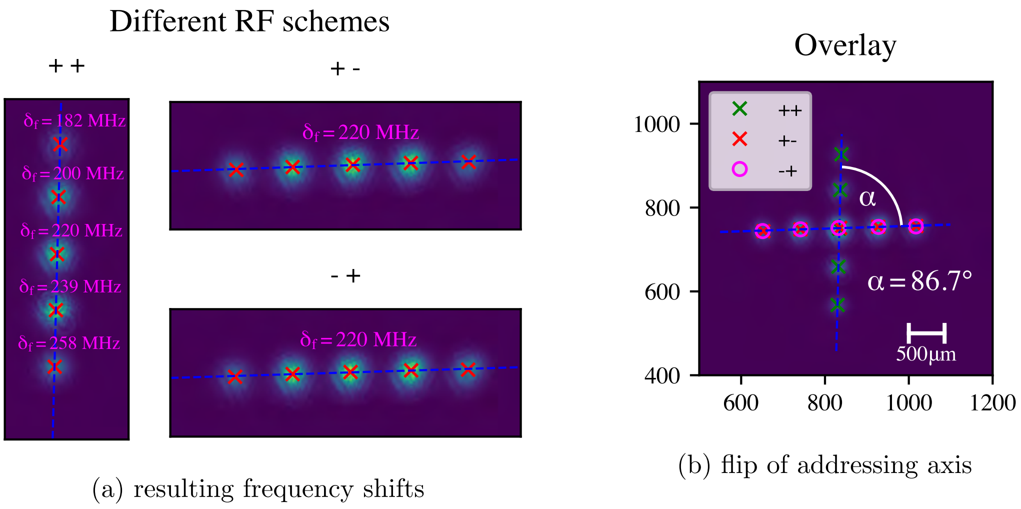

(a) resulting frequency shifts

(b) flip of addressing axis

Figure 4.5.: Deflection of the beam for different operation modes. All measurements are performed on the +1 +1 diffraction order. The signs indicate how the addressing frequency Δ_A is modulated to the center frequency of the two AODs. In (a) each image is the sum of 5 measurements. The resulting optical frequency shift δ_f is indicated. (b) All three images are overlayed. We see the addressing axis changes between the modes. The angle is not perfectly 90° as we would expect.

This change in operation scheme leads to a 90° rotation of the addressing axis (figure 4.5b). The overlay of both measurements show a small deviation of 3.4°. This comes likely from a miss alignment between the two AODs. This additional 90° rotation and the small error can be corrected with the cAOD mount and have no further impact on the operation in the setup.

4.3. Spot characterization

This chapter presents the results which characterize the beam that can be expected at the ions position. This test combines the addressing telescope (lens configuration $[60, 125, -40, 150^*]$ see chapter 3) and the imaging objective. For all measurements the setup is described in chapter 4.1.2.

4.3.1. Focal plane overlap

The imaging and addressing objective used in the setup is optimized for the operation with trapped ions experiments in vacuum. This optimization includes the two wavelengths (729 nm for qubit control and 397 nm for readout) but also other factors such as the vacuum viewport are taken into account. Besides a high NA of 0.4 the objective should also overlap the focus plane of the addressing and imaging light.

This overlap is important since the addressing and the imaging will happen in the same experimental sequence. Small errors in the position can be corrected by 'misaligning' the optics before the objective such that the beam is not perfectly collimated. The Zemax mode predicts a separation of the two foci of $\delta_z = 473\,\text{nm}$ (chapter 3.2).

For this measurement the camera with the 50x objective was scanned over the expected separation. For each position an image of the imaging beam and for the addressing beam was taken. The switching was done with the flip mirror. The stability of the flip mirror

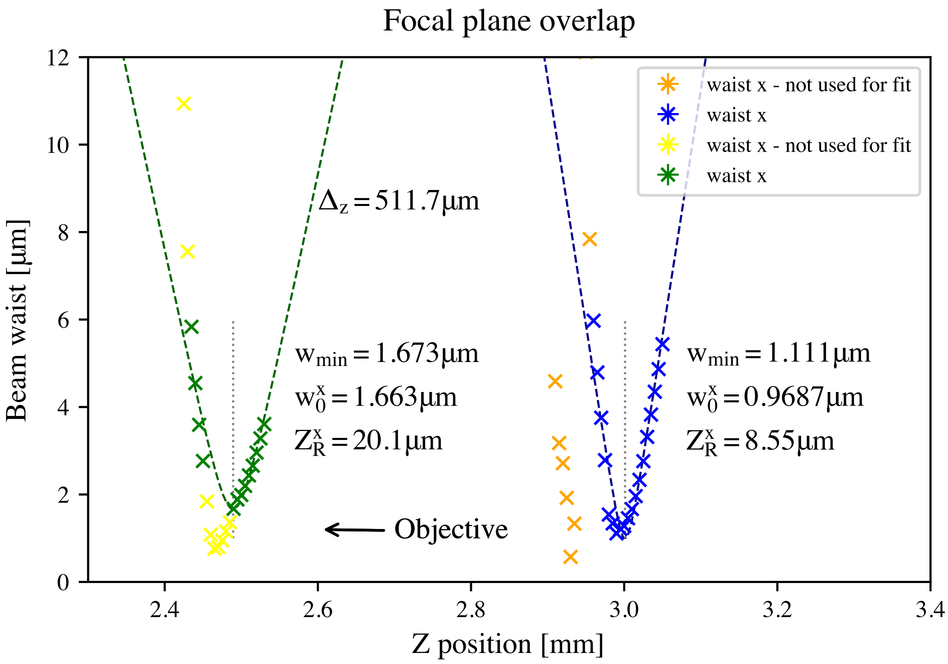

Figure 4.6.: Comparison of the z-position of the imaging and addressing focus. The waists are obtained from a 2D gaussian fit. The indicated z-position has an arbitrary zero point toward the objective. Some data points experience a strong airy pattern and cannot be fitted with a gaussian and are thus excluded from the waist fit. The measured difference in the focus position is $\Delta_z = 511.7\,\mu\text{m}$

was tested and is good enough for this application (appendix B.2). A 2D gaussian was fitted to the images. This obtained waist for major and minor axis are averaged and used for the beam waist fit in figure 4.6. Note the outliers were not used for the fit and come from the fact that the beam toward the objective experience some airy patterns.

The measured separation of 511.7 µm is in agreement with the simulation (chapter 3.2). The deviation can come from not perfectly collimated input beams. In a test, the position of the 729 nm beam could be overlapped with the imaging focal point. For this the last lens of the addressing telescope was adjusted by ∼20 mm. In this process the beam size only increased slightly. In the final setup we will more likely aim for the optimal addressing focus. The imaging system can be slightly adjusted since it is more forgiving because only the two ions need to be seperated.

4.3.2. Waist size

The waist of the addressing beam has to be smaller then the ion spacing, such that it will only address a single ion. A smaller spot will also increase the power in the focus which enables faster Rabi oscillations. To quantify the achievable spot size of the 729 nm beam is investigated. For this scan a resolution of 0.5 µm was chosen to properly resolve the the waist with an Rayleigh length in the order of 10 µm. The measurement was performed at the center of the addressing system for a drive frequency of $\Omega_{1,2}$ =110 MHz.

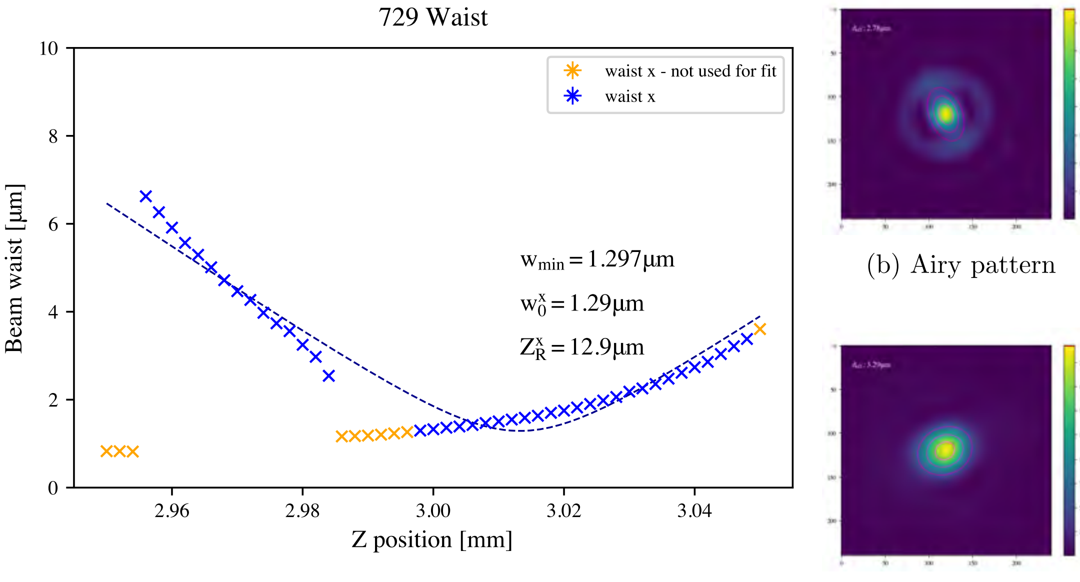

(a) Beam waist

(b) Airy pattern

(c) Gaussian shape

Figure 4.7.: (a) Beam waist of the 729 nm addressing beam for center of the addressing range (RF drive at 110 MHz). The excluded points resemble more an airy pattern (b) than a gaussian beam (c) and are thereof excluded. The measured minimal waist (measured at $1/e^2$) is 1.126 µm which is a nearly limited by the objective's performance.

In table 3.1 the comparison of the measurement and theoretical values show that we achieve nearly the simulated spot size. This spot size will allow for individual addressing on an ion string with 5 µm spacing between the ions.

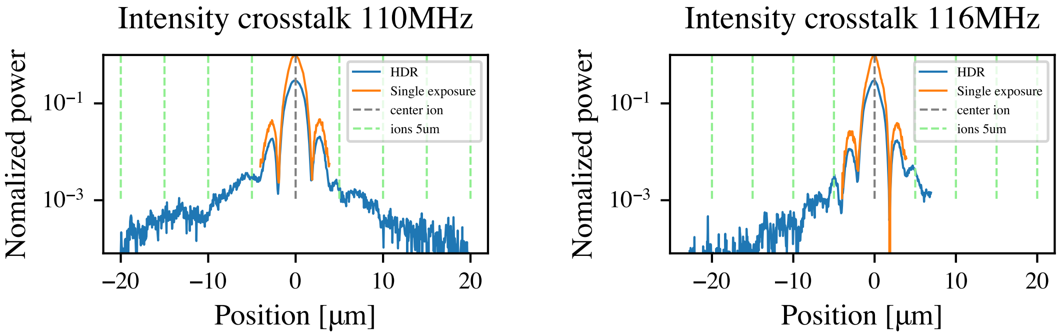

(a) Center beam $f_A = 110\,\mathrm{MHz}$ (b) Maximal deflection $\Delta_A = 6\,\mathrm{MHz}$

Figure 4.8.: Comparison of an x-slice through the intensity maximum for two different spots. The addressing range was limited to ±6 MHz du to the limited field of view of the 50x imaging objective. The blue line for the high dynamic range (HDR) images underestimate the center peak, they were scaled to be the continuous extension of a single exposure image. The green lines indicate the position of the neighboring ions with a spacing of 5 µm. The crosstalk is in the order of $\sim 3 \times 10^{-3}$.

4.3.3. Crosstalk

One of the most important figure of merit for an addressing system in a real world application ist the crosstalk between ions. To measure the crosstalk one needs to employ a measurement device which has a high dynamic range. The dynamic range is the ratio between the smallest resolvable unit and the maximum value of a sensor. The effective crosstalk is best measured directly with the ions. To get an idea already from the test setup the measurements were also taken with the camera. In table 4.1 the parameters of the used camera are listed. We see that from the given dynamic range we can maximally resolve a crosstalk of 2.44×10^{-4}. We have to consider also the residual background due to stray light which is entering through the objective and the sensor noise. This reduces the effective dynamic range to $\sim 5 \times 10^{-3}$. [17] To get better accuracy we can use multiple images where the exposures double. We can then add the images normalized by their exposure time and can recover some of the lost dynamic range. In this method I assume a linear CCD response. This method also will overestimate the waist since there might be slight jitter between the images. In addition the maximum intensity of the peak is under estimated because the sensor is saturating for the longer exposures. To address this issues the obtained crosstalk slice can be renormalized such that it is continuous with a measurement of one single image. In figure 4.8 the crosstalk for two addressing positions are plotted.

The measurement indicates a crosstalk in the order of 3×10^{-3}. This is higher than the results from the simulations. This has to be expected since the real setup will not be perfectly aligned and thus the spot quality will degrade. This measurement was taken at the position of the beam waist. This does not have to be the point of the smallest crosstalk due to the observed airy rings. A small offsets in z-direction might benefit the crosstalk (see cross sections in figure 4.9).

---

[17] The background of the images was usually between 20 and 50. The usable dynamic range is than reduced to $30/4096 \approx 0.005$

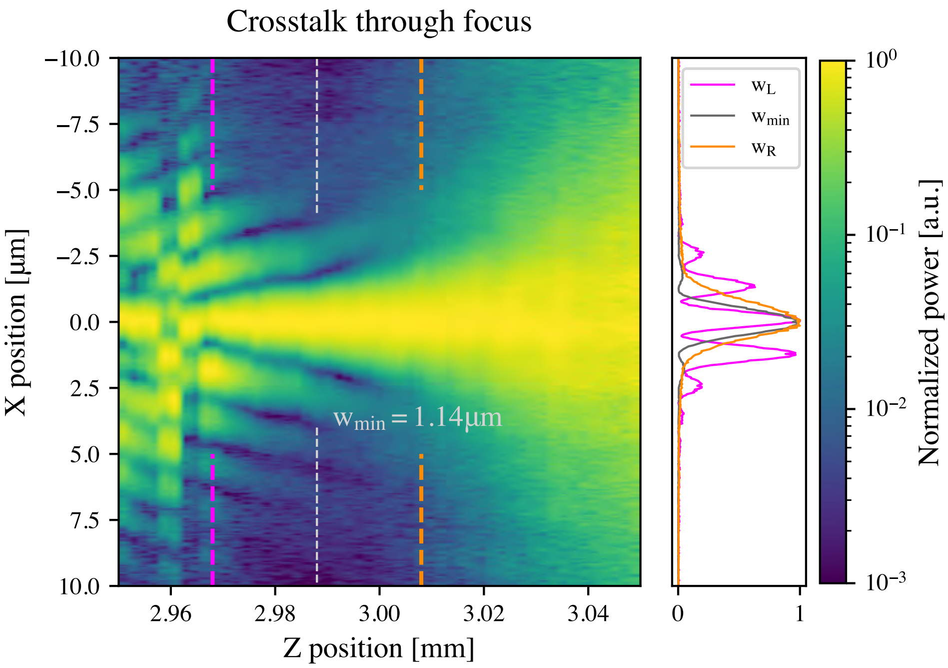

Figure 4.9.: Crosstalk map through the focus. Each column represents the crosstalk at the fitted gaussian maximum. We see the effects of the airy pattern towards the objective. The optimum z-position is a balance between tight focus and crosstalk of side lobes. To the right two cross-sections at an offset of ±20 µm are shown.

For the deflected beam in figure 4.8b we can observe a slight increase of the crosstalk away from the center. This is in good agreement with the simulations. This comes from aberrations from off-axis beam paths.

The effect of the z position is visualized in figure 4.9. The gray dashed line indicates the position of the smallest gaussian fit. See that the crosstalk does not increase significantly for small errors in the waist alignment. This indicates a stable operation of the setup will be possible

4.3.4. 200 mm lens

Because the beam waist is a bit bigger than the diffraction limited waist. I tried an additional telescope configuration. For this I exchanged the last lens and increased the focal length from 150 mm to 200 mm. This will increase the beam diameter before the objective and should result in a smaller focus. The measurements performed do not support this (see appendix B.1). The spot size does not get smaller, probably due to more clipping of the beam. The fitted waist was approximately the same size 1.34 µm and the addressing range is reduced by ∼ 75 % to 229.3 µm. This reduction in addressing range combined with no gain renders this lens system not appropriate for the targeted specification.

4.4. Mode of operation

In this chapter I present the addressing capabilities and how the beam of the cAOD can be controlled. First the usable addressing range and the beam quality over the bandwidth is measured. In the second and third subsection different operation modes of the device are presented.

4.4.1. Addressing range

The addressing range is mainly given from the RF bandwidth of the cAOD. The beams which are deflected off axis will experience more aberrations from the addressing telescope and the spot size and shape will be worse. From the simulations in chapter 3.2 we expect that the whole bandwidth will produce a waist smaller than 1.3 µm which makes individual addressing feasible over the range of 323 µm.

The measurement for the addressing range was performed with the setup described in chapter 4.1.2. Because the field of view of the 50x objective is limited to a third of the bandwidth the measurements were performed with both objectives and are in good agreement.

In figure 4.10 the resulting position in both the horizontal and vertical axis are plotted. The positions were extracted from a 2D gaussian fit to the obtained camera images. Note the horizontal direction is just the direction parallel to the ccd chip. The cAOD was aligned onto this axis with the goniometer stage.

The effective obtained addressing range of 302.9 µm is in agreement with the simulation (table 3.1). From the addressing range we can compute the conversion factor η of RF frequency and addressing position. We find $\eta_x = 7.98\,\mu\text{m}/\text{MHz}$.

In figure 4.10b we see a small y-deflection towards the end of the addressing range. We would expect this to be a perfect line. This error can be explained with a small offset in the hight of the objective. According to the Zemax model a vertical shift of 150 µm would produce this shift. Such small deflections in y-direction can reduce the addressing efficiency towards outer ions. With a good alignment this error should be well below the spot size and is negligible.

Further we can look at the beam diameter over the addressing range. This gives an indication if the addressing efficiency du to the spreading of the power will degrade for stronger deflections. In figure 4.11 the fitted beam diameter is plotted. Note that the measurement was performed slightly out of the minimal waist position and the 10x objective is limiting the resolvable spot.

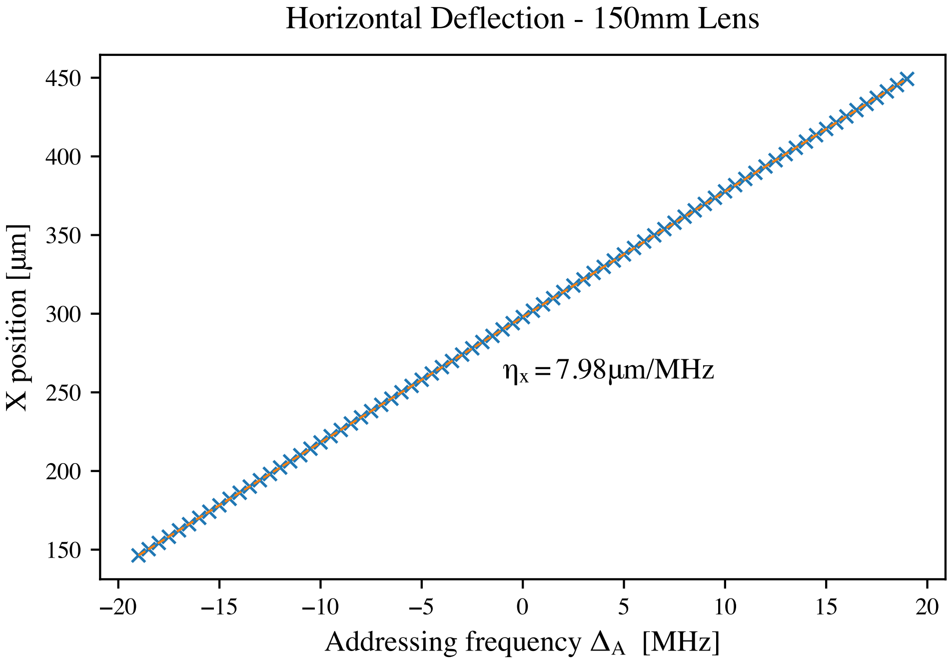

(a) horizontal deflection

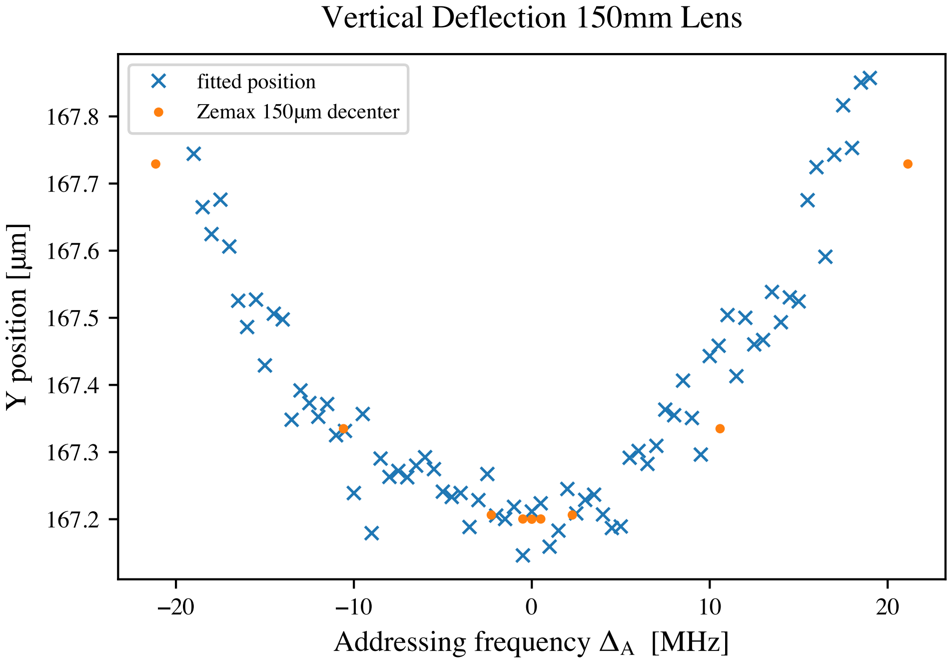

(b) vertical deflection

Figure 4.10.: The addressing range of the cAOD over its full bandwidth of 38 MHz. We see a perfect linear addressing over the total addressing range 302.9 µm in the x-direction. The calibration constant between frequency and deflection distance is $\eta_x = 7.98\,\mathrm{nm/MHz}$. The vertical deflection experience small shifts towards the end of the addressing range (b). A comparison to the Zemax model indicates the alignment of the objective was not perfect which leads to this unwanted deflection. The observed deflection matches the model where the beam enters 150 µm above the center axis.

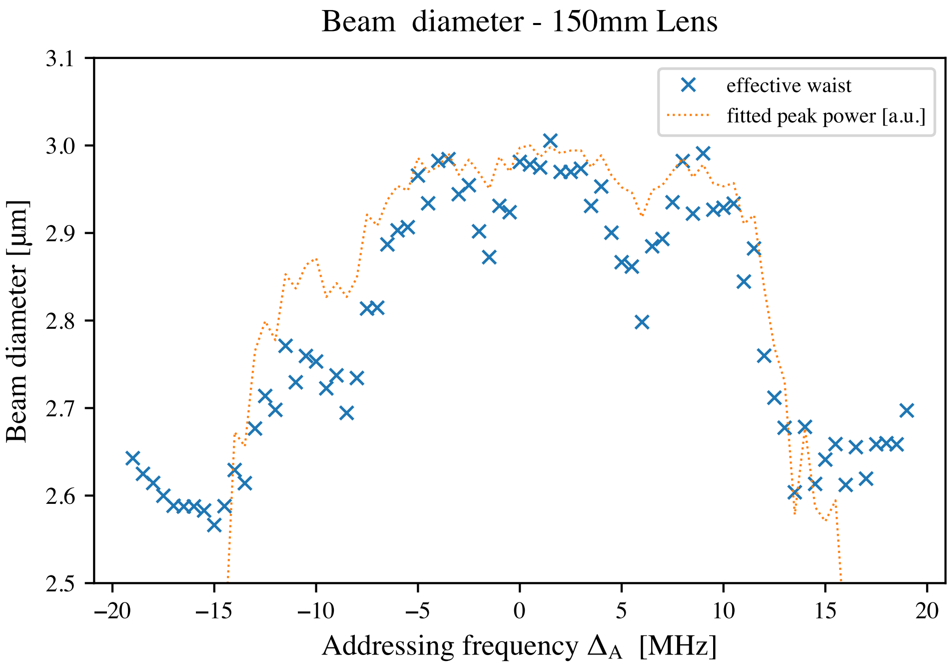

Figure 4.11.: The beam diameter and power over the addressing range. We clearly see the effect of changing diffraction efficiency in the power. The change in the spot diameter looks inverted because the imaging system was not perfectly in focus.

4.4.2. X-Y addressing

For all previous measurements the drive frequency were computed from the given Δ_A by adding and subtracting them according to the scheme presented in chapter 2.5. If we discard the constraint of a constant frequency shift, we can use the two AODs to address an arbitrary point within the span of their bandwidth. Since the cAOD is mounted at an 45° angle it is convenient to define a horizontal and a vertical frequency $\Delta f_{x/y}$. Which are mapped to the AOD frequencies according to chapter 2.5. The images were taken with the 10x objective to image the whole addressing range.

This arbitrary positioning method might be useful to fine adjust the beam position onto the ions and is helpful for alignment. Additionally this lets us test the performance of the optical system further because we can generate multiple points on a square lattice and check if the beams are actually mapped to the correct positions (figure 4.12a).

We see that the systems performs rather constant for addressing frequencies $\Delta_A = \pm 8\,\mathrm{MHz}$ in terms of power and spot size. Towards the end of the addressing range we observe slight deviations in the beam size. The comparison of the four points with the same distance to the center indicates that the addressing beam is not going through the telescope perfectly on the axis but is shifted a bit. Since the roundness of the beam does not deviate a lot this means the input angle through the objective is rather good.

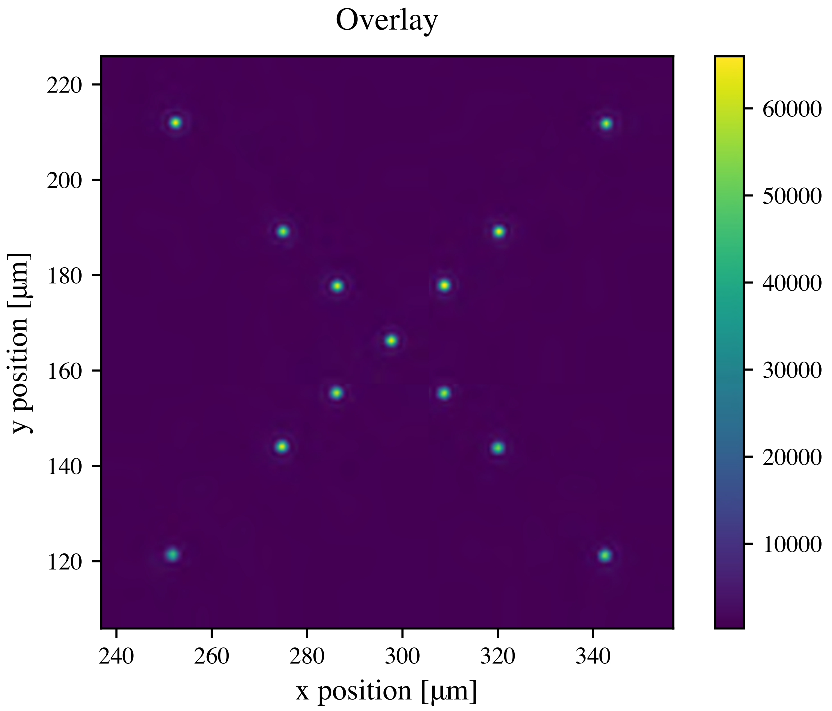

(a) Overlay of mutliple measurements

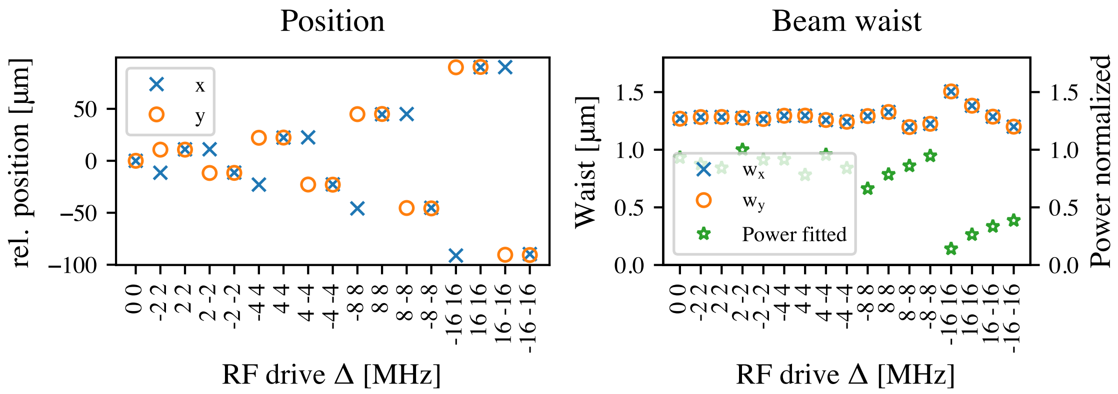

(b) fitted positions

(c) fitted waist and peak power

Figure 4.12.: Each dot represents one measurements with the pair of horizontal and vertical drive frequency. The pictures are summed to compare them. In (a) only the points up to 8 MHz are plotted. We can only see small deviations towards the edges of the bandwidth. (b) The x and y deflection for each point is shown. We see that the position has nearly no distortion also toward the edges. (c) The beam waist will change toward the edges of the band width.

4.4.3. Multi tone

For multi qubit gates or addressing several ions simultaneously more than one addressing spot is generated. This is achieved by driving the cAOD with more than one frequency. This will generate the desired spots but also some unwanted mixings in a grid pattern (see figure 2.4c). From this we see that the power will scale with $1/N^2$ where N is the number of tones (frequencies) which are sent to the cAOD.

For the measurements the setup described in chapter 4.1.2 is used. To generate the multi tone RF signal the arbitrary waveform generator (AWG) mode of the Moku:Pro is used. To generate the wave forms the algortihm is as follows:

1. Set the desired frequencies.
2. Use the invers Fast Fourier transform (iFFT) to go to the time domain.
3. Find the minimum period of the effective signal.
4. Write M cycles of the periods to the Moku.

The number of cycles M was changed because the finite numerical resolution lead to rounding errors which introduced undesired frequency components for some waveform lengths. Additionally higher order components were also prominent in the RF spectrum. To reduce this I added bandpass filters with a window of 87 - 118 MHz, the center of the window is a bit too low and the bandwidth is smaller then needed. But it managed to clean the generated RF signal noticeably. In appendix B.4 some measurements of the generated RF is shown.

The most basic and also important case is to generate two dots. In figure 4.13 we can see the dots with a spacing of 0.628 MHz. This corresponds to two neighboring ions with a spacing of 5 µm.

For implementation of gates it is important that the power of two dots is the same. Additionally also the position accuracy should not be affected of this driving mode. In figure 4.14a two tones were generated and the addressing frequencies $\pm\Delta_A$ were increased. As a reference a single addressing beam at the center is shown.

We can see the power for the tones is lower than the expected 25 %. This can be explained because the RF signal in the AWG mode is attenuated by ~ 1 dB from the band pass filters. Additionally the RF amplitude was held constant between single tone and multi tone operation. The effective RF power at the desired multi tone frequencies is lower than for the single tone. This two effects combined have a result that the diffracted power is lowered due to a weaker drive signal. The decrease in power for higher addressing frequencies Δ_A comes from the decrease in diffraction efficiency for higher frequencies (compare bandwidth measurement). This can be improved by changing the RF amplitude depending on the frequency.

In figure 4.14b the position of the two points is shown. The dashed line indicate the expected deflection from the measured calibration η_x. This is in good agreement over the whole addressing range. This validates that the AWG implementation works well and the device indeed can generate the diffraction for two frequencies independently.

In this application we can see the advantage of the cAOD in the case where two ions are addressed each ion will see ~ 20 % of the available power. If we compare this to a classic fiber array the power is split to eg. 12 channels and then switched with a fiber AOM. Each of the ion will only see 8.3 % of the total available light. In this discussion

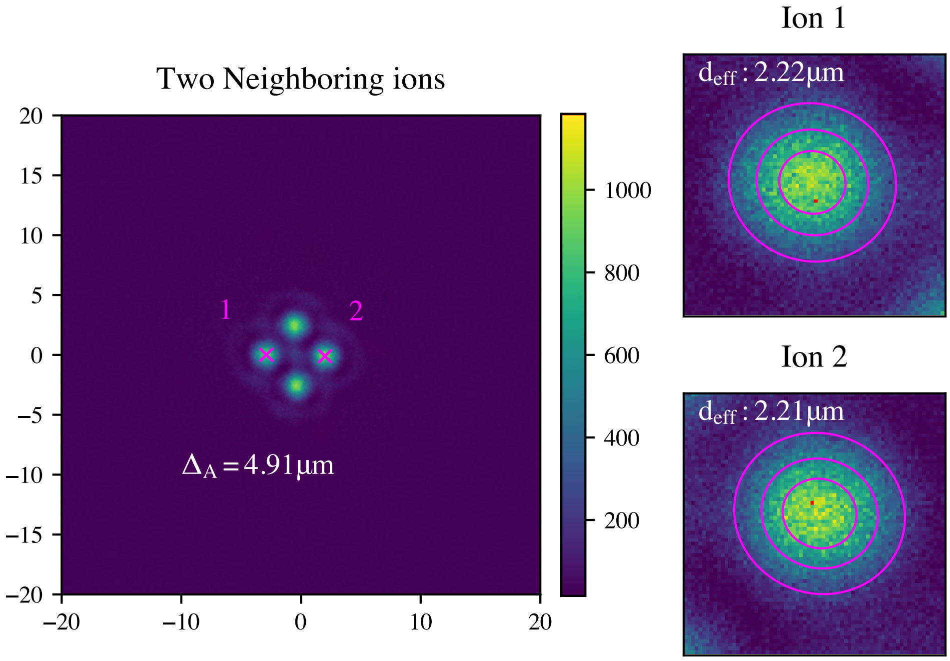

Figure 4.13.: Two neighboring ions are addressed with two frequencies with a difference of 0.628 MHz. The spacing is slightly off since the frequency was based on the theoretical values. With the measured η_x the frequency spacing for two ions is 0.637 MHz. Both addressing dots have a round shape with a similar diameter. Note the two additional dots are the mixed frequencies of the desired drive frequencies and cannot be eliminated. These spot will introduce scatter in the chamber.

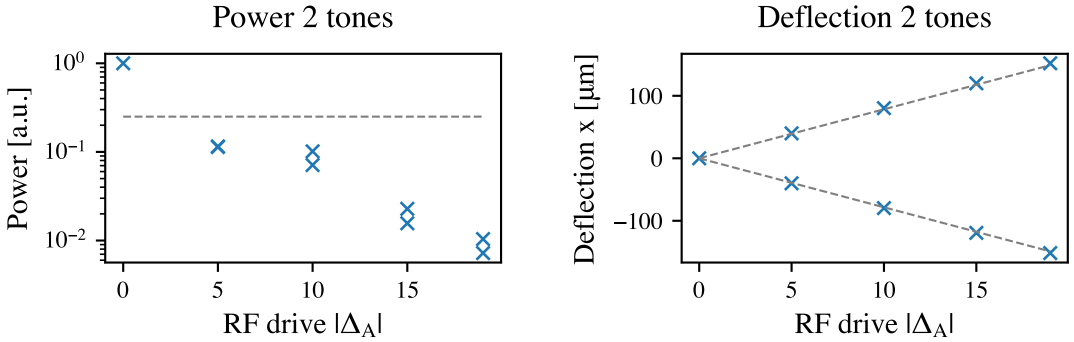

(a) fitted peak power

(b) position of beams

Figure 4.14.: A series of two RF tones with increasing deflection position was sent to the cAOD. (a) The fitted peak power is below the expected 25 % due to losses in the RF signal generation. Additionally the deflection power will decrease for higher frequencies. (b) The position of the beams is accurate and no shifts are introduced from the second RF frequency

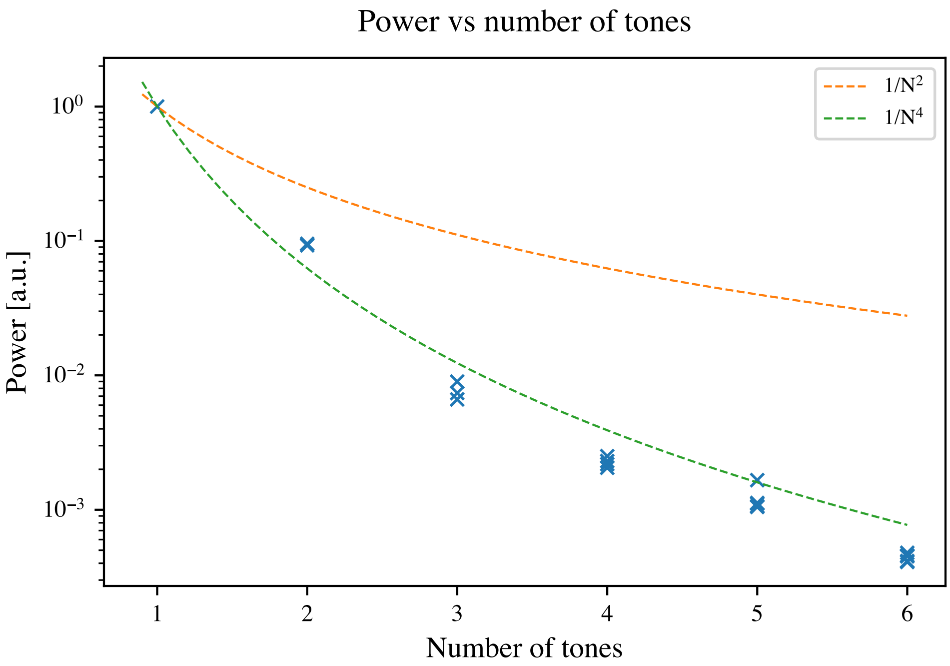

Figure 4.15.: The number of RF tones is increased and the power in the generated addressing beams is measured with the camera. We would expect a scaling with $1/N^2$. The data is better represented with an $1/N^4$ dependancy beacause the RF amplitude of the AWG is held constant.

the efficiency of the cAOD and fiber AOD were neglected but this is in both cases around 80 %.

The scaling of the power in the usable node should be $1/N^2$. To test this I generated an increasing number of tones from 1 to 6 and fitted the power for each beam on the addressing axis. All measured points are plotted in figure 4.15, some of the measurements overlap and are not distinguishable in the diagram. We find a strong discrepancy to the expected scaling and the data is better represented with a scaling of $1/N^4$. The ideal scaling assumes the RF power for the N^2 beams is equal to the power for one addressing beam. This assumption does not hold because the RF signal is generated with a constant amplitude. This means that the amplitude for each peak scales with $\sim 1/N$ and thus the RF power is quadratic in the amplitude. In total this results in the $1/N^4$ scaling we observe.

To further test the limits of the system I created waveforms with 33 (figure 4.16a) and 60 (figure 4.16b) tones. In ordert to take these images the ND filters and exposure times were adjusted. The optical power is weak because of the $1/N^2$ scaling and the lower RF power. But we see the cAOD is capable of generating 60 beams which can be clearly resolved. One can note the lower dots with higher frequency components are weaker than the top ones. Purely from the efficiency curve of the device the decrease towards the end of the RF bandwidth should be symmetrical. This additional drop in efficiency is due to the bandpass filters which have a center frequency at 102.5 MHz(compared to the cAOD center frequency of 110 MHz).

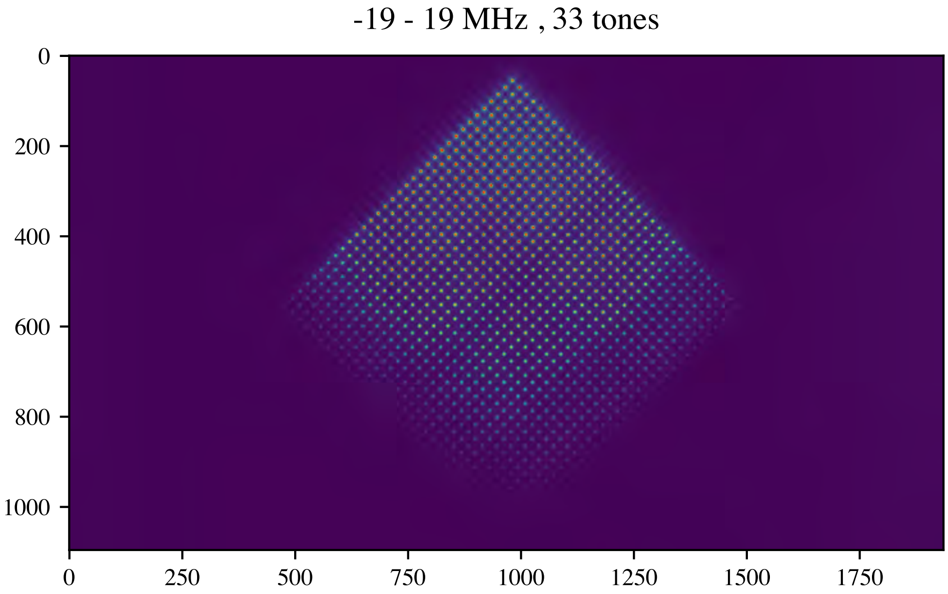

(a) 33 equally spaced tones

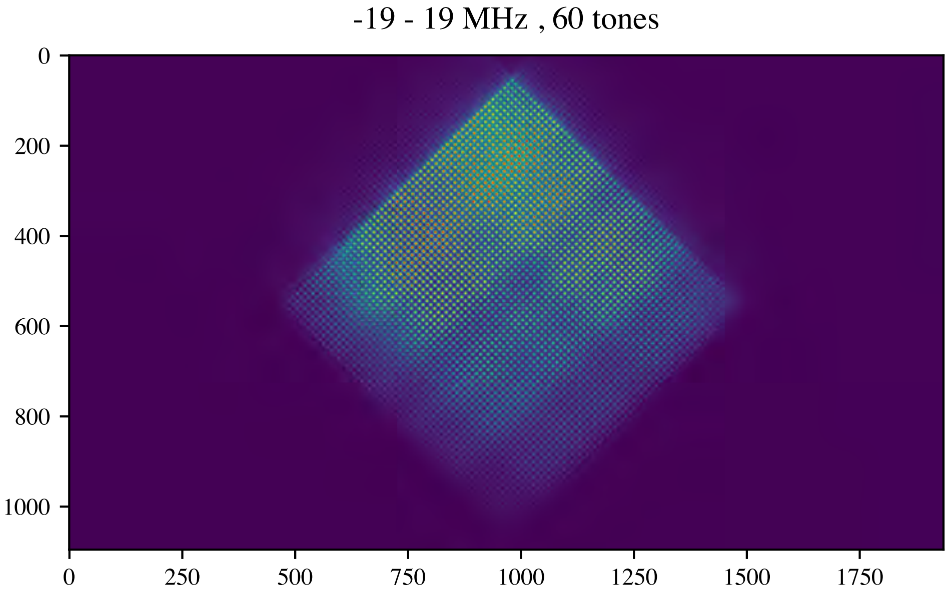

(b) 60 equally spaced tones

Figure 4.16.: Multi tone operation of the cAOD. The optical power is strongly reduced by a factor of $\sim 10 \times 10^6$ (estimated from the used ND filters). This lower points in the image have higher frequency components and are stronger attenuated by the bandpass filter which has a lower center frequency than the cAOD. This lower RF power makes the dots fainter.

5. Experimental Setup

5.1. RT Setup

The room temperature (RT) setup is built around a monolithic Paul trap which is operated at room temperature. The trap is placed in an ultra high vacuum (UHV) chamber on a support pillar with an Ca oven. The setup uses the $^{40}\mathrm{Ca}^{+}$ isotope. To define the magnetic quantization axis a constant magnetic field with 4 Gauss is applied along the trapping axis. The chamber and all the beam shaping optics are placed on a vibration isolated optical table. To minimize environmental impact from temperature and humidity and to keep dust away the setup is below a flow box[1].

To operate the setup a multitude of different laser beams are used to control the ions. The light beams are switched and modulated mostly with AOMs. All devices are controlled from the in house developed control system M-ACTION. The experiments are controlled from an ETH version of the NIST-developed software package *ionizer*.

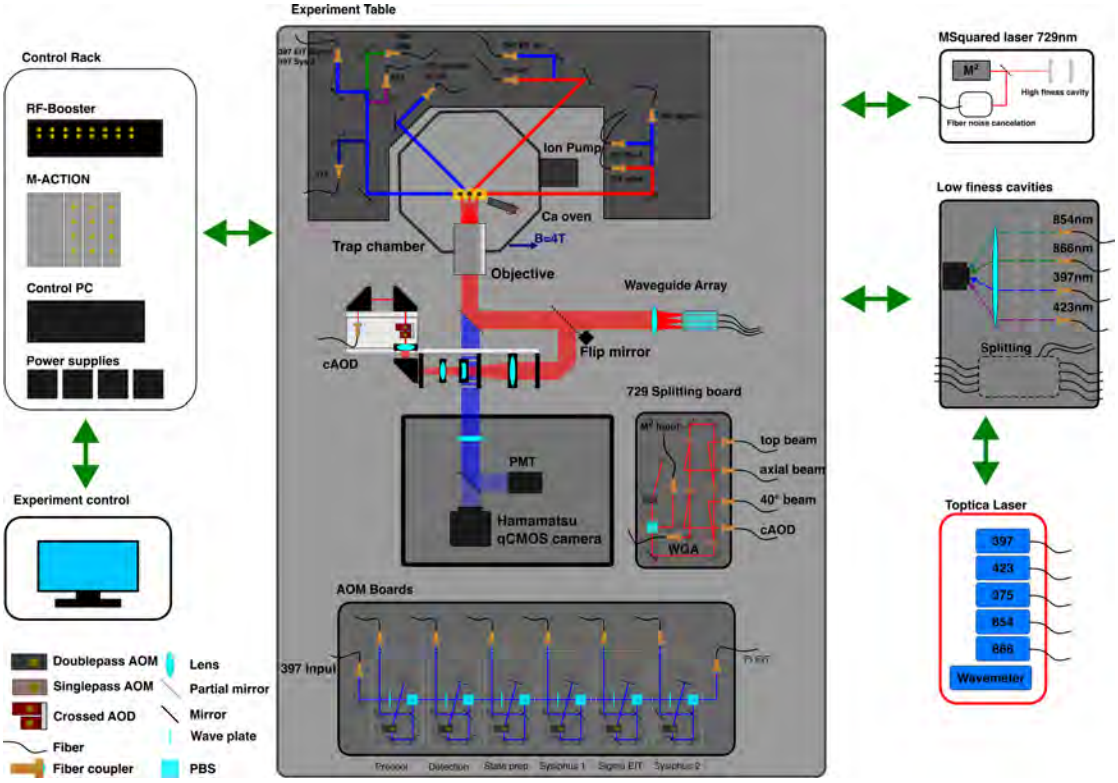

Figure 5.1.: Overview of the room temperature setup. The 729 nm splitting board and the cAOD setup were added in the course of this thesis. The individual components are simplified and some parts were left out.

---

[1] Outlet of the air conditioning system with high laminar flow.

Trap The trap is fabricated from a single piece of glass using femtosecond lasers to alter the material properties. The exposed parts can then be etched away. The trap is engineered to store up to 50 ions at equidistance. The entire structure is gold coated. Special engineered tranches are used to keep the different electrodes isolated. The trap is driven at an RF frequency of 35 MHz. The trap is segmented along the trapping axis. This allows to fine tune the ion spacing which is needed for the addressing with a WGA.

Laser sources For a high fidelity qubit manipulation the lasers need narrow line widths and good phase stability. This is extremely important for the 729 nm qubit laser. A Ti:Sa laser from MSquared is used in combination with an high-finesse cavity to generate high power of the qubit manipulation light.

The other wavelengths describe below are generated with Toptica diode lasers. These are stabilized with four low-finesse cavities tuned to the desired frequencies of 397, 423, 854 and 866 nm. For stabilization an PDH-lock is employed.

The second stage of the ionization with the 375 nm light does not need to be very precise and is used directly from a Toptica diode laser.

Loading The hot Ca atoms fly out of the oven toward the trap. A frequency tunable 423 nm beam is used to select the desired isotope. Using an additional 375 nm beam the atoms are then ionized (see figure 1.1b). The pulses for ionization do not need to be fast and can be switched with mechanical shutters.

Puls generation The majority of the power from the diode lasers and MSquard are directly delivered to the RT table with fibers. The 866 and 854 nm beams are used for re-pumping and qubit reset. It's sufficient to switch these pulses fast since the frequency is already adjusted with the cavities. This is achieved with a fiber AOM for the two fibers.

The light from the 397 nm fiber is distributed to six DP AOM boards using waveplates and PBSs such that the power can be adjusted according to the needs. Each Board allows to switch the pulses and also shift the frequencies. The DP AOM operate int the range of 110 MHz to 215 MHz. The following beams are generated and delivered in fibers to the chamber:

- Precool beam
- Detection and Doppler cooling beam
- State preparation
- Sisyphus cooling (Sys 1 and Sys 2)
- EIT-cooling beams (EIT pi and EIT sigma)

Qubit manipulation The ions are manipulated using the gate implementations presented in chapter 2.3.1. The light can be delivered to the ions through different optical axes. The switching is done with the splitting board setup presented below. The setup features three global beams: axial along the trap axis, in plane at a 40° angle with respect to the trapping axis and from the top. In addition two options for single ion addressing are possible under a 90° angle. With a flip mirror one can select either the newly implemented cAOD setup or the WGA.

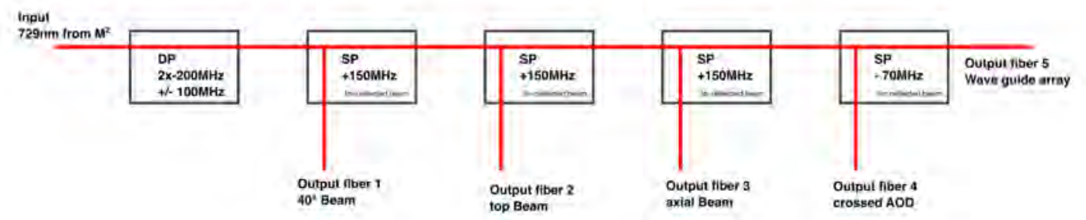

Figure 5.2.: Schematic of the splitting board. The light can be directed to one of the five outputs. With exception of the last output an additional frequency shift from the switching is introduced.

Imaging For ion readout a high NA objective made by Photon gear is used to collect the light of the ions (NA $= 0.4$). The collimated beam passes through the dichroic mirror which is used for the individual addressing setups and is focused with a $f = 500\,\mathrm{mm}$ lens. A bandpass filter is used to maximize contrast. Using a pellicle beam splitter the beam is split between the photo multiplier tube (PMT) and a CCD camera. Because of its single pixel nature the PMT cannot detect which ion is in the $|1\rangle$ state. The Hamamatsu qCMOS camera allows for ultra low noise measurements of all ion states in the trap with site-resolving capabilities.

5.1.1. Splitting board

In the previous chapter we have seen that the qubit manipulation is done from multiple directions. In addition to the global beams a WGA is used for single addressing and also the cAOD setup uses the light from the MSquared. Due to the high power an endcaped fiber is used. In total five different endpoints should be used. Previously fiber splitters[2] were used to divide the light and fiber AOMs were used to switch the light. In this configuration the majority of the power is dumped in the unused channels, only $\sim 10\,\%$ is delivered to the ion[2].

Therefore we built a new 729 nm distribution board. Instead of fiber splitters the board uses AOMs to deflect the beam. This method allows to steer the majority of the power($\sim 50\,\%$ of the MSquared input) to one output. The introduced frequency shift of the AOMs is pre-compensated with a DP AOM (figure 5.2). The splitting board is built in a compact and sturdy way.

A Double pass frequency shifter is used to select different transitions of the Ca^+ ions. It can introduce a variable frequency down shift from 200 - 400 MHz with almost no displacement of the beam. This is achieved by placing a cat-eye lens into the reflector arm [30]. In order to separate the incoming and outgoing beam a $\lambda/4$ waveplate is placed before the back reflector. The back reflector will change the handedness of the

---

[2] Assuming 60 % efficiency in the DP AOM, 20 % usable light in the fiber splitter and 80 % from fiber AOM

circular wave and the second pass through the waveplate results in an 90° rotation of the polarization. The actual separation is then done with an PBS after the second pass though the AOM.

In addition to the frequency control the DP AOM is used to switch and shape the light pulses on timescales of µs. To enable fast rise and falling times the beam is focused into the AOM crystal. This enables fast rise times on the order of 25 ns.

The switching AOMs are either on or off and steer the diffraction order away from the 0th order. The resulting frequency up shift of the RF drive is pre compensated in the DP AOM. The switched beam is separated with mirrors. In figure 5.2 an overview of the output channels is presented. Outputs 1 to 3 are used for the different global manipulation beams.

The output 4 is used for the cAOD setup and utilizes a different AOM. The device is aligned for the -1 diffraction order unlike the oder channels. This additional shift of $-70\,\mathrm{MHz}$ compensates the static frequency shift of $2\Omega_0$ from the down stream cAOD. Only this combination of switching and frequency compensation enables us to use the +1 +1 cAOD without any losses in power from additional frequency shifters.

Note that output 5 has no frequency shift. This is used for the fiber array which has additional fiber AOMs for each channel which will introduce the same shift downstream.

5.1.2. Addressing system mount for experiment

The cAOD assembly with the telescope is big and heavy. To mount this subsystem to the chamber has some additional constraints given from the overall design and layout of the chamber and the already present imaging and addressing optics. It is planed to enclose the chamber and the surrounding optics in a mu-metal shield. The telescope was designed with the constraints in mind whereas the cAOD stage was not specifically tailored to the RT setup. In addition to the telescope and cAOD the input optics and the flip mirror also needs to be mounted to the setup. With this starting point the assembly in figure 5.3a was designed in CAD. In figure 5.4 the assembled mount can be seen.

As a base for the optical system the Zemax simulation was imported into the CAD together with the model of the current RT setup this fixed the position of all optical components. Not all existing optical components are perfectly represented in the CAD model. I included some adjustment options to account for small deviation throughout the design. The alignment of the setup is difficult when it is mounted to the experiment. Therefore it would be ideal if the assembly can be aligned on the test setup and then be moved to the experiment. This resulted in the following design requirements:

- Fix relative alignment of input optics to cAOD
- Fix relative alignment of telescope to cAOD
- Make input optics and telescope removable
- Incorporate adjustment in mount of flip mirror

From these requirements I designed a solid baseplate which acts as the reference point for the cAOD stage, the input optics and the telescope. Two precision dowel pins make the XY-positioning between the reference plate and the adapter plates for the optics.

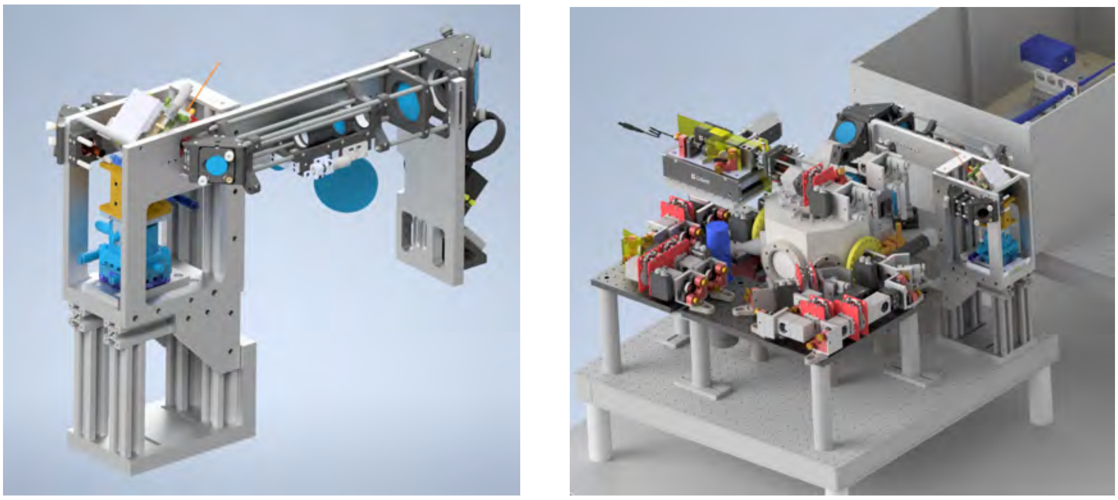

(a) isolated assembly (b) full setup

Figure 5.3.: CAD rendering of the addressing system assembly. The blue circles are the optical elements exported from the Zemax simulation. The design uses a combination of aluminum profiles with custom machined plates as a support structure. The optics are mounted in a Thorlabs cage system which is mounted to the aluminum plates.

The tolerances are chosen for a clearance fit to enable taking the plats apart. To give more stability to the assembly an aluminum profile is used, which takes the load of the whole assembly. The profiles are aligned with small alignment combs to get better angular accuracy.

The telescope system and the input optics are nearly identical to the one presented in chapter 3.4. The telescope and the input optics were slightly modified in size to adapt for better mounting. Also the cAOD stage assembly is the same as for the test setup.

The long telescope arm is supported with an additional custom machined post. This part provides support to take the load of the long leaver arm and acts as a mounting surface for the flip mirror. The flip mirror has only one screw for mounting. To reduce possible rotations due to vibrations an edge was added which is flush with the housing of the device.

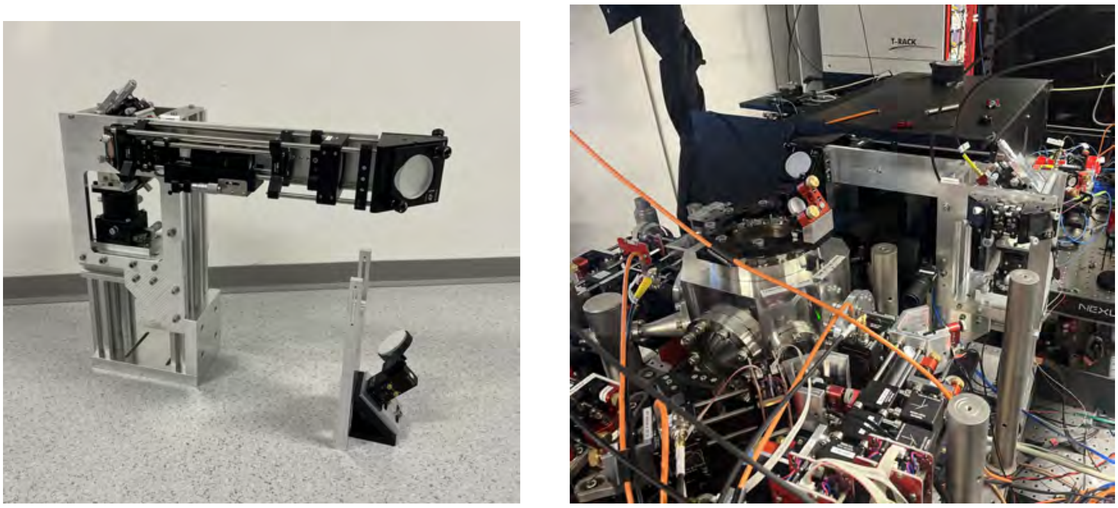

(a) isolated assembly

(b) full setup

Figure 5.4.: (a) The mount for the cAOD and telescope during assembly. On the left the AOD with the six-axis stage is mounted. On the right the periscope with the flip mirror is placed. These two parts are connected in the final configuration. (b) The assembly mounted to the chamber. Note the other side is visible. All components (input optics, telescope and cAOD) are aligned with dowel pins.

5.2. Measurement with Ions

The addressing system presented in chapter 5.1.2 was placed on the experimental table. The alignment of the system was prepared on the test setup[3] according to the procedure described in chapter 4.1.2. A polarization maintaining fiber is used to bring the 729 nm light from the splitting board to the cAOD addressing setup. The switching AOM on the splitting board cancels the static frequency offset of 220 MHz in combination with the double pass.

The RF signals are generated from the M-ACTION control system to integrate the addressing capabilities into ionizer. The code base for the experiments was adapted from the GKP setup[4]. To implement the operation mode of our cAOD according to chapter 2.5 we had to change the signs in the equations relating the deflection position with the AOD frequency.

Constraints The alignment of the cAOD addressing system onto the ion through the imaging objective is an challenging task because the alignment needs to be perfect within several µm. The constraints given from the working setup further complicate this:

- No camera can be placed in the focal plane of the objective due to the vacuum chamber.
- The objective has to focus on the ion axis and the ion should sit in the center.
- The objective angle needs to be orthogonal to the ion chain and the view port.

---

[3] The stability of the dowel pins is estimated in appendix B.3.

[4] Experiment at ETH Zürich which uses the exact same trap and a very similar experimental setup.

- The ions need to be imaged with the camera and PMT for readout.
- The WGA needs to work in the same configuration of dichroic and objective.

The imaging system is used for all experiments and works reliably. Also the WGA is already used for experiments but the alignment is not fully optimized. The imaging part can also work with bigger aberrations and therefore it is not given that the objective is in its optimal position. Based on this starting point we decided to use the cAOD to find the optimal alignment of the objective and ignore the WGA for now. The cAOD is much better for this task because it can scan a region of 210 µm width and height (square which fits in the span of the cAOD). This makes it much easier to find the ion signal and optimize for it.

We decided to adjust the dichroic mirror and the objective to optimize the alignment. The camera we wanted to keep fixed. Except for the ion no component can be used as a fixed reference because they can work in suboptimal regimes as well. All positions have to be optimized in parallel since the measurements can only be performed if there is some light entering the PMT. After several failed attempts to align the objective and the cAOD we also started moving the camera. With this additional degree of freedom we started converging towards a beam with fewer aberrations and a smaller focus.

Abberations The observed aberration can have many potential origins. All optical components between the input fiber and the ion could contribute. In the process of the alignment we could eliminate the cAOD and all optics before. The aberrations observed in figure 5.5b rotate when the cAOD is rotated. Because the scan frame rotates together with the AODs this means the aberrations must occur after the deflector. Otherwise they would rotate along and stay in the same spot on the scan field.

The telescope after the cAOD is a potential source for aberrations. The alignment was optimized in several iterations. For the big output beam with a diameter of ~20 mm it is also important that the gaussian maximum is aligned with the center of the beam. The overlap was tested by propagating the beam several meters. The spot did not experience noticeable distortions in the far field and the gaussian is well centered. This check also showed that the beam is well collimated.

The next optic after the telescope is the dichroic mirror. By removing it temporarily we noticed that the mirror was slightly bent and focussed the beam in the vertical direction slightly. This was resolved by gluing the mirror to the holder instead of clamping it.

This leaves only the objective and the vacuum viewport as source for the aberrations. The view port and trap are fixed in position so the objective alignment has to be optimized with the 5-axis stage.

Alignment The current alignment procedure is as follows:

1. Use the objective to image the ion onto the camera without an imaging lens.
2. Insert the imaging lens and keep the ion image at the same position on the camera.
3. Align the addressing beam onto the objective.
4. Scan the height of the addressing beam by hand and move the beam until it is clipped on the trap electrodes. Move to the middle position.

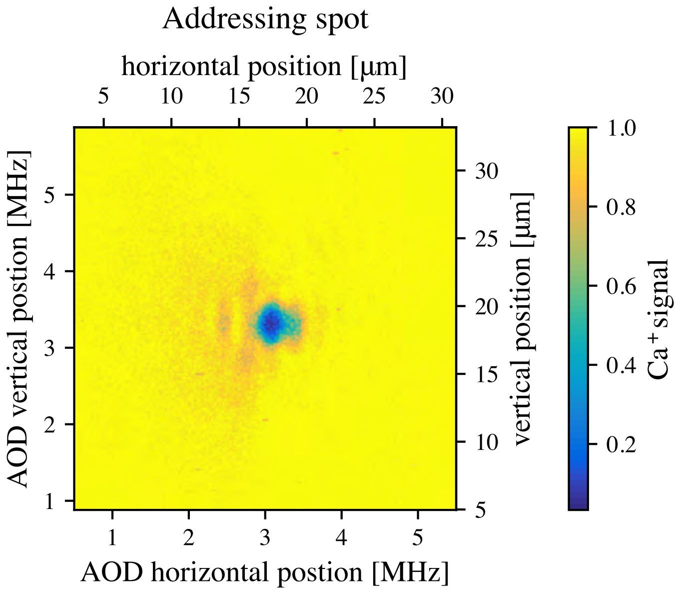

(a) optimized spot

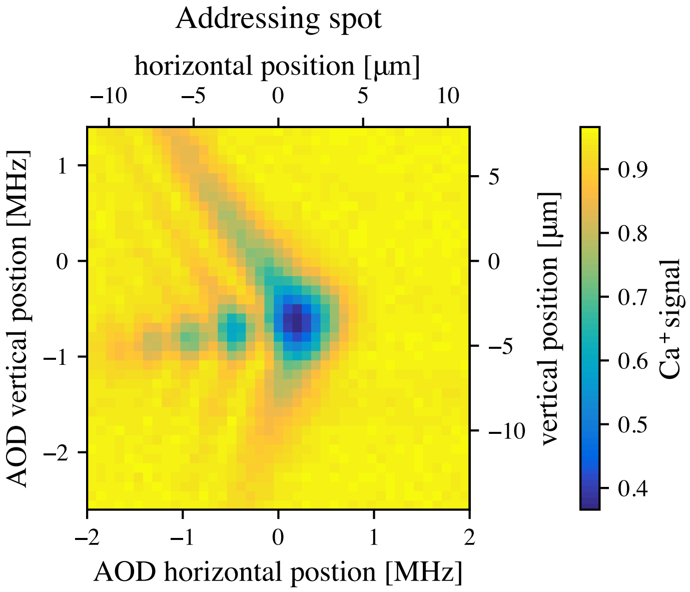

(b) spot with aberrations during alignment

Figure 5.5.: Map of the ion state after a π-pulse with length of 2.8 µs and a power of ~10 mW. We look only at a small subset of the total addressing range. The ion is kept at a fixed position and the addressing beam is moved. The color bar indicates the ion state. The ion dark state ($D_{5/2}$) is blue and the bright state ($S_{1/2}$) is yellow. In (a) a decently optimized beam is depicted. The beam is still distorted from aberrations which need additional optimization. (b) shows the spot during alignment with strong aberrations. The pattern indicates coma from a tilted lens.

5. Find the horizontal alignment by scanning the cAOD and moving the beam by eye to the trap center.
6. Once the ion signal is found it can be moved to the scan center by tilting the dichroic mirror.
7. Optimize the focus such that the beam is slightly not focused. This allows to see the aberrations better.
8. Translate and rotate the objective to reduce the aberrations on the addressing spot. Adjust the camera and PMT to keep a strong signal.
9. Optimize the beam pointing of the addressing beam on the objective axis with a back reflector and irises.
10. Repeat the last two steps.

The beam pointing of the addressing beam and objective can be checked with a plane mirror that screws to the objective mount. If the reflected beam overlaps with the incoming beam the axis of the beam and objective are aligned. This might also be used to validate the final alignment. A small part of the reflected beam will pass through the dichroic and enter the imaging system. This part is usually blocked with a 397 nm optical bandpass filter. If the filter is removed the signal of the ion and the addressing beam should overlap.

Experimental control The scan shown in figure 5.5 measures the state of the ion after an π-pulse is applied. The state is detected from the PMT signal with a threshold value to separate the bright $S_{1/2}$ and dark state $D_{5/2}$. Each measurement is the average of 10 shots. Multiple passes of a scan are then averaged. Before the π-pulse and the readout the ion is cooled and brought to its atomic ground state. The pulse sequence for this experiment is shown in figure 5.6 .

The applied π-pulse needs to be calibrated for the scan to have a good contrast. The calibration is done by performing Rabi flops. The shortest pulse length which can be generated is limited by the control system to $\sim 1.5\,\mu\mathrm{s}$. Therefore the power sent through the cAOD is reduced by lowering the RF amplitude of the single pass switching AOM. This translates to an approximate optical power of 10 mW.

To map the addressing beam it is important that the ion is not moving in the trap. The ion can move on different scales, the micro motion induced from the RF trap and the inherent motional state of the ion. The micro-motion can be compensated by placing the ion perfectly on the RF null. The ion position is shifted with the direct current (DC) shim-electrodes. The optimal offset voltage is found by modulating the trap RF frequency with the motional sideband of the ion.

The motional state of the ion is reduced by doppler cooling. Further sideband or Sisyphus cooling would be needed to bring the ions to the motional ground state.

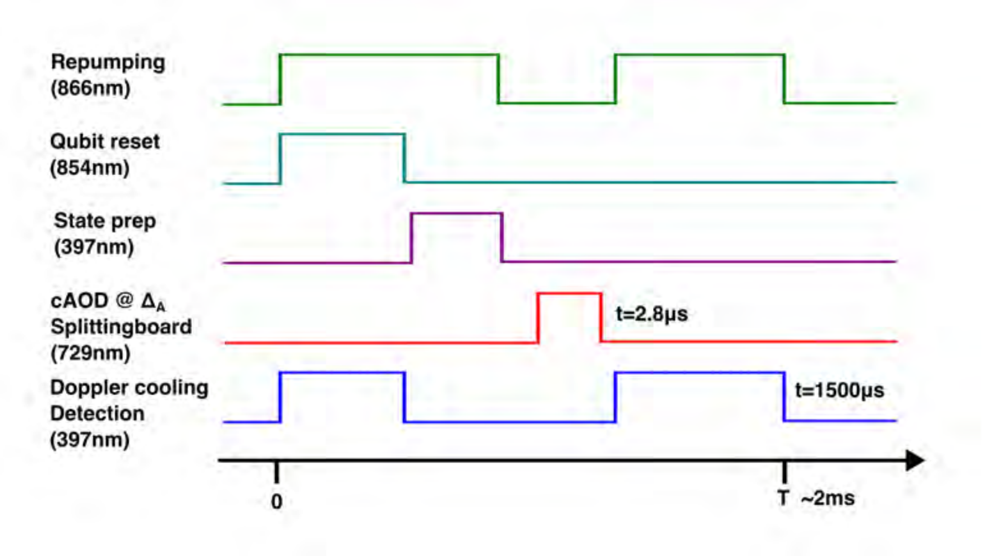

Figure 5.6.: Pulse sequence used to map the addressing beam. The pulses are sent to the AOMs in the optical paths and modulate the light accordingly.

5.2.1. Spot shape and crosstalk

The preliminary optimized spot presented in figure 5.5a is used as a basis to estimate the beam waist and the crosstalk. The spot experiences still some aberrations and the focus position might be further optimized. We can determine the spot size by fitting a 2D Gaussian peak. The conversion to µm is done with the calibration constant η_x found in the test setup. The conversion factor needs to be scaled down by the factor of $\sqrt{2}$ because we work in the horizontal coordinate system and not directly with the bare AOD frequencies (compare figure 2.4b).

This gives a spot size of 3.57 µm. The fit measures the $1/e^2$ diameter of the peak (figure 5.7). We can see that this already enables individual addressing (figure 5.7a). The objective can be moved in 10 µm steps, a finer adjustment of the focal plane can be achieved with telescope lens. To determine the spot size it would be better to keep the addressing system fixed and move the ion along the axis. In this operation effects from the addressing system are not measured. The ions can be shifted with the DC electrodes of the trap.

If we look at the intensity crosstalk in the horizontal direction we see that the aberration present to the left introduce a lot of crosstalk. The right side of the peak is already very steep and experience nearly no crosstalk. With the current aberrations the worse crosstalk to the neighboring ion on the left side is in the order of 2×10^{-2}.

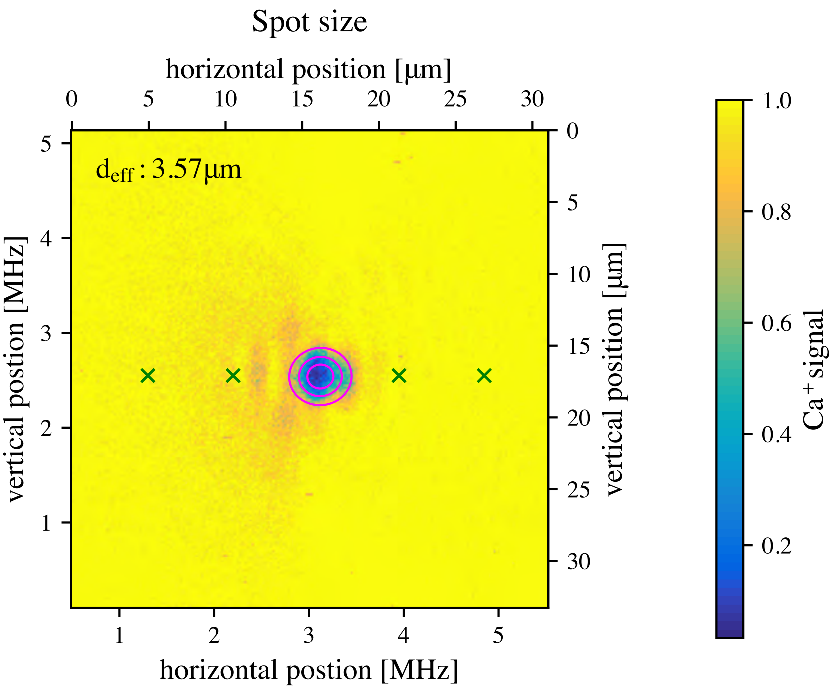

(a) gaussian fit

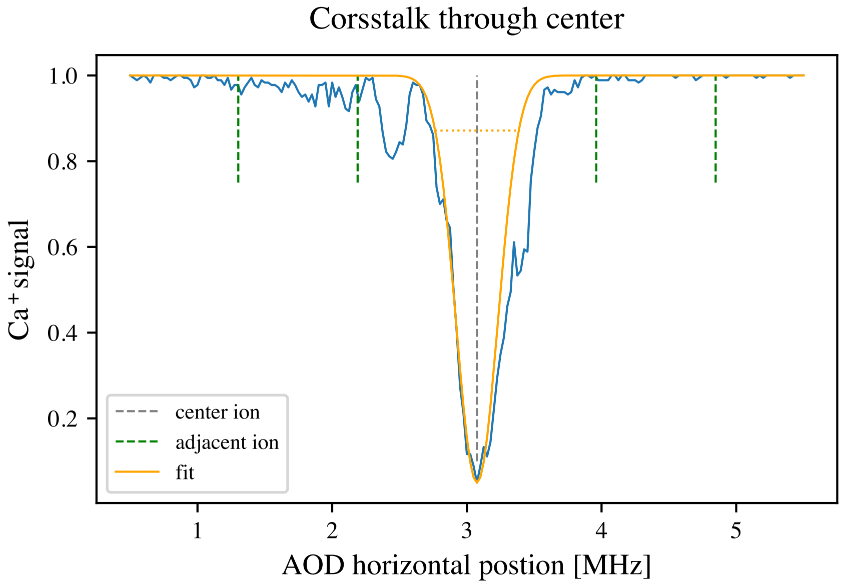

(b) crosstalk through center

Figure 5.7.: A first estimate of the crosstalk between ion in the setup. (a) A gaussian fit of the spot results in an estimated beam diameter($1/e^2$) of 3.57 µm. Since the beam is deflected the shape might be distorted from the cAOD. The four crosses indicate the position of the two nearest neighbors in either direction. (b) A cross section through the spot along the addressing axis shows the intensity crosstalk in the current configuration is in the order of 2×10^{-2}. The right hand side in (b) shows with better alignment the expected lower crosstalk should be feasible.

6. Addressing with fiber v-groove array

A possible further step of the addressing setup could be to use an cAOD in combination with an FVGA and a WGA. The FVGA is used to couple the light from the cAOD into the fiber of the WGA. The WGA is used as a mode cleaner and the cAOD enables good multi ion addressing capabilities. In addition less scattering light will enter the chamber because the unwanted diffraction orders are blocked at the FVGA. A FVGA is a piece of glass substrate which has high precision v-shaped groves in it. In the grooves fiber cores are placed and glued. For this test an available 8 channel FVGA[1] with an pitch of 127 µm is used.

6.1. Test setup

This test aims to demonstrate the feasibility of such a setup. The light delivery and the cAOD mount are identical to the setup described in chapter 4.1.1. The output of the cAOD is expanded in an 1:2 telescope and coupled into the fibers with a 35 mm planoconvex lens. This lens system is aligned analogous to the procedure explained in chapter 4.1.2.

The FVGA is mounted on a simple XYZ-translation stage[2]. The angle for the coupling is adjusted with two mirrors between the telescope and the coupling lens. The alignment of the cAOD is rather sensitive. A 2 degrees rotation stage would be advantageous for alignment but was not available. For the alignment the fiber pen[3] is connected to the neighboring fiber. The light of the cAOD and from the fiber pen is moved to the center of the in-coupling lens. If both the 729 nm and the fiber pen beam are perfectly overlapping the coupling is optimized with a power meter.

For the first test the fibers were checked one at a time with the power meter. To have faster measurements for multi tone and individual addressing tests the fiber ends were put on a 3D printed v-groove mount. To image the fiber ends a simple imaging system consisting of a $f = 60\,\mathrm{mm}$ and $f = 75\,\mathrm{mm}$ lens was used. To maximize the light collection 2 inch optics were used. Then the ccd camera[4] was used to image all 8 fiber channels at the same time. The power to the camera was reduced with a combination of two ND filter (ND30 and ND20).

6.2. Measurements

The first measurement aims to find the positions of the fibers in terms of the cAOD addressing frequency. The beam is moved along the FVGA and if a fiber core is hit light will be coupled into the fiber. For this calibration a single tone is generated using the

---

[1] OZ Optics,VGA-8-127-0-X-14.4-4.0-2.0 3-QS-730/860-4/125-2.5U-1-1-0.6-SP

[2] 3x OptoSigma, TAM-401S

[3] A light source which couples directly into a fiber. This is helpful for aligning of fiber couplings.

[4] Thorlabs, Kiralux CS235MU

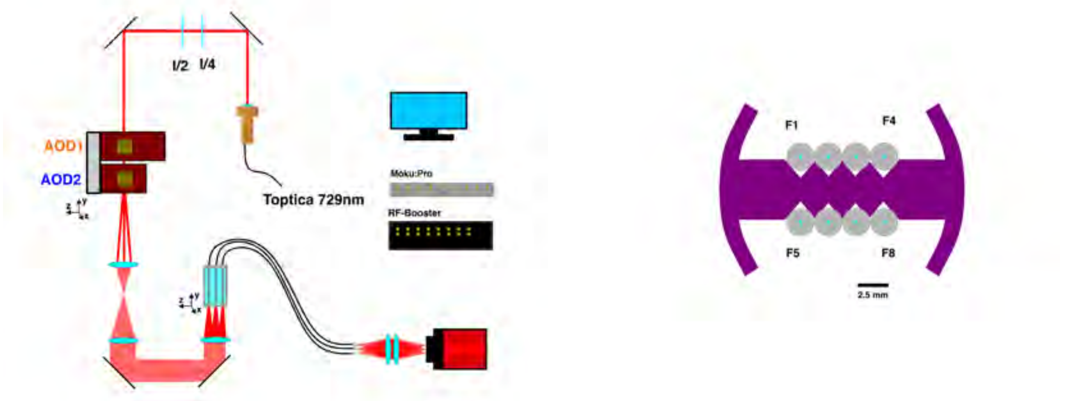

(b) fiber holder

(a) setup

Figure 6.1.: Setup for testing the in-coupling to the FVGA. (a) An overview of the optical system with the imaging camera is depicted. The fiber ends of the FVGA are imaged with a camera. The telescope and in-coupling lens are placed in a Thorlabs cage system. (b) A detailed view of the 3D printed fiber holder. The holder can be mounted in an 1 inch optics mount. All fibers are aligned with a stop in the front and clamped from the top with a spring loaded part.

cAOD and the addressing frequency Δ_A is scanned over the bandwidth. Using the CCD camera the maximal intensity is measured (figure 6.2).

We can see the eight fibers are clearly distinct peaks. For single addressing tones there is no light arriving at the position of neighboring fibers. This means the crosstalk is very low. The peak hight is not a good measure for the actual optical power in the fibers because the imaging system is not ideal for this measurement. With the available 2 inch lenses a magnification of 0.8 was the only viable option. The core is therefore only a single pixel on the ccd sensor. Additionally the system introduces a lot of aberrations for the outer fibers. This measurement is more of qualitative nature to observe where light is coupled into the fibers. For the particular set of telescope and in-coupling lens an addressing constant $\Delta_F = 4.59\,\text{MHz}$ between the fibers is measured.

In figure 6.3a the powers in each fiber is measured with the power meter. The alignment of the setup was before optimized to have equal coupling into fiber 1 and 8. The optical power before the FVGA is 2.55 mW which results in a weak coupling of 1.5 %.

If the alignment is optimized for only one fiber the coupling can be increased. In fiber 4 (driving the cAOD at the center with 110 MHz) a coupling of 1.05 mW is achieved. The cAOD is moved to the first fiber by changing the RF drive to 124 MHz and the coupling is optimized again. The measured in-coupling was 0.65 mW. This shows that the coupling also works for deflected beams.

During the optimization I figured that the FVGA is not perfectly orthogonal to the optical axis of the in-coupling lens. The current setup with only a XYZ-translation stage does not allow to correct such an angle.

To get a sense of crosstalk between two neighboring channels is difficult. With the power meter I am below the sensitivity. And the camera has no quantitative value. For

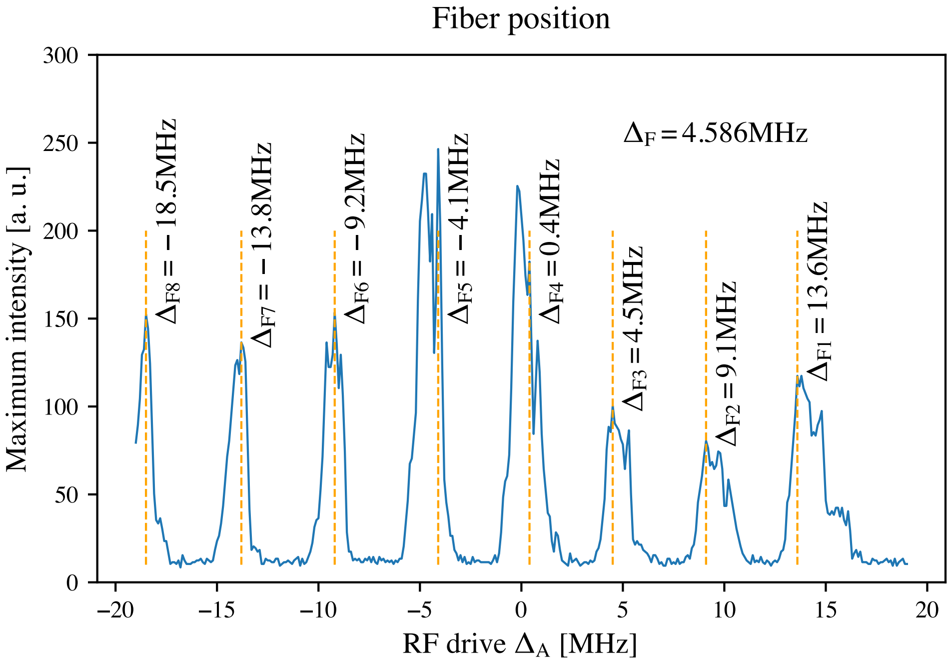

Figure 6.2.: Scanning the addressing position on the FVGA by changing the deflection freqcuency Δ_A of the cAOD. The maximum intensity on the camera at the end of the fibers is recorded. The peak is not fitted or integrated since the imaging system experiences strong aberrations. From the peak position the addressing deflection frequency Δ_{Fn} for all fibers is found. The fiber spacing in terms of the cAOD drive frequency is $\Delta_F = 4.586\,\text{MHz}$.

a series of images with exposers from 1 - 100 000 ms no signal of the neighboring channels is visible. In images taken with high gain and exposure times some crosstalk between the channels is observed. The crosstalk has to be several order of magnitude lower than the actual signal.

I also can demonstrate multi tone operation. By sending eight frequency corresponding to the fiber positions I can couple some light into all fibers (figure 6.3b). The power is in the 10 nW order. This further strong reduction to the previous single addressing comes mainly from the $1/N^2$ scaling in the power for the generated diffraction orders. Additionally the RF drive power is reduced by $1/N^2$ due to previously discussed reasons(chapter 4.4.3).

This also translates to the two tone operation which is of practical use. Any combination of fibers can be addressed. The coupling can be aligned such that the power is well balanced as can be seen from the single tone measurement in figure 6.3a.

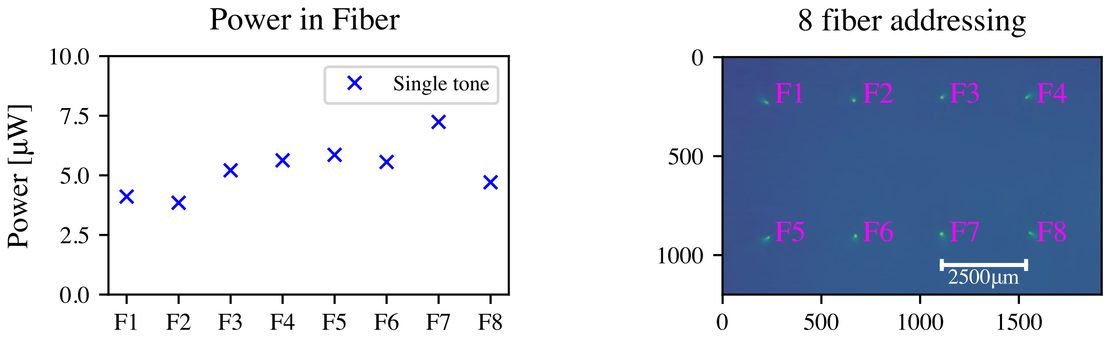

(a) power for single tone addressing

(b) multi tone addressing

Figure 6.3.: The FVGA was aligned such that fiber 1 and 8 have a similar coupling efficiency. Figure (a) shows the power measured with the power meter in each fiber when sweeping the frequency. The power before the FVGA was 2.55 mW so the coupling is in the 1.5 % range. Figure (b) shows one image where 8 tones are generated. The power for each peak is in the nW range. But the optical power before the FVGA is reduced due to the imperfect RF generation. The colormap is logarithmic to make the small fiber cores visible.

7. Conclusion

The individual addressing system using a crossed acousto optic deflector was first simulated and then designed around the available lenses and mechanical mounts. The key requirement of a waist size far below the ion spacing of 5 µm is achieved with a beam diameter($1/e^2$) of 2.24 µm. The archived addressing range of 302.9 µm is sufficient to address more than 50 ions.

The operation of the cAOD was tested in different modes. The steering in horizontal and vertical direction allows to align the system and allows for small adjustments in software. The addressing of multiple ions was simulated by driving the device with multiple RF tones simultaneously.

The generation of an adequate RF drive signal can be improved significantly. The power arriving in the desired frequency peaks needs to be balanced. And the diffraction efficiency needs to be accounted for in order to have constant power across the whole range.

The crosstalk measured with the camera is 3×10^{-3} which is slightly higher compared to similar setups. This can simply come from limitations in the measurement and from different setups and data analysis. An effect to consider is the lower magnification used to make a bigger addressing range accessible.

A key improvement for the RT-setup is the newly built splitting board which enables better power distribution of the 729 nm qubit manipulation light. The smart use of the switching AOMs drive frequency allows to use the cAOD without special optimizations and no resulting power losses. The AOMs used for the switching experienced some temperature drifts depending on pulsed or continuous operation. This effect was resolved by keeping them "warm" during idle times by driving them far off the desired operation point. The designed addressing system was mounted to the chamber with the designed custom mounts which allow the system to be pre-aligned in a test setup. The mount offers some flexibility for future changes to the setup. In addition it also integrates the flip mirror to switch between cAOD and WGA.

The alignment on the setup proved to be challenging. Due to time constraints the setup is not fully optimized. The current state of the alignment produces an addressing beam with a diameter($1/e^2$) of 3.57 µm. This is $\sim$ 1.6 times bigger compared to the achieved beam diameter in the test setup. This spot size is small enough to address ions in a chain with spacing of 5 µm.

Aberrations introduce a relative strong crosstalk to the neighboring ion of 2×10^{-2}. The side not affect by the aberrations has much lower crosstalk and indicates the system can perform as intended.

Next steps involve the further optimization of the alignment of the objective, addressing system and imaging system. The experienced aberrations might be studied with more simulations to optimize the system. The beam size and crosstalk should also be measured by moving the ion instead of the addressing system.

Another avenue was using a FVGA as a mode filter after a cAOD. In a test setup the feasibility of this separate setup was studied. A working prototype allowed to test the lens system and demonstrated the in-coupling to the fibers. Based on the test changing the in-coupling lens for a shorter focal length of $f = 30\,\mathrm{mm}$ should improve the coupling efficiency. This lens gives a better match between the fiber core and spot size. The setup is essentially a simultaneous coupling of eight fibers which needs high precision mounts and a very stable setup. Both aspects can be improved by replacing the used xyz-stage with a resolution of $10\,\mu\mathrm{m}$ with higher resolution stage. In addition two rotation degrees of freedom in the FVGA-mount are needed. For this a custom mounting solution with the center of rotation at the fiber tips has to be implemented.

Appendix A

Data sheets

A.1. Crossed AOD

Test Sheet

DTSXY-400-730

Serial Number 1001 - O230052	A-A Reference File: O230052

The AO component is combined with the RF driver : -

Device characteristics

Central Drive Frequency (Fc)	110MHz (Tol:+/-2MHz) @730nm	**Customer Wavelength (Lambda)**	730nm
AO Bandwidth (DF)	38MHz	**Material (velocity=v)**	TeO2 (650m/s)
Active Aperture	7,5mm	**0th order angular Direction**	+7° (+: clockwise/incident beam)
Laser Polarisation IN (*)	Linear perpendicular	**1th order angular Direction**	~colinear @Fc (ref incident beam)
Max Power Density (**)	$5W/mm^2$	**Scan Angle**	(42mrad)*
AO Laser Frequency Shift	on X: +Fc +/-DF/2	**Electrical Impedance**	50 Ohms
AO Laser Frequency Shift	on Y: +Fc +/-DF/2	**Cooling**	Conduction through base plate
Max Accepted RF Power (***)	2W		
Laser Beam Diameter	500µm<Diam<6mm		

Measured performances

Laser Wavelength = **780 nm**

Beam Diameter ($1/e^2$) = **1,6 mm**

	Specification	*Measurement*
Optical Transmission /axis : T(%)	> 95%	**99 %**
VSWR @ DF	-	**<2,2 /1**
RF Power / axis : Prf (W)	< 2W	**1,2W**
Efficiency in "1-1" order (****)	>40%	**>58 %**

Observation

Drive frequency (F) vs optical wavelength (Lambda) :
With AO birefringent interaction, there is a one-to-one correspondance between the optical wavelength and the drive frequency (linked to the crystal birefringence), typically
(F1/F2) ~ (Lambda2)/(Lambda1)
So the AO response measured @785nm is lower than the response specified @730nm
=> The ao measurement are @785nm in good accordance with the performances to be reached @730nm

Drive RF power (P) vs optical wavelength (Lambda) : $(P1/P2) \sim (Lambda1/Lambda2)^2$

Please refer to the section birefringent "high frequency" interaction of your operating manual

 # OPERATING MANUAL : Please download the operating manual "DTSXY High Frequency +Freq" on our restricted access area at "www.aaoptoelectronic.com".

 # BE CAREFULL : To avoid any damage, never use a frequency out of the bandwidth specified in the test sheet !

Comments

(*): Polarisation defined / XY base plate, INPUT = Y axis
(**): To avoid any damage on coated faces or in the bulk crystal. Do not focuse the beam directly on the AO cell
(***): To avoid any damage on the transducer
(****): See measurement curves (Efficiency vs Drive Frequency)

Date: 07/07/2023 ***Operator:*** Y.CIMBE

A.A S.A., 18 rue Nicolas Appert - F 91898 ORSAY Phone: +33 (8) 11 09 76 76 - Fax: +33 (1) 76 91 50 31 web site: www.a-a.fr

Figure A1.: Data sheet for the crossed acousto optic deflector.

A.2. Photon Gear objective

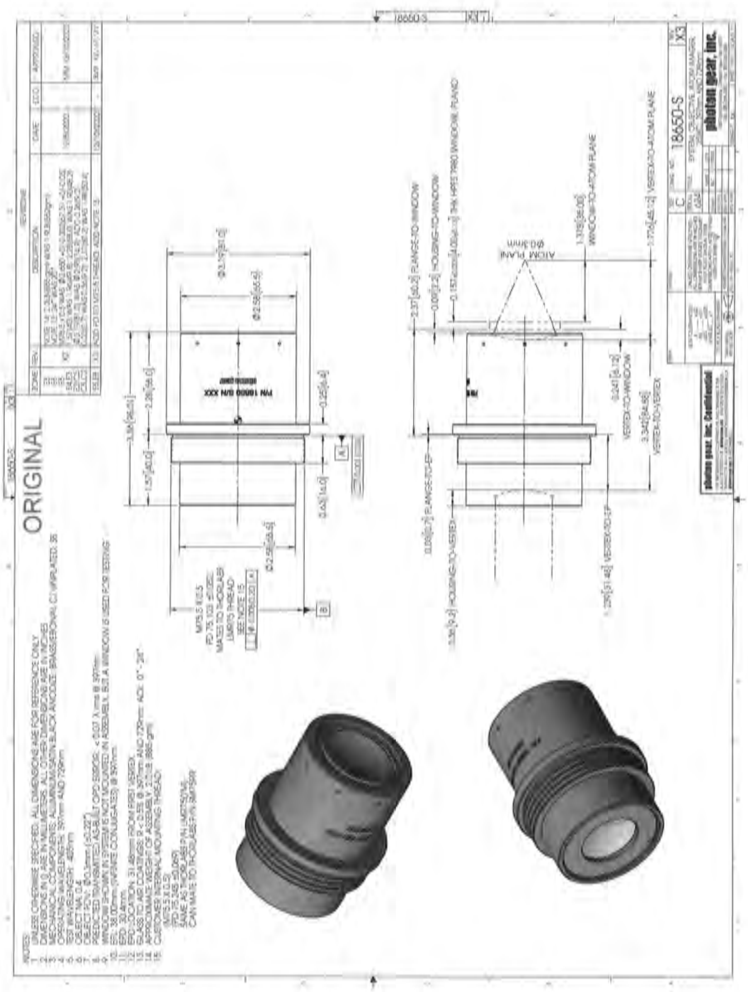

Figure A2.: Data sheet for the imaging and addressing objective.

Appendix B

Additional Measurements

B.1. Telescope with 200 mm lens

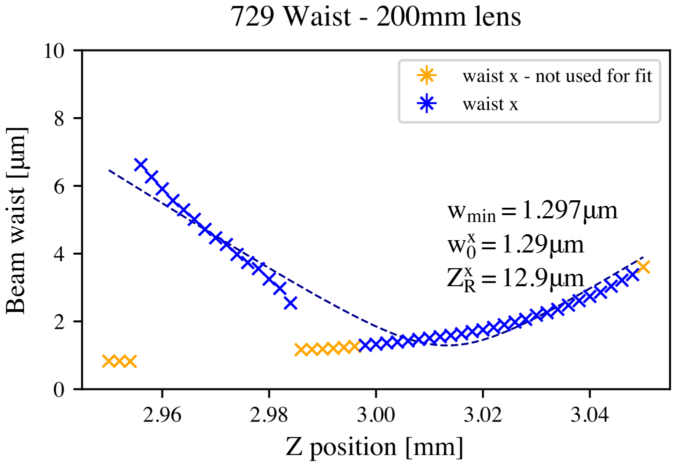

(a) Waist

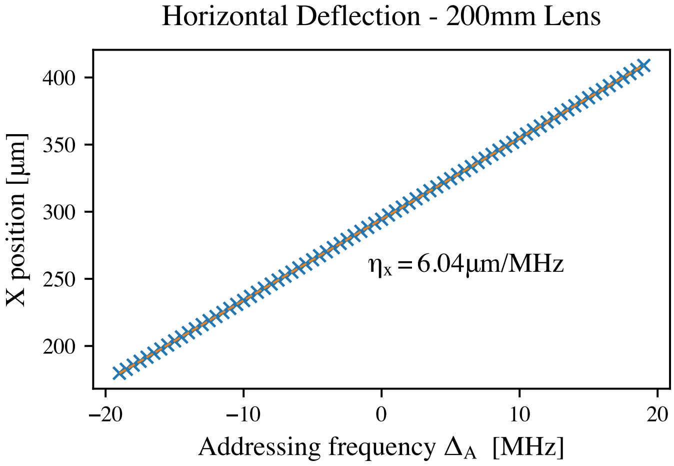

(b) Horizontal addressing range

Figure B1.: Waist measurement and addressing range measurement for the lens system $[60, 125, -40, 200^*]$ (compare chapter 4.3 and 4.4). The achievable range is 229.3 μm.

B.2. Flip mirror stability

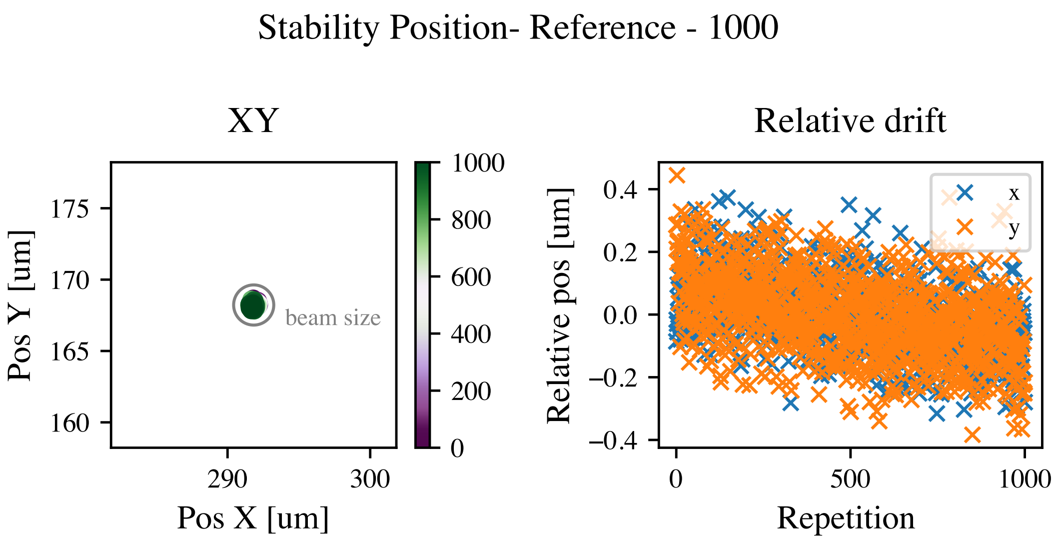

(a) Position stability

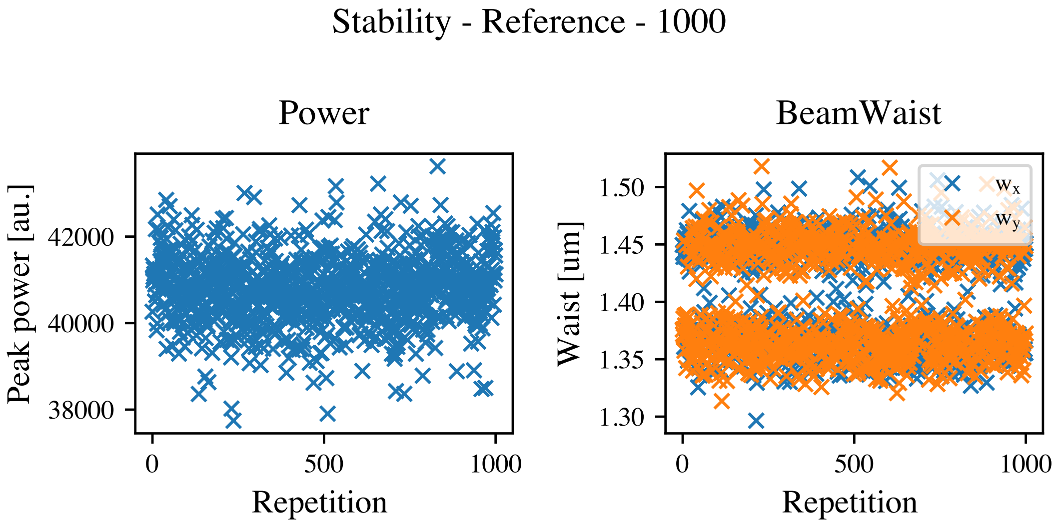

(b) Spot stability

Figure B2.: Reference measurement of the system stability (setup described in chapter 4.1.2). Nothing was moved during the course of the . Between each image a wait time of 2 s was added. Total measurement time approximately 30 min.

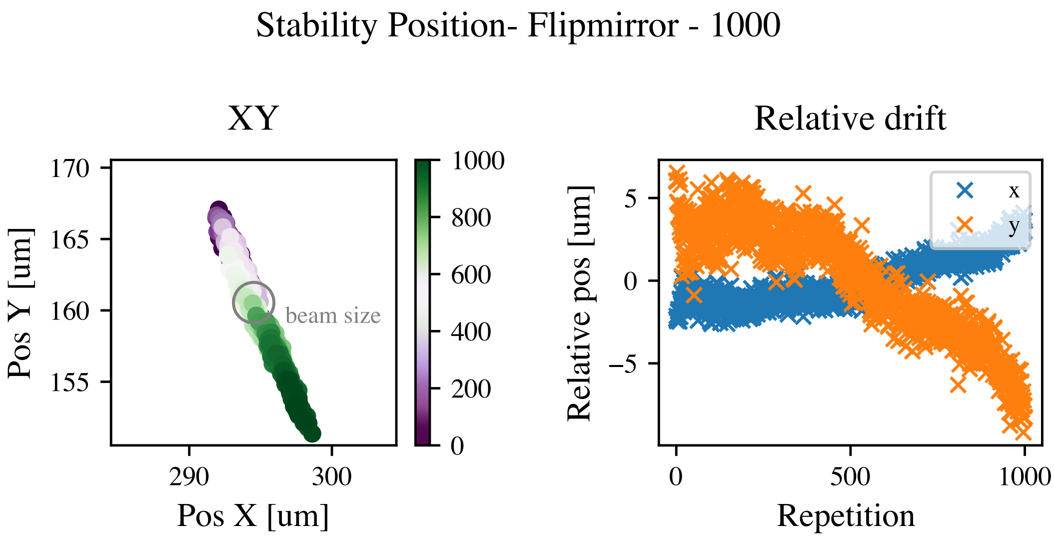

(a) Position stability

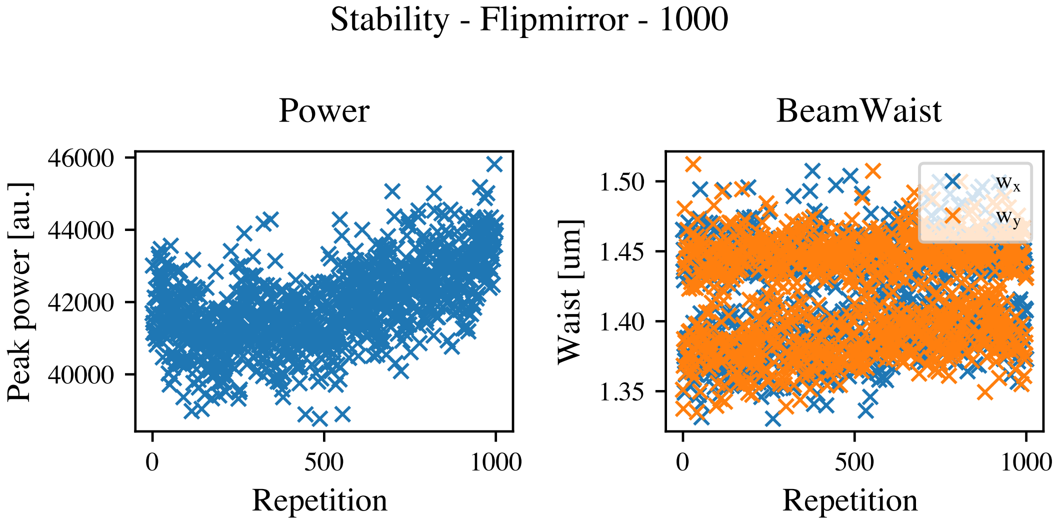

(b) Spot stability

Figure B3.: The stability of the Flip Mirror for 1000 flip cycles (up-down-up). Between each flip a wait time of 1 s was added. Total measurement time was approximately 30 min. The measurement was performed directly after the reference measurement (figure B2).

B.3. Addressing mount stability

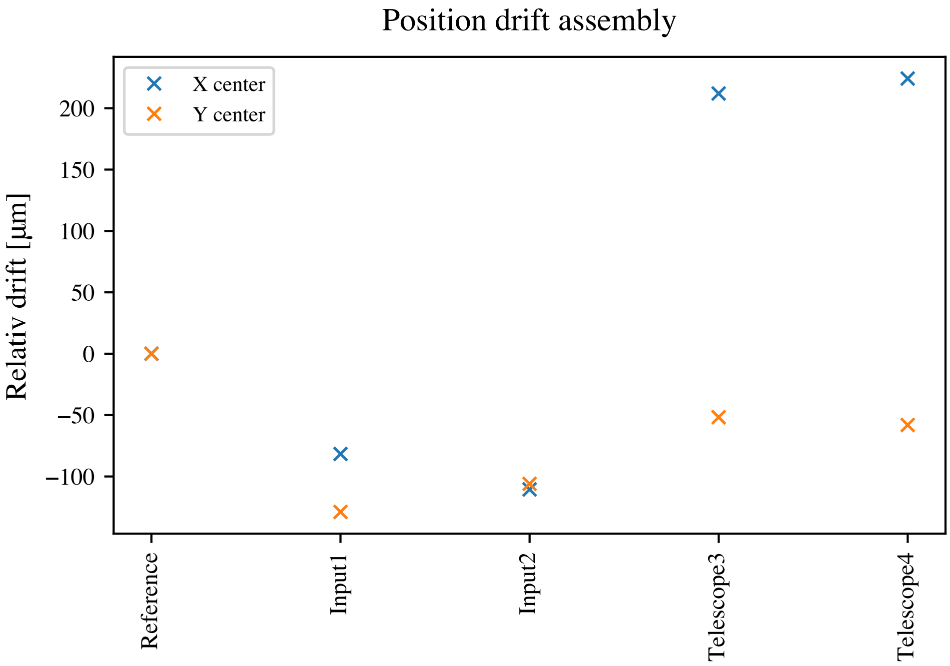

Figure B4.: An estimate of the reproducibility of the mechanical assembly presented in chapter 5.1.2. The cage system was aligned without any lenses. At the end a camera was placed. The gaussian beam is fitted to extract the beam position. The measurements were taken from left to right. First a reference measurement was taken. Then the input plate was removed twice and remounted. Then the same procedure for the Telescope plate was repeated. Since the two dots of the consecutive removal and mounting are closer this is an indication that the screw tension and assembly routine can further improve the stability. We can estimate the repeatability to be approximately 0.3 mm in the horizontal direction and 0.2 mm in the vertical direction.

B.4. AWG with Moku:Pro

(a) No bandpass (b) width bandpass

Figure B5.: Testing the RF generated from the Moku AWG. The signal is measured with an Keysight FieldFox spectrum analyzer. In (a) and (b) the same signal is generated at a frequency of 110 MHz. The bandpass filter suppresses the higher harmonics at the cost of −1.5 dB attenuation.

(a) No bandpass (b) width bandpass

Figure B6.: Driving five addressing frequencies: −19, −5, 0, 5 and 19 MHz. The effect of the bandpass is more pronounced and also lowers the background significantly. We observe an attenuation of ∼−13 dB. This is in good agreement with an power reduction of $1/N^2$ where N is the number of generated frequencies.

(a) bandpass, 4 repetitions (b) bandpass, 2 repetitions

Figure B7.: Driving seven addressing frequencies: −19, −10, −5, 0, 5, 10 and 19 MHz. Only the number of repetitions of the time domain signal sent to the Moku was changed. We see the peaks in (a) are more pronounced. In (b) some side peaks are visible which lead to shadow dots in the addressing.

B.5. Telescope collimation

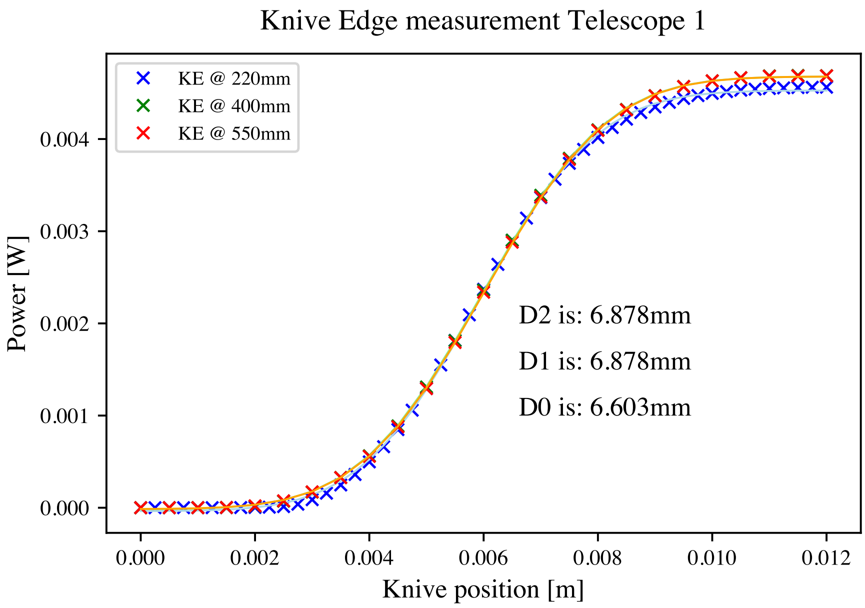

(a) Telescope 1

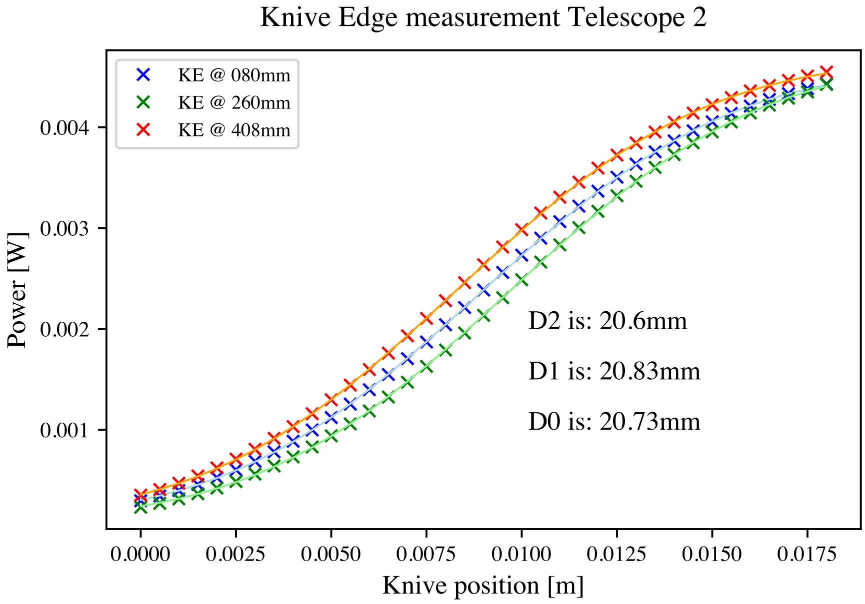

(b) Telescope 1 and 2

Figure B8.: Knive edge measurements of the 729 nm beam after the addressing telescope. These measurements were performed during the alignment of the telescopes. Each trace is the beam diameter at a different position after the last telescope lens. The Zemax simulation predicts beam diameters of 6.4 mm for the first telescope and 20.4 mm for the total telescope. We can see that the beam is collimated, and thus the shear plate interferometer is feasible to collimate beams.

Glossary

AC alternate current
AOD acousto optic deflector
AOM acousto optic modulator
API application programming interface
AWG arbitrary waveform generator

CAD computer aided design
cAOD crossed acousto optic deflector

DC direct current
DMD digital micro-mirror device
DP AOM double pass acousto optic modulator

EOM electro optic modulator

FVGA fiber v-groove array

HDR high dynamic range

iFFT invers Fast Fourier transform

NA numerical aperture
ND neutral density

PBS polarizing beam splitter
PMT photo multiplier tube

RF radio frequency
RT room temperature

UHV ultra high vacuum
UV ultra violet

WGA wave guide array

Bibliography

[1] J. I. Cirac and P. Zoller. Quantum Computations with Cold Trapped Ions. *Physical Review Letters*, 74(20):4091–4094, May 1995.

[2] Colin D. Bruzewicz, John Chiaverini, Robert McConnell, and Jeremy M. Sage. Trapped-Ion Quantum Computing: Progress and Challenges. *Applied Physics Reviews*, 6(2):021314, June 2019. arXiv:1904.04178 [physics, physics:quant-ph].

[3] John Clarke and Frank K. Wilhelm. Superconducting quantum bits. *Nature*, 453(7198):1031–1042, June 2008. Publisher: Nature Publishing Group.

[4] Google AI Quantum and Collaborators et al. Hartree-Fock on a superconducting qubit quantum computer. *Science*, 369:1084–1089, September 2020.

[5] M. Steffen, D. P. DiVincenzo, J. M. Chow, T. N. Theis, and M. B. Ketchen. Quantum computing: An IBM perspective. *IBM Journal of Research and Development*, 55(5):13:1–13:11, September 2011.

[6] Alexander M. Dalzell, Aram W. Harrow, Dax Enshan Koh, and Rolando L. La Placa. How many qubits are needed for quantum computational supremacy? *Quantum*, 4:264, May 2020.

[7] P.W. Shor. Algorithms for quantum computation: discrete logarithms and factoring. In *Proceedings 35th Annual Symposium on Foundations of Computer Science*, pages 124–134, Santa Fe, NM, USA, 1994. IEEE Comput. Soc. Press.

[8] Somayeh Bakhtiari Ramezani, Alexander Sommers, Harish Kumar Manchukonda, Shahram Rahimi, and Amin Amirlatifi. Machine Learning Algorithms in Quantum Computing: A Survey. In *2020 International Joint Conference on Neural Networks (IJCNN)*, pages 1–8, Glasgow, United Kingdom, July 2020. IEEE.

[9] Dylan Herman, Cody Googin, Xiaoyuan Liu, Alexey Galda, Ilya Safro, Yue Sun, Marco Pistoia, and Yuri Alexeev. A Survey of Quantum Computing for Finance, June 2022. arXiv:2201.02773 [quant-ph, q-fin].

[10] Youngseok Kim, Andrew Eddins, Sajant Anand, Ken Xuan Wei, Ewout van den Berg, Sami Rosenblatt, Hasan Nayfeh, Yantao Wu, Michael Zaletel, Kristan Temme, and Abhinav Kandala. Evidence for the utility of quantum computing before fault tolerance. *Nature*, 618(7965):500–505, June 2023. Publisher: Nature Publishing Group.

[11] P. A. Barton, C. J. S. Donald, D. M. Lucas, D. A. Stevens, A. M. Steane, and D. N. Stacey. Measurement of the lifetime of the 3 d 2 D 5 / 2 state in 40 Ca +. *Physical Review A*, 62(3):032503, August 2000.

[12] Jian Jin and D. A. Church. Precision lifetimes for the Ca + 4 p 2 P levels: Experiment challenges theory at the 1% level. *Physical Review Letters*, 70(21):3213–3216, May 1993.

[13] Cornelius Hempel. *Digital quantum simulation, Schrödinger cat state spectroscopy and setting up a linear ion trap.* PhD thesis, August 2014.

[14] Markus Teller. Single-ion addressing for the high-fidelity implementation of quantum network protocols. April 2017.

[15] H. C. Nägerl, D. Leibfried, H. Rohde, G. Thalhammer, J. Eschner, F. Schmidt-Kaler, and R. Blatt. Laser addressing of individual ions in a linear ion trap. *Physical Review A*, 60(1):145–148, July 1999.

[16] Lukas Pernthaler. Single Ion Addressing of up to 50 Ions. Master's thesis, Leopold-Franzens University of Innsbruck, August 2019.

[17] I. Pogorelov, T. Feldker, Ch. D. Marciniak, L. Postler, G. Jacob, O. Krieglsteiner, V. Podlesnic, M. Meth, V. Negnevitsky, M. Stadler, B. Höfer, C. Wächter, K. Lakhmanskiy, R. Blatt, P. Schindler, and T. Monz. Compact Ion-Trap Quantum Computing Demonstrator. *PRX Quantum*, 2(2):020343, June 2021.

[18] Hendrik Timme. Single-ion addressing using crossed acousto-optic deflectors. Master's thesis, ETH Zürich, March 2023.

[19] Philip Zupancic, Philipp M. Preiss, Ruichao Ma, Alexander Lukin, M. Eric Tai, Matthew Rispoli, Rajibul Islam, and Markus Greiner. Ultra-precise holographic beam shaping for microscopic quantum control. *Optics Express*, 24(13):13881, June 2016.

[20] Flavia Timpu, Roland Matt, Simone Piacentini, Giacomo Corrielli, Matteo Marinelli, Cornelius Hempel, Roberto Osellame, and Jonathan Home. Laser-Written Waveguide Array Optimized for Individual Control of Trapped Ion Qubits in a Chain. 2022.

[21] A. S. Sotirova, B. Sun, J. D. Leppard, A. Wang, M. Wang, A. Vazquez-Brennan, D. P. Nadlinger, S. Moser, A. Jesacher, C. He, F. Pokorny, M. J. Booth, and C. J. Ballance. Low Cross-Talk Optical Addressing of Trapped-Ion Qubits Using a Novel Integrated Photonic Chip, October 2023. arXiv:2310.13419 [physics, physics:quant-ph].

[22] David P. DiVincenzo and IBM. The Physical Implementation of Quantum Computation. *Fortschritte der Physik*, 48(9-11):771–783, September 2000. arXiv:quant-ph/0002077.

[23] Anders Sørensen and Klaus Mølmer. Entanglement and quantum computation with ions in thermal motion. *Physical Review A*, 62(2):022311, July 2000.

[24] Vincent Pierre Yves Jarlaud. *Sideband Cooling of Ion Coulomb Crystals in a Penning Trap.* Ph.D., Imperial College of Science, May 2018.

[25] Stephan Gulde. *gulde_diss.pdf.* PhD thesis, Leoplad-Franzens-Universität Innsbruck, 2003.

[26] H Haffner, C Roos, and R Blatt. Quantum computing with trapped ions. *Physics Reports*, 469(4):155–203, December 2008.

[27] E. A. Saleh and Balvin Carl Teich. *Fundamentals of Photonics*. John Wiley & Sons, Ltd, 1 edition, 1991. _eprint: https://onlinelibrary.wiley.com/doi/pdf/10.1002/0471213748.

[28] AA Optoelectronic. AA Application Notes.

[29] Ralf Alexander Berner. *GKP-Setup Imaging System and Single Ion Adressing with an AOD*. Semester thesis, ETH Zürich, July 2022.

[30] E. A. Donley, T. P. Heavner, F. Levi, M. O. Tataw, and S. R. Jefferts. Double-pass acousto-optic modulator system. *Review of Scientific Instruments*, 76(6):063112, June 2005.